Development of Highly Compact Hydrostatic Motor for Low Speed High Torque Applications

Sørensen, Rasmus Mørk

Publication date:
2013

Document Version
Early version, also known as pre-print

Department of Mechanical and Manufacturing Engineering.
Aalborg University, Denmark.
Special Report No. 100

Development of Highly Compact Hydrostatic Motor for Low Speed High Torque Applications

Ph.D. Thesis

by

Rasmus Mørk Sørensen

Department of Mechanical and Manufacturing Engineering, Aalborg University
Fibigerstræde 16, DK-9220 Aalborg East, Denmark
e-mail: rms@liftra.dk

Typeset in LaTeX and printed in Aalborg, September 2013.

ISBN 87-91200-66-0

Title:	Development of Highly Compact Hydrostatic Motor for Low Speed High Torque Applications
PhD student:	Rasmus Mørk Sørensen
Supervisors:	Professor Michael R. Hansen, PhD Assoc. Prof. Ole Ø. Mouritsen, M.Sc. Assoc. Prof. Morten K. Ebbesen, PhD Director Per Fenger, M.Sc.

Publications in refereed journals:

- Sørensen, R. M., Hansen, M. R. and Mouritsen, O. Ø. Numerical and Experimental Study of Hydrostatic Displacement Machine. *International Journal of Fluid Power* 13 (2012) No. 2 pp 29-40
- Sørensen, R. M., Hansen, M. R. and Mouritsen, O. Ø. Numerical and Experimental Study of Friction Loss in Hydrostatic Motor. *Modeling, Identification and Control*, Vol 33, No. 3, 2012, pp. 99-109, ISSN 1890-1328

Publications in proceedings:

- Sørensen, R. M., Hansen, M. R., Mouritsen, O. Ø. and Fenger, P. E. Investigation of Hydraulic Motor Principle for Low Speed High Torque Applications. *Proc. of the 22th. Nordic Seminar on Computational Mechanics*, 2009, Aalborg, Denmark.
- Sørensen, R. M., Hansen, M. R., Mouritsen, O. Ø. and Fenger, P. E. Hydraulic Yaw System for Wind Turbines with New Compact Hydraulic Motor Principle. *Proc. of the European Wind Energy Association Conference*, 2011, Brussels, Belgium.

This thesis has been submitted for assessment in partial fulfillment of the PhD degree. The thesis is based on the submitted or published scientific papers which are listed above. Parts of the papers are used directly or indirectly in the extended summary of the thesis. As part of the assessment, co-author statements have been made available to the assessment committee and are also available at the Faculty. The thesis is not in its present form acceptable for open publication but only in limited and closed circulation as copyright may not be ensured.

Preface

This thesis has been submitted to the Faculty of Engineering, Science and Medicine at Aalborg University in partial fulfillment of the requirements for the Ph.D. degree in Mechanical Engineering. The underlying work has been carried out at the Department of Mechanical and Manufacturing Engineering, Aalborg University and Liftra Aps during the period from January 2009 to September 2013.

The work has been partially founded by the Danish Ministry of Science, Technology and Innovation, under the Industrial PhD initiative as project no. 08-041618.

A number of other persons have earned my biggest thanks for their competent support during the project: my supervisors Michael R. Hansen (UIA), Ole Ø. Mouritsen (AAU) and Morten K. Ebbesen (UIA), my company supervisor Per Fenger (Liftra), the technical staff at AAU Søren Bruun, Bjarne Kristensen and Jan Christiansen. Last, but not least, I thank my girlfriend, Majken, for being the strongest woman I know.

Rasmus Mørk Sørensen
Aalborg, September 2013.

Abstract

This industrial PhD project concerns the development of a new type of hydrostatic motor with high specific displacement (displacement pr. volume). The development work has been based on a model based approach combined with experimental work on prototypes. The new type of motor has some advantages regarding specific displacement, however, it also has some potential disadvantages associated with the structural flexibility that influences the leakage paths and, subsequently, the performance of the motor. Classically, the structural flexibility of hydraulic components is kept at a minimum by simply adding more material and specifying tight manufacturing tolerances. This is a reliable approach but it yields heavy motors with relatively low specific displacement. To minimize the volume of the motor principle put forward in this report, the structural deflections that influence the leakage paths of the motor are instead opposed by counteracting hydrostatic forces, referred to as compensation pressures. The structural deflections, the adjustment of the structural deflections and the consequences for the motor efficiencies are investigated in depth in this report.

The volumetric and the hydromechanical efficiencies are examined by a fluid structure interaction (FSI) simulation. The volumetric losses are investigated by solving Reynolds equation for the pressure distribution in the gaps of concern. The corresponding gap heights are evaluated iteratively by linear finite element (FEM) simulations. The modeling of the friction losses is identified as a Stribeck curve which depends on gap height. The asperity friction is decreasing exponentially with an increase in gap height. The parameters of the friction loss model are based on prototype measurements that include the structural deflections of the lubricating gap faces.

The simulations are verified by prototype measurements. The prototype used has a displacement of $D = 1.75 l/rev$ and is equipped with pressure, flow, velocity, temperature and torque sensors. Furthermore, the structural deflections of the gap faces are measured with a moving coil actuator. The pressures serve as boundary conditions for the FSI simulation, while the output of the simulations is compared with both the measured internal leakage flow, external leakage flow, torque loss and structural deflection. There is a good correlation between the numerical and experimental work.

The main contributions of the project is the proof of concept of the new motor including the active utilization of pressure compensation and the developed models of the tribology related friction losses and the leakage path related volumetric losses. It is shown that the efficiencies of the motor may be kept above a certain minimum over a wide range of operations and, simultaneously, that the efficiencies can be controlled to improve speed-up and load holding operations. E.g. the total efficiency is of minor importance during start-up, but it is important that the motor is able to transfer the sufficient torque. Hence the torque loss of the motor

can be minimized at the cost of more volumetric loss. Finally, the model based approach and the utilization of compensation pressure has led to a design with limited demands to the manufacturing tolerances.

Resume

Dette Erhvervs-PhD projekt omhandler udviklingen af en ny type hydraulik motor med et højt specifikt deplacement (deplacement pr. motor volumen). Udviklingsarbejdet har været baseret på en modelbaseret fremgangsmåde, som er kombineret med eksperimentelt arbejde på prototyper. Den nye type motor har nogle fordele mht. specifik deplacement, men den har også nogle potentielle ulemper vedrørende den strukturelle stivhed der har indflydelse på lækagevejene og deraf motorens ydeevne. Traditionelt set har den strukturelle stivhed af hydraulik komponenter været holdt på et minimum ved at tilføje tilpas materiale og specificere fine fremstillingstolerancer. Dette er en driftsikker tilgangsvinkel, men den medfører også tunge motorer med relativt lavt specifikt deplacement. For at minimere volumen på den motortype dette projekt omhandler, er de strukturelle udbøjninger, der påvirker lækagevejene i motoren, modvirket med modsatrettede hydrostatiske kræfter, kaldet kompensationstryk. De strukturelle udbøjninger, justeringen af de strukturelle udbøjninger og konsekvenserne for motorens virkningsgrader er undersøgt detaljeret i denne rapport.

De volumetriske og hydromekaniske virkningsgrader er analyseret med en fluid-strukturel interaktion (FSI) simulering. De volumetriske tab er undersøgt ved at løse Reynolds ligning for trykfordelingen i spalterne af betydning. Den tilhørende spaltehøjde er bestemt iterativt med lineære finite element (FEM) simuleringer. Modelleringen af friktionstab er identificeret som en Stribeck kurve som afhænger af spaltehøjden. Kontakt friktionen aftager eksponentielt med en forøgelse af spaltehøjden. Parametrene i friktionstab modellen er baseret på prototype målinger, hvilke inkluderer strukturelle udbøjninger af de overflader der udgør smørefilmen.

Simuleringerne er eftervist med prototype målinger. Den benyttede prototype har et deplacement på $D = 1.75l/omdr$ og er udstyret med tryk-, flow-, hastigheds-, temperatur- og moment målere. Derudover er de strukturelle udbøjninger af overfladerne der udgør oliefilmen målt med en moving-coil aktuator. De målte tryk fungerer som en randbetingelse til FSI simuleringen, mens resultaterne fra FSI simuleringen er sammenlignet med både de målte interne lækageflow, eksterne lækageflow, friktionstab og strukturelle udbøjninger. Der er god overensstemmelse mellem de numeriske og de eksperimentelle resultater.

De væsentligste bidrag fra dette projekt er påvisningen af motorkonceptet, hvilket inkluderer den aktive udnyttelse af kompensationstryk og de udviklede modeller af de tribologi relaterede friktionstab og det volumetriske tab relateret til lækagevejene. Det er eftervist at motorens virkningsgrader kan holdes over et vist minimum over et bredt anvendelsesområde, samtidig med at virkningsgraderne kan styres til at forbedre hastigheds- og last holde operationer. Eksempelvis er den totale virkningsgrad mindre vigtig under opstart, hvor det er mere vigtigt at motoren kan yde det nødvendige moment. Her kan friktionstabet i motoren

blive minimeret på bekostning af mere volumetrisk tab. Derudover har den modelbaserede tilgangsvinkel og brugen af kompensationstryk ført til et design med begrænsede krav til fremstillingstolerancer.

Contents

1

Introduction

The thesis concerns the development of a new type of hydrostatic motor. The project is initiated and partly funded by Liftra Aps and has been carried out as an industrial PhD-project. The main motivation for Liftra Aps is the view to utilize the new motor in the yaw system of wind turbines thereby extending the product portfolio of Liftra Aps beside the usual range of special cranes and lifting equipment. Another motivation is the use of the new motor concept in some of the specialized load carrying equipment of Liftra.

1.1 Liftra

Liftra is a small size company within the market for lifting and transportation equipment for the wind turbine industry. Liftra has since 2003 grown with the wind turbine industry and are now employing around 45 persons in Aalborg (Denmark), Hamburg (Germany), Bilbao (Spain), Tianjin (China) and Chicago (USA).

The market potential of Liftra has grown with the increasing size of the wind turbines. The nowadays turbines has reached such a size, that no standard products are available for handling the parts. Liftra is, based on the costumer requirements, developing e.g. stacking frames for transport of blades and tower sections, blade yokes for blade installation/uninstallation, main shaft fixtures for avoiding dismounting of rotor during gearbox replacements and special cranes for gearbox replacements.

Common for many of the Liftra products is that they are tailormade solutions, which themselve are small machines with several hydraulic actuations and advanced controls. The typical design parameters are low price and weight. The weight of the actuation system is sometimes more important than the efficiency of the system.

1.2 Hydraulic Displacement Machines

The performance of hydraulic motors and pumps is related to their efficiencies. The design and manufacturing tolerances are a trade-off between volumetric and hydromechanical losses. The general trend is that if the volumetric loss goes down the hydromechanical loss goes up, and vice versa, because of their opposite nature.

Furthermore, the performance is related to the underlying type of motor or pump; how the fluid pressure is converted to mechanical torque and inversely. The working principles of the motors or pumps are divided into vane and piston types. And again into several subcategories dependent on the manufacturer. The different principles have different advantages, which are all competitive parameters on the market. These are e.g. torque, speed, adjustable displacement, price and actual volume.

1.3 Background and Motivation

The background for this project is a new type of hydraulic motor with some unique application advantages. The idea for the motor principle originated at Liftra and has led to a patent, Fenger (2010). The main advantage of the motor is that it can deliver a high torque in an extraordinary compact form. For several of Liftras special cranes, this torque per outer motor volume ratio is the most important motor parameter. In the wind turbine industry you only lift few times per day, and hence the efficiency is of minor concern. These motors are considered as low energy motors, because most of the time they are only deadweight.

1.4 The Motor Principle

The basis for the project is the new type of hydraulic motor. The principle of the oil displacement of the motor is shown on figure 1.1 and 1.2 in two-dimensional views.

The stops and the rotor form three chambers that are further divided by one or two vanes. However, it can be designed with different number of chambers and vanes as a trade off between specific displacement (displacement per motor volume) and complexity. The rotor is subjected to a torque because of pressure difference across the vanes. The vanes are moved in radial direction when passing a stop.

1.4.1 Motor Characteristics

The motor is characterized as an high torque low speed motor. Hence, minimization of the leakage paths and the structural deflections are envisaged to be crucial in order to reach acceptable volumetric efficiencies. Especially the large faces across the rotor are highly influencing the efficiencies and must therefore have a special attention.

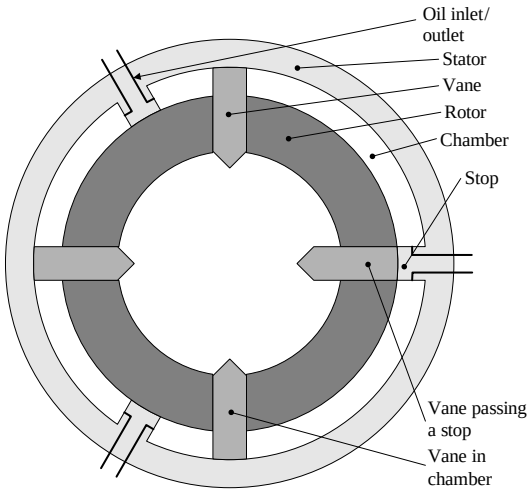

Figure 1.1: The motor principle with name designations.

The motor principle has a very high displacement per volume ratio, (Sørensen et al. (2011)), and it has meanwhile an advantage when up-scaling. Not only the dimensions are enlarged when up-scaling, but also the possibility for more chambers. The main challenge in the motor development is to ensure acceptable efficiencies in the relevant operating conditions.

1.4.2 Potential Applications

The hydraulic motor principle is applicable in several different applications. For e.g. a truck mounted loader crane the efficiency of the crane operations is of minor interest. It is most important that the crane components are compact and light to maximize the space for the load.

Another potential application is as yaw motor in Liftras self hoisting cranes, see figure 1.3. It is special cranes that are developed for a more effective replacement of gearboxes. The crane is, by its own power, hoisted to the nacelle, after which it is able to do a gearbox replacement. Here the weight and occupation of space are more important than the efficiency of the yaw motor. The motor can replace the tooth rim, the pinion gear and the pinion motor, which will decrease the outer dimension of the crane and therefore make the installation of the crane easier.

The original target application for the motor is in the yaw system of a wind turbine, which is described in Sørensen et al. (2011). The most frequently used electrical yaw system can be replaced by a hydraulic system. The very high specific displacement of the motor principle ensures that the hydraulic system does not occupy too much space. A hydraulic yaw system could solve some of the reliability

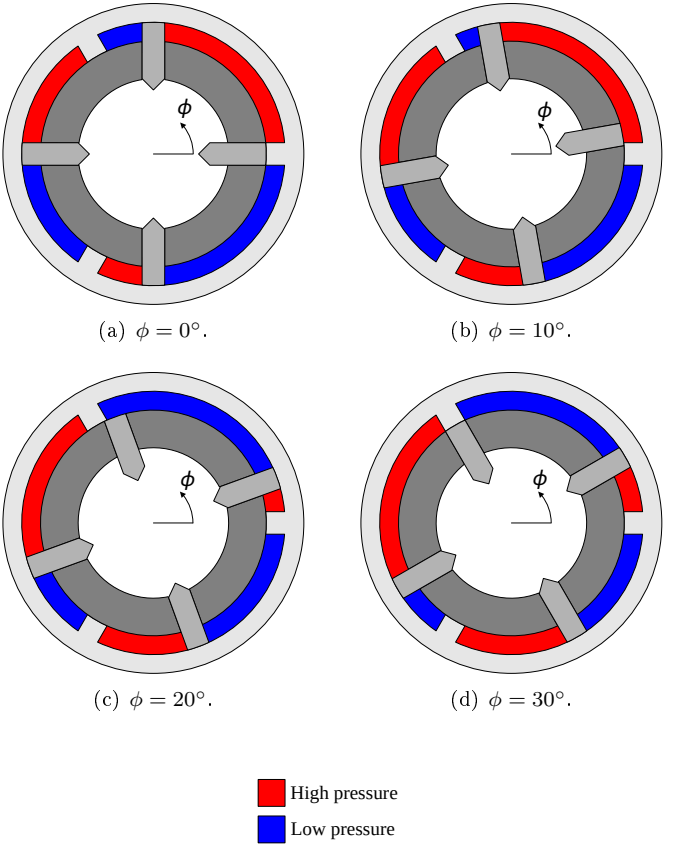

(a) $\phi = 0°$. (b) $\phi = 10°$.

(c) $\phi = 20°$. (d) $\phi = 30°$.

Figure 1.2: A three chamber motor is shown in four positions covering a rotation of $30deg$ of the rotor. No oil inlets/outlets are visualized.

problems that are related to the nowadays electrical yaw systems, Stubkier (2013). The breakdown of gears could be reduced and the external peak loads on the yaw system can be damped by the elasticity of the hydraulic fluid.

1.5 Research Objectives

The research objectives of this project are to extend and increase the use of a model based approach when designing and developing hydraulic displacement machines. The development and manufacturing is both time consuming and expensive due to its strong dependency on tolerances and prototype design. The manufacturing tolerances and surface roughness of the internal parts require special machining facilities and extra manufacturing steps. Also, assembly and testing must be carried out with tight tolerances on parameters such as bolt pretension, choice

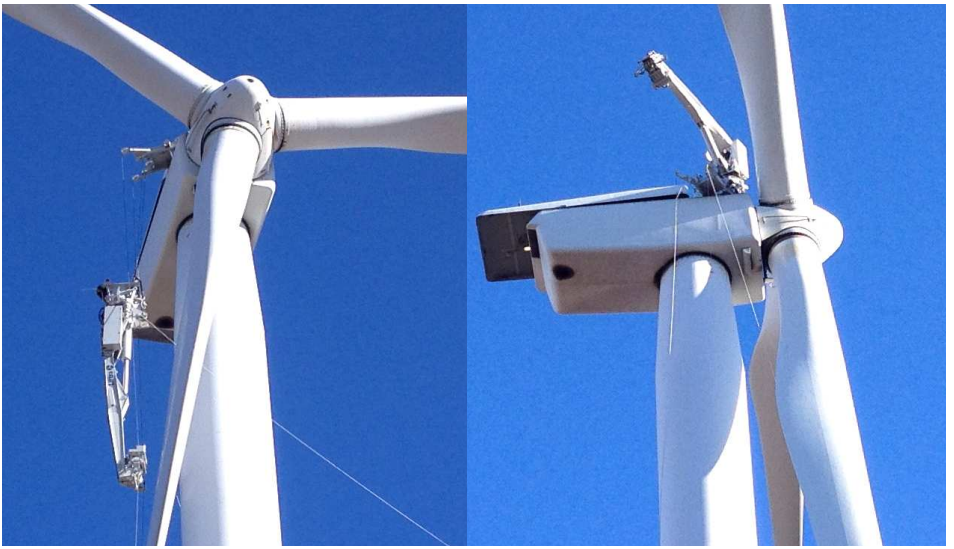

Figure 1.3: A potential motor application is as yaw motor at Liftras self hoisting cranes. Here one is during installation and after the installation on the top of the nacelle of a wind Turbine.

of fluid and fluid temperature. When developing new motors whether it is a new type of motor or simply scaling of an existing this is even more pronounced. For these reasons it is desired to do as much as possible of the experimental work on virtual prototypes.

The use of a model based approach to the design is complicated by the fact that two important design criteria, volumetric efficiency and hydromechanical efficiency, are difficult to evaluate due to their strong relationship to tribological phenomena. Therefore, the modeling typically requires handling of friction, lubrication and complex structural deflections.

The research objectives can be specifically outlined as:

The project shall establish a simulation model to describe the performance of the motor, i.e.

- *Set up an experimental verified model to describe the volumetric losses and how it is influenced by structural deflections.*
- *Set up an experimental verified model to describe the hydromechanical losses and how it is influenced by structural deflections.*
- *Decrease the need for fine production tolerances of the internal parts and*

minimize the negative effects of structural deflections by the utilization of active pressure control via strategically positioned pressure pockets within the motor structure.

1.6 Research Approach

The two large areas across the end faces of the rotor (the face of the rotor shown on figure 1.1 and 1.2) represent the core transmission elements in the motor. They strongly influence the total efficiency of the motor. These areas have, as all the gaps between moving parts, double contradicting functionality, namely sealing and lubrication. If the performance criteria of either of these functionalities are not given proper attention the motor will not be useful for practical applications. The main challenge is to maintain the performance with respect to both sealing and lubrication over a wider range of operating conditions.

1.6.1 Theoretical Loss Modeling

The gaps of concern are investigated by a comprehensive simulation model. The objective of the model is to be able to simulate the actual gap heights and thereby determine the volumetric losses and the hydromechanical losses. The pressure distribution in the gaps is determined by solving the Reynolds equations, where the present gap heights and the actual pressure level of the individual volumes are among the boundary conditions. This pressure distribution in the gaps is again influincing the structural deflections and hence the gap height, which is why pressure and gap height are solved iteratively in a fluid structure interaction simulation.

The gap height is used as the parameter that governs the loss behaviour. The volumetric loss depends on the gap height and the lubrication regime, and the hydromechanical loss is based on gap height.

1.6.2 Experimental Verification

Except for the division into volumetric and hydromechanical losses there exist no unified modeling techniques that describe the losses in hydrostatic machines in detail, Ivantysyn and Ivantysynova (2003).

The volumetric and hydromechanical losses depend highly on surface roughnesses and production tolerances. Especially, the hydromechanical loss is difficult to model in a simple way since it depends on a wide variety of friction. In general, the complex behaviour prevents model based prediction of the performance and therefore design of hydrostatic machines rely heavily on fine machining tolerances and excessive testing of volumetric and hydromechanical losses for the entire operating range, see Ivantysyn and Ivantysynova (2003), Ivantysynova (2003) and Murrenhoff et al. (2008).

For the above reasons an experimental verification is absolut necessary for the development of a theoretical model of a new motor principle. The aim of the experimental work is to develop and validate the simulation models. Therefore the test setup has numerous measurement sensors.

1.7 Outline of Thesis

The thesis is organized in five chapters with the current, the Introduction, being the first, and the last, the fifth, containing the conclusions and discussions.

Chapter 2 introduces the motor principle and all the details of the mechanical design of the prototypes. Furthermore, the experimental part of the project is described with emphasis on the test setup and the measurement procedures and equipment.

Chapter 3 is on the efficiency of hydrostatic motors. This includes a general introduction to state-of-the-art within loss modeling in hydrostatic machines and a presentation of the loss models developed in this project.

Chapter 4 is on the project results and, in general, on the experimental verification of the model principle and the developed simulation models.

The conclusion in chapter 5 reviews the main contributions from the project and give suggestions for future projects.

2

Prototype Experiments

2.1 Introduction

The objective of the prototype testing is to verify the numerical simulations and a proof of concept of the motor principle with compensation pressures. The intention has not been to optimize the total efficiency of the prototype motor.

2.2 Prototype Motor

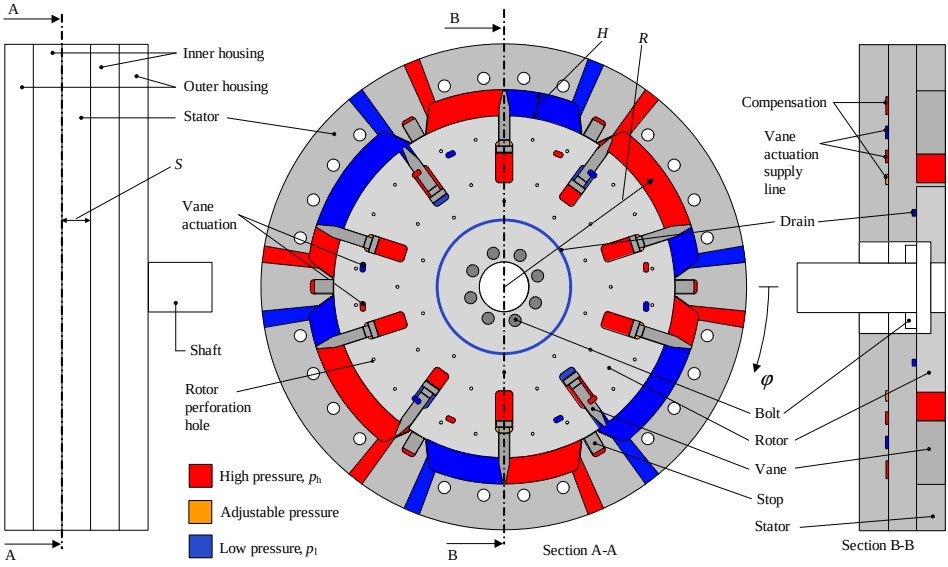

Figure 2.1: The motor principle with hydraulic pressures indicated at the section views.

The prototype motor is shown in figure 2.1. The stops and the rotor form six chambers that are further divided by one or two vanes. The prototype has 10

vanes. The rotor is subjected to a torque because of pressure difference across the vanes. The radial movement of the vanes is facilitated by means of alternating high and low hydraulic pressures in pockets in the housing. In figure 2.1 the pressures corresponding to a clockwise rotation are shown. When not passing a stop the vanes are forced against the stator which seals with the vane tip. To avoid high demands on tolerances on the dominant radial dimension the stops are designed as small pistons that are forced against the rotor by a pressure.

The rotor is perforated with multiple small holes in the axial direction of the motor. The intention is that they equalize the pressure on each side of the rotor thereby preventing any resulting axial force on said rotor.

The displacement, D, of the motor principle is given by

$$D = 2 \cdot \pi \cdot R \cdot S \cdot H \cdot n_{ch}, \tag{2.1}$$

where n_{ch} is number of chambers and R, S and H are geometric dimensions (see figure 2.1). The data and dimensions of the prototype are listed in table 2.1.

Outer motor diameter	$d = 340mm$
Outer motor height	$l = 100mm$
Height of rotor	$S = 20mm$
Width of chamber	$H = 18mm$
Radius to centre of chamber	$R = 129mm$
Number of chambers	$n_{ch} = 6$
Number of vanes	$n_{vane} = 10$
Displacement of prototype	$D = 1.75l/rev$

Table 2.1: Data and dimensions of the prototype.

2.2.1 Hydraulic Vane Actuation

The vanes are formed as pistons that are moving in radial slots of the rotor (see figure 2.1). The radial actuation of the vanes, when passing a stop, is forced by pressures on the vanes. The timing of the actuations is controlled by the vane actuation pressures, p_{v1} and p_{v2}, and their location on the inner housings, see figure 2.2. Each stop is surrounded by a low and a high pressure vane actuation pocket. The pressures are switching with the rotational direction of the motor. The pressure levels are following the low and high pressure of the motor. It is important that the pressure pockets are located sufficiently far from each other to prevent a connection from a high pressure volume to a low pressure one when a vane is just at a middle of a stop.

The hydraulic vane actuation is illustrated by a frame sequence in figure 2.3 which shows the timing and the pressures when a vane is passing a stop. The frames in figure 2.3 are section views with the present surrounding pressures illustrated by red (high pressure) and blue (low pressure) colours. The rotational direction

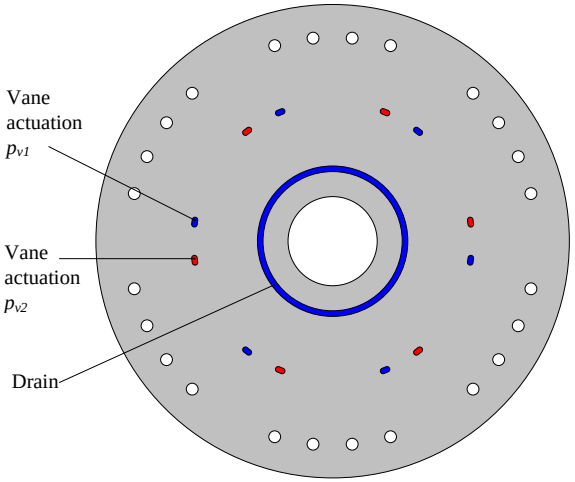

Figure 2.2: The face of the inner housings that is adjacent to the stator and the rotor with their pressure connections marked. The sealing elements are not shown.

is clockwise. The section views of the vanes show that they have internal oil connections and a build-in shuttlevalve. The internal connections ensure that the high pressure of the chamber is lead to the volume above the vane. Then the vanes are forced against the stator and the sealing between vane tip and stator is ensured. The ball of the shuttle valve closes the internal connection to the low pressure volume of the chamber. The opposite connection is closed when the rotational direction is changed.

Explanation of each frame in figure 2.3:

1. There are now two vanes in the right chamber. The vane which is going to pass the stop is approaching the vane actuation high pressure, p_{v2}.

2. The piston side of the vane is now connected to p_{v2}. It is still in its radial position with the vane tip forced against the stator.

3. The vane tip just passes the low pressure connection of the chamber. Therefore the chamber pressure on both sides of the vane drops to the low pressure of the motor. The piston volume of the vane is still connected to p_{v2} which is forcing the vane towards the centre. The volume above the vane is drained through the internal oil connection of the vane.

4. The vane is still forced toward the centre of the rotor. It is now in a position ready to pass the stop without mechanical contact.

5. The vane is just above the stop. The volumes around the vane is isolated, except from leakage flow.

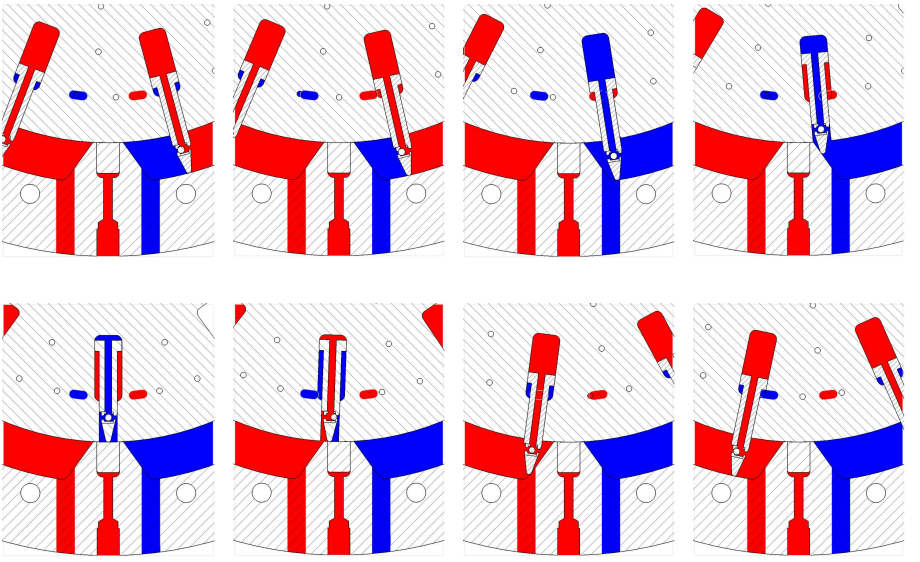

Figure 2.3: A vane is passing a stop.

6. The vane gets connected to the high pressure volume of the next chamber. The ball of the shuttle valve is forced to the side and then the volume above the vane is connected to high pressure. Meanwhile the piston volume of the vane is connected to low pressure through p_{v1}. Thereby the vane is forced outwards against the stop and the stator.

7. The vane is still forced outwards, now against the curvature of the stop.

8. The vane is now fully in the next chamber and ensures that the previous vane can start passing the next stop. The volume of the chamber between the vanes is now isolated, except from leakage flow. The next vane is approaching the stop to pass it in exactly the same way.

One of the vanes of the prototype motor is shown in figure 2.4. The shuttle valve is mounted with a shrink fit. The machining on the top face ensures that the oil is always channeled to both sides of the vane.

2.2.2 Number of Chambers and Vanes

The combination of the number of chambers, n_{ch}, and vanes, n_{vane}, has more implications of the motor performance. The number of vanes, n_{vane}, always needs to be higher than n_{ch} to prevent that the high pressure inlet gets connected to the low pressure outlet at the other side of the chamber. Then the pressure of

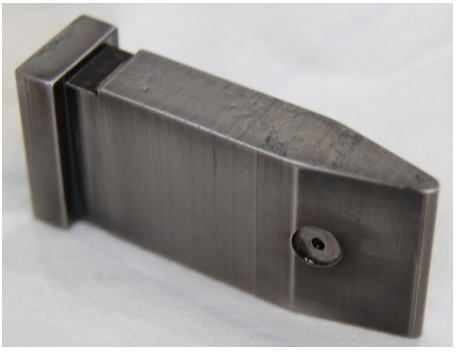

Figure 2.4: A vane of the prototype motor.

the motor will disappear. Therefore it is essential with two vanes in the chamber where a vane is starting to pass a stop.

An even number of n_{vane} and n_{ch} are ensuring that the radial forces on the rotor are balanced. Though, the hydraulic vane actuation is causing flow/speed ripples because of the changed need for flow when a vane is passing a stop. By the balancing of the radial forces there are more vanes that passes a stop at the same time. Therefore the flow/speed ripples become larger.

In general, the combination of n_{ch} and n_{vane} is not straightforward. Besides from the above mentioned influences, there are several geometric limitations too. The design of the prototype is based on that it must have a reasonable displacement, but not being too complex.

2.3 Adjustment of Structural Deflections by Compensation Pressures

The structural deflections of the faces that form the lubricating gap between rotor and inner housing are highly influincing the efficiencies of the motor. These surfaces are referred to as the surfaces of interest (SOI), see figure 2.5. An aim of the project is to investigate the deflections of the SOI and their impact on the efficiencies of the motor. The issue is that the pressure distribution in the gaps between SOI is creating a significant force at the inner housings because of the large area from the outer radius of the chambers to the drain connections located close to the centre of the rotor. These forces are causing a deflection of the inner housings which must be minimized to maximize the volumetric efficiency of the motor. To counteract these deflections, the motor has the compensation pressure volumes between the inner and outer housings (see location and geometry in figure 2.1, 2.5 and 2.6). The colours of the figures are marking the pressurized areas. Red is high pressure, blue is low pressure orange is compensation pressure and green

is representing the pressure in the chamber and in the lubricating gap, which alternates during a revolution.

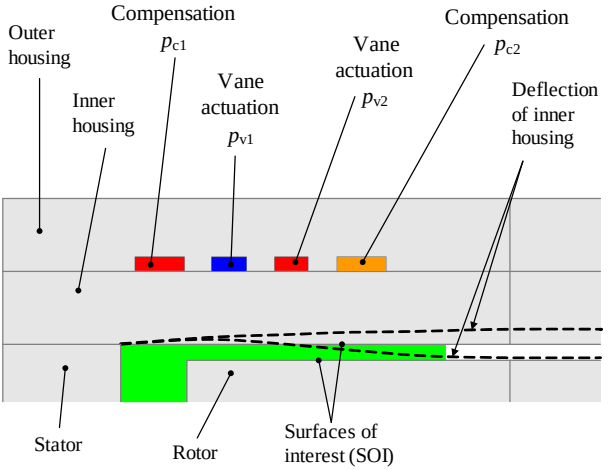

Figure 2.5: A section view of the motor with potential deflections of an inner housing illustrated by the dotted lines. Sørensen et al. (2012*a*)

Besides the pressure distribution in the gap and the compensation pressures, the pressures in the supply lines to the vane actuation also influence the deflections of the inner housings. Therefore the deflection of the inner housings can potentially be in two directions as illustrated by the dotted lines in figure 2.5. The deflection behaviour depends on the area and pressure magnitude of the individual volumes illustrated in figure 2.5. The layout of the vane actuation supply lines and compensation pressure volumes is restricted by the available space outside the sealings and oil channels. The layout of these volumes is illustrated in figure 2.6 without oil inlet channels. The volumes are sealed by o-rings.

The pressures in the vane actuation supply lines follow the low and high pressure levels of the motor. One is connected to the low pressure part and the other to the high pressure part, depending on the rotational direction. The compensation pressure p_{c1} always follows the high pressure of the motor. The inner compensation pressure p_{c2} is made adjustable during the prototype tests. The purpose of the adjustability is to investigate the impact on the deflections of the inner housings. To study when the magnitude of p_{c2} is causing the deflections to follow either of the dotted lines of figure 2.5 or somehow between. Hence, the magnitude of p_{c2} can be examined with regards to both total volumetric and friction loss of the motor.

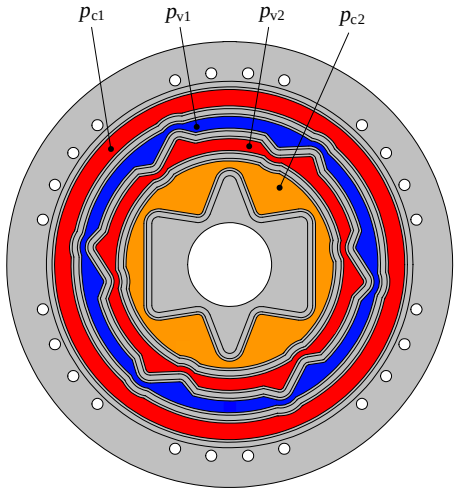

Figure 2.6: The geometry of the compensation and vane actuation supply pressure volumes, which are between the inner and outer housing. Sørensen et al. (2012*a*)

2.4 Experimental Test Setup

The aim of the experimental work is to verify the motor principle and to be able to verify the simulation models. To be able to determine the volumetric and the hydromechanical losses, the test setup has several measurement sensors; pressure transducers to measure p_h, p_l and p_{c2}, a strain gauge transducer to give the output torque, T_{out}, an absolute encoder for motor velocity, flow transducers to give the flow into the motor and out of the motor through the chambers and the drains on both side of the rotor. Further the test setup has a temperature sensor to give the temperature of the oil. The prototype motor is loaded by a powder brake, through a gearbox.

The structural deflections of the inner housing are measured with a moving coil actuator (MCA). The MCA is fitted with a $0.1\mu m$ encoder to measure the position of the MCA piston. The body is mounted on the inner housing of the prototype motor as shown in figure 2.7. The MCA is controlled in force mode and maintains a force of $1.7N$ during the tests so that the piston always is in contact with the rotor. The built-in encoder of the MCA measures the position of the piston and therefore the relative distance between the inner housing and the rotor. The measurements are performed when the rotor rotates and therefore the MCA tip is sliding across the face of the rotor. The extracted gap heights are mean values during one motor revolution to minimize deviations due to e.g. surface roughness and variations in the thickness of the rotor.

The prototype motor is shown in figure 2.8 in the test setup and in figure 2.9 when

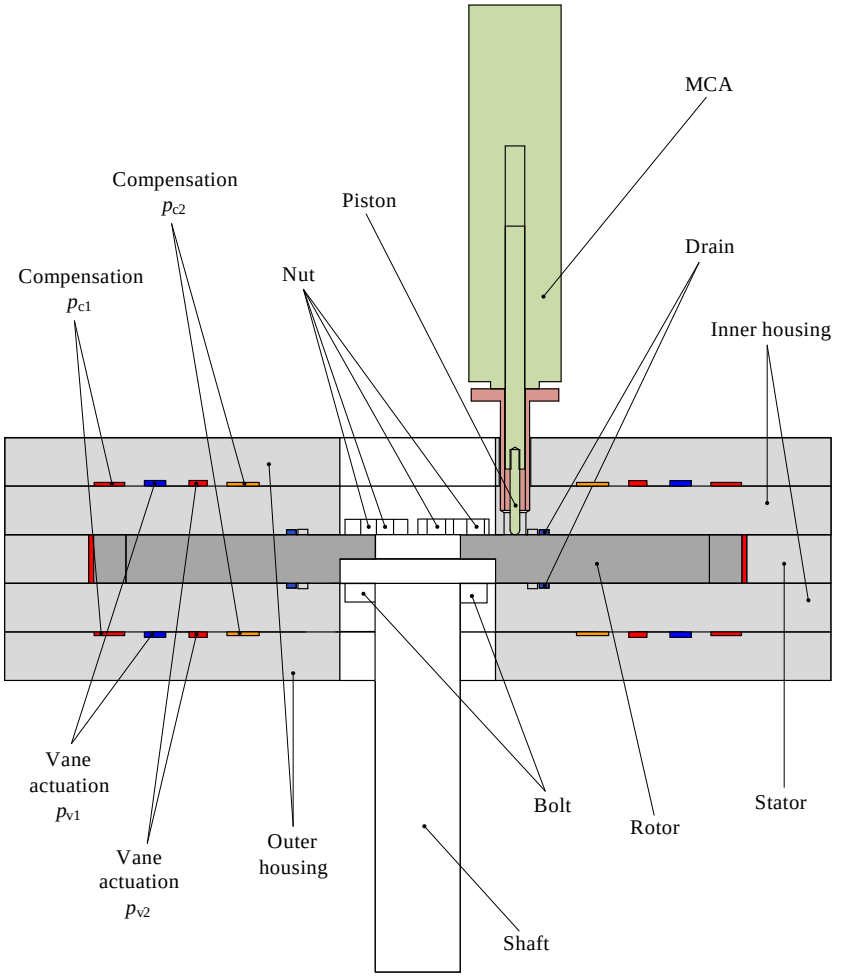

Figure 2.7: Moving Coil Actuator illustration. Sørensen et al. (2012*a*)

partly assembled. The prototype has several oil hose connections, and a lot more than strictly necessary. The intention is to be able to measure more individual flows and pressures during troubleshooting of the motor. During start-up the sealings between the stops and the rotor and between the vane tips and the stator are ensured by mechanical springs.

2.4.1 Meassurement of the Vane Actuations

It was desired to be able to follow the radial actuations of the vanes when passing a stop. A problematic actuation of the vanes will both influence the performance and the efficiencies of the prototype motor. Therefore a kind of data logging of the

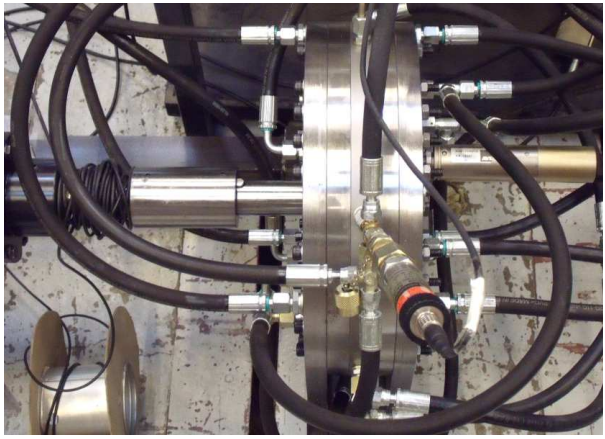

Figure 2.8: The prototype motor in the test setup.

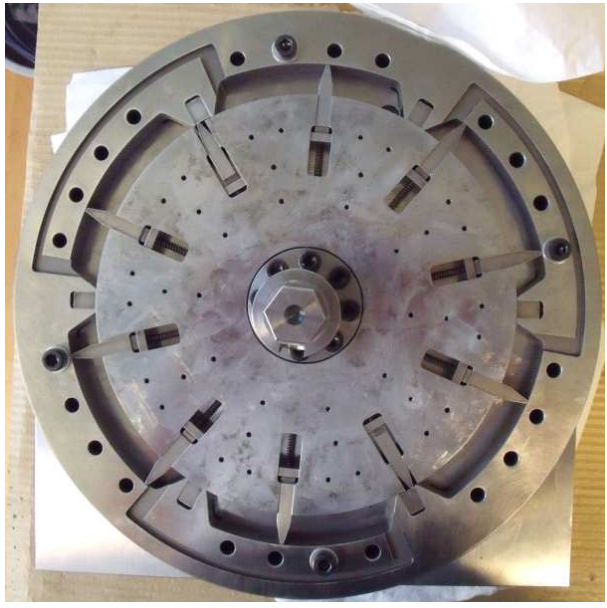

Figure 2.9: The prototype motor when partly assembled.

radial position of the vanes with regard to the angular position of the rotor was desired for troubleshooting and for the identification of the sources to the internal losses.

Furthermore, the vane actuation depends on both the operating high pressure of the motor and the rotational speed. The pressure determines the force by which

the vanes are actuated and the speed determines the time available for the full vane movement before they hit the curvature of the stops. A measurement of the vane positions could also be helpful to examine these motor condition dependencies.

A measurement of the radial position of the vanes in the prototype motor was considered too sophisticated. The time needed and the necessary design changes of the prototype would move the focus from the deflection impacts. Therefore the vane actuation mechanism of the prototype is visually verified through a small porthole in the inner and outer housings, see size and location in figure 2.10. With the portholes (one on each side of the rotor) it is possible to see the movement of the vanes both before and after the passing of a stop, because of the location of them. The portholes at the shown location are not influencing the performance of the motor. The portholes are not included in the previous figures to limit the information level.

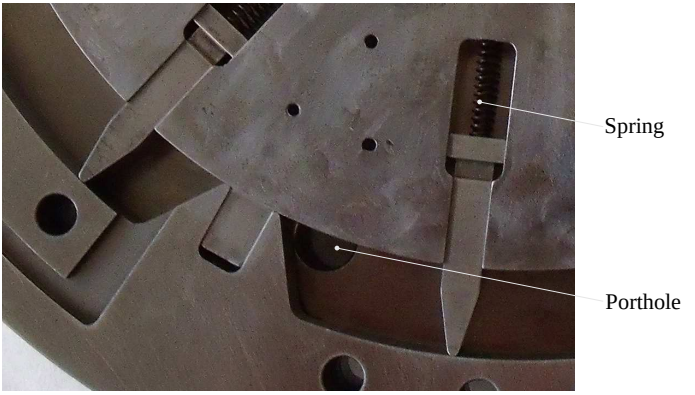

Figure 2.10: A porthole through the inner and outer housing is useful for a visual inspection of the movement of the vanes.

The springs between the rotor and the vanes (see figure 2.10) ensure that the vanes are pushed against the stator during start-up and therefore make the pressure build-up possible.

2.5 Summary of Contributions

This chapter presented the work carried out with regard to the experimental part of the project, including the following:

- A new motor concept has been derived from the motor concept originated at Liftra.
- The motor concept has been realized in a prototype.
- The prototype has been instrumented and tested succesfully.

3

Efficiency of Hydrostatic Motor

Two important parameters for hydrostatic motors are displacement and efficiency. The displacement of hydraulic motors is the basic parameter for the size of the motor and the efficiency is a parameter for the performance of the motor. The displacement is given by the design and dimensions of the motor, while the efficiency is influenced by several factors.

3.1 Efficiency of Hydraulic Motors

In general, energy is transfered from the hydraulic fluid to rotational energy in hydraulic motors, given by

$$\Delta p \cdot Q \cdot \eta = T \cdot \omega, \tag{3.1}$$

where Δp is pressure drop across the motor, Q is flow into the motor, T is torque, ω is rotational speed of the output shaft and η is the total efficiency of the motor. The total efficiency, η, can be further divided into a volumetric efficiency, η_{vol}, and a hydromechanical efficiency, η_{hm}. The volumetric efficiency, η_{vol}, is the relation between the input flow and the actual velocity of the motor, which is given by

$$Q \cdot \eta_{vol} = \frac{D \cdot \omega}{2\pi}, \tag{3.2}$$

where D is the displacement of the motor.
The hydromechanical efficiency, η_{hm}, is the relation between the pressure difference inside the motor and the actual torque of the output shaft, which is given by

$$\Delta p \cdot \eta_{hm} = \frac{T \cdot 2\pi}{D}. \tag{3.3}$$

Hence, the relation between the efficiencies is

$$\eta = \eta_{vol} \cdot \eta_{hm}. \tag{3.4}$$

In equation 3.1 - 3.4 the efficiencies are just denoted by a symbol, but they depend on several parameters and the operational conditions of the hydrostatic motor.

When talking about the efficiencies of hydrostatic motors, it is sometimes easier to use the term loss. Because all the individual, and detectable, losses are those giving the efficiencies.

The volumetric loss of hydrostatic motors is mainly due to leakage flow from high pressure volumes to low pressure volumes. The other contribution is compression of the hydraulic fluid, which is considered negligible in this study. The leakage flow, Q_{leak}, in the internal gaps of the motor, which also has a lubricating function, is given by

$$Q_{leak} = C_{leak} \cdot \frac{\Delta p}{\mu}, \tag{3.5}$$

where μ is viscosity of the oil and C_{leak} is a leakage parameter that takes into account the production tolerances, i.e. the geometry of all the internal clearances of the motor.

The hydromechanical loss, or torque loss, of hydrostatic motors is due to friction forces. The friction loss depends on both the tribology of all the surfaces that move relative to each other inside the motor and the operational parameters of the motor. The operational parameters are angular velocity, ω, pressure, p, and viscosity, μ. The total torque loss, T_{loss}, of hydrostatic motors is given as, Ivantysyn and Ivantysynova (2003)

$$\begin{aligned} T_{loss} &= T_{turb} + T_{visc} + T_{mech} + T_{cst} \\ &= C_{turb} \cdot \mu \cdot \omega^2 + C_{visc} \cdot \mu \cdot \frac{\omega}{h} + C_{mech} \cdot \Delta p + C_{cst}, \end{aligned} \tag{3.6}$$

where C_{turb} is a loss parameter that accounts for turbulent friction due to turbulent fluid flow around restrictions, bends, etc. C_{visc} is taking the laminar friction into account. It is due to shearing of the fluid film between parts that move relative to each other. C_{mech} is a parameter that describes the mechanical friction inside the motor. C_{cst} is the static friction loss due to sealings.

As given by the loss parameters and the influence from the operational parameters of equation 3.5 and 3.6, the total loss behaviour of hydrostatic motors is both complex and nonlinear.

Both the volumetric losses and the hydromechanical losses depend of the internal gaps of hydrostatic motors. Therefore the height of these gaps and the lubricating conditions inside them are very important factors for the total efficiency. They have two contradicting functions, which is sealing and lubrication. If the gap height increases, the volumetric loss will increase, but the friction loss decrease. If the gap height get smaller it is opposite. Hence, the total efficiency of hydraulic displacement machines is a compromise between volumetric loss and hydromechanical loss. The general trend is that if the volumetric loss goes down the hydromechanical loss goes up.

All the major losses inside hydrostatic motors depend on the gaps between the moving parts, in a complex and nonlinear relationship. This is further complicated by the fact that some gap heights are influenced by structural deflections of the faces that form the gap. These structural deflections are due to the hydrostatic pressure in the lubricating gap, which again depends on the operating pressure of the motor.

3.2 State of Art within the Design of Hydrostatic Displacement Machines

As described in the previous section, the efficiency of hydrostatic motors are complex. Equation 3.5 and 3.6 are general loss formulas, whereas the loss parameters are individual for different kind of motors and for different motor sizes. Furthermore, the efficiency level highly depends on the manufacturing of the motors. Both the initial gap heights and the roughness of the surfaces are due to the manufacturing. But the need of building prototypes to determine the efficiencies during a development phase, is both time consuming and expensive. Therefore, more model based design tools are requested, which has been of interest for several researchers during the history.

Except for the seperation of volumetric and hydromechanical losses, there exist no unique modeling techniques that describe the losses in hydrostatic machines in detail, Ivantysyn and Ivantysynova (2003). The complex behaviour and influence from the tribological system of hydrostatic machines, prevents a model based prediction of the performance. Therefore, the design of hydrostatic machines rely on excessive testing of volumetric and hydromechanical losses for the entire operating range, see Ivantysyn and Ivantysynova (2003), Ivantysynova (2003) and Murrenhoff et al. (2008). Though, more researchers have contributed to the mathematical loss modeling.

The conceptuel behaviour of the torque loss is described in equation 3.6. The loss coefficients C are those varying for different torque loss models, different motor sizes and principles. In the litterature these coefficients were first given as constants, Wilson (1946). Later on it was shown, McCandlish and Dorey (1984), that both linear and nonlinear loss coefficients give more accurate results over a wider range of operating conditions. Besides from the two mentioned papers, many mathematical torque loss findings have been published, in e.g. Hibi and Ichikawa (1977), Conrad et al. (1991), Ivantysynova (1999), Inaguma and Hibi (2005), Murrenhoff et al. (2008) and Inaguma (2011). The main difference of the existing models are in the mathematical description of the individual losses Ivantysynova (2003). Generally, a higher accuracy can be achieved if the loss coefficients are expressed as polynomials. Some use polynomials of higher order, which makes it difficult to relate particular loss coefficients to physical effects McCandlish and Dorey (1984).

3.3 Volumetric Loss of the Hydrostatic Motor

The motor of interest in this project is catagorized as a low speed high torque motor. For this kind of motor the volumetric efficiency calls for special attention. This is further justified by the intended size of the motor (section 1.4.2). Hence, the machining of the fine tolerance surfaces gets more complex and the structural deflections to a wide range of operating conditions are more difficult to minimize without adding too much weight.

Leakage flow occurs several places in the motor from the high pressure volumes to the low pressure volumes (see figure 2.1). E.g. around the vanes and the stops and between the SOI into the drain connection. Furthermore, the oil flowing into the low pressure side of the vane actuation system (section 2.2) is volumetric loss. But the only flow of interest in this section is the leakage flow between the SOI. Both according to theory and measurements, it is by far, the biggest source to volumetric loss. Hence, it is practically the volumetric loss of the motor that is controlled by the compensation pressure. The modeling of the leakage flow between the SOI is described in this section and in Sørensen et al. (2012*b*).

3.3.1 Pressure Distribution in the Lubricating Gaps

The gap heights between rotor and housings, called SOI (se figure 2.5), depend of the pressure distribution in the two gaps (one on each side of the rotor). These pressure distributions are given by Reynolds equation for fluid film lubrication. The general Reynolds equation is, Hamrock et al. (2004)

$$\begin{aligned} 0 &= \frac{\partial}{\partial x}\left(-\frac{\rho \cdot h^3}{12 \cdot \mu} \cdot \frac{\partial p}{\partial x}\right) + \frac{\partial}{\partial y}\left(-\frac{\rho \cdot h^3}{12 \cdot \mu} \cdot \frac{\partial p}{\partial y}\right) \\ &+ \frac{\partial}{\partial x}\left(\frac{\rho \cdot h \cdot (u_m + u_n)}{2}\right) + \frac{\partial}{\partial y}\left(\frac{\rho \cdot h \cdot (v_m + v_n)}{2}\right) \\ &+ \rho \cdot (w_m - w_n) - \rho \cdot u_m \cdot \frac{\partial h}{\partial x} - \rho \cdot v_m \cdot \frac{\partial h}{\partial y} + h \cdot \frac{\partial \rho}{\partial t}, \end{aligned} \tag{3.7}$$

where ρ is density, h is gap height, p is pressure, μ is viscosity, u, v and m are velocity and t is time. Subscript m denotes the surface of body m and subscript n denotes the surface of body n, see figure 3.1).

The two first terms of equation 3.7 are called the Poiseuille terms. They describe the flow rate due to pressure gradients within the lubricated area. The third and fourth terms are called the Couette flow. They describe the flow rate due to the velocities of the surfaces that form the lubricating gap. The fifth to seventh terms describe the flow rate due to a squeezing motion. The fifth term is the normal squeeze term that happens if the gap height is changed if the surfaces are pressed together or away from each other. The sixth and seventh terms are the translation squeeze terms, which are the action from a translation of inclined surfaces. The last term is called local expansion term and arises from a thermal expansion of the

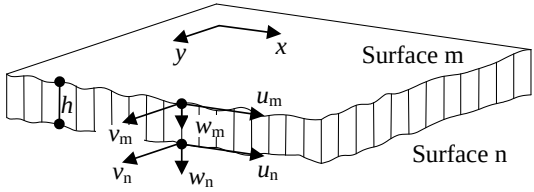

Figure 3.1: Illustration of the fluid film between surface m (housing) and surface n (rotor). Sørensen et al. (2012*b*)

fluid.

In this study it is assumed that the rigid body motion of the rotor is only rotational and axial, and that the density and viscosity of the fluid are constant. Because of the circular shape of the rotor and the rotational velocity, equation 3.7 can, usefully, be translated into polar coordinates. Hence, the pressure distribution in the gaps between SOI is, Beschorner et al. (2009) and Ivantysynova and Baker (2009)

$$\frac{\partial}{\partial r}\left(r \cdot h^3 \cdot \frac{\partial p}{\partial r}\right) + \frac{1}{r} \cdot \frac{\partial}{\partial \theta}\left(h^3 \cdot \frac{\partial p}{\partial \theta}\right) = 6 \cdot \mu \cdot r \cdot \omega \cdot \frac{\partial h}{\partial \theta} + 12 \cdot \mu \cdot r \cdot \frac{\partial h}{\partial t}. \quad (3.8)$$

In Sørensen et al. (2012*b*) and Sørensen et al. (2012*a*) equation 3.8 is solved numerically using the finite difference method (FDM) for one rotor position. In this method the lubricating area is divided into elements (mesh) and the derivatives of equation 3.8 is approximated by finite differences. Hence, the pressure in all nodes, $p_{i,j}$, is expressed by its surrounding pressures and are determined by looping through the mesh until the pressure variation from previous iteration is smaller than a specified convergence tolerance. This pressure distribution is the input for the structural calculations, which return an updated gap height. Again, this updated gap height serves as input to the next calculation of pressure distribution. These coupled fluid structural interaction (FSI) simulations are continued until the pressure variation from previous iteration is smaller than a specified convergence tolerance. A converged pressure distribution between the SOI is shown in figure 3.3 to one test condition of the prototype motor.

This present rotor position (the one shown on figure 2.1) is representing a mean resulting force of the fluid pressure. The deviations to other rotor positions is considered negligible for the results of this study.

3.3.2 Structural Deflections of the Surfaces of Interest

For the determination of the volumetic loss, which is equal the leakage flow, the gap heights between the SOI is essential. The structural deflections that influence

the leakage flow is determined by FEM simulations. The used FEM model is shown in figure 3.2 with the boundary conditions and the applied loads included. The applied mesh is omitted in figure 3.2, to decrease the detail level.

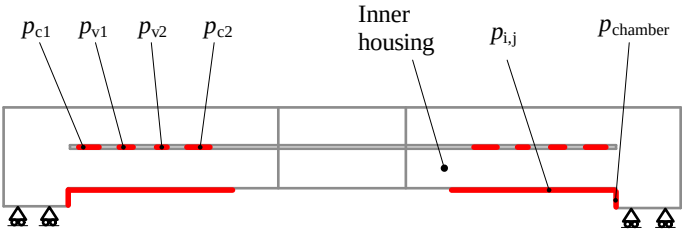

Figure 3.2: A section view of the FEM model with pressures and boundary conditions denoted. Sørensen et al. (2012*a*)

The input to the FEM simulations is the pressure distribution in the gaps between the SOI ($p_{i,j}$ in figure 3.2). They are updated to each iteration, as described in section 3.3.1. The added vane actuation pressures and the compensation pressures are constant, but very important for the overall deflection behaviour of the parts. All the pressures are applied as nodal forces in the FEM simulations. They are given by

$$F_{i,j} = p_{i,j} \cdot r_{i,j} \cdot \Delta r \cdot \Delta \theta, \tag{3.9}$$

where F is force, p is pressure, r is radius, Δr is the radial element division of the mesh and $\Delta \theta$ is the tangential element division of the mesh. Subscript i denotes the i'te node in radial direction and subscript j is the j'te node in tangential direction.

The interaction between the fluid and the structural calculations is managed by text files. In the beginning of the fluid sequence of the simulation, a text file with the current gap height for each node is read. In the end, the updated node pressures is written to a text file. For the structural sequence the order is opposite. The node pressures are read from a text file and the node deflections are written to a text file.

The enabling of the coupling of the fluid and the structural calculations, is because of a manually mesh generation. Hence the applied mesh, element numbering and node numbering is the same for both the fluid and the structural simulations. Then the regularly interchange of state variables is fast.

The simulated deflection of the faces between the SOI to one test condition of the prototype motor is shown in figure 3.3.

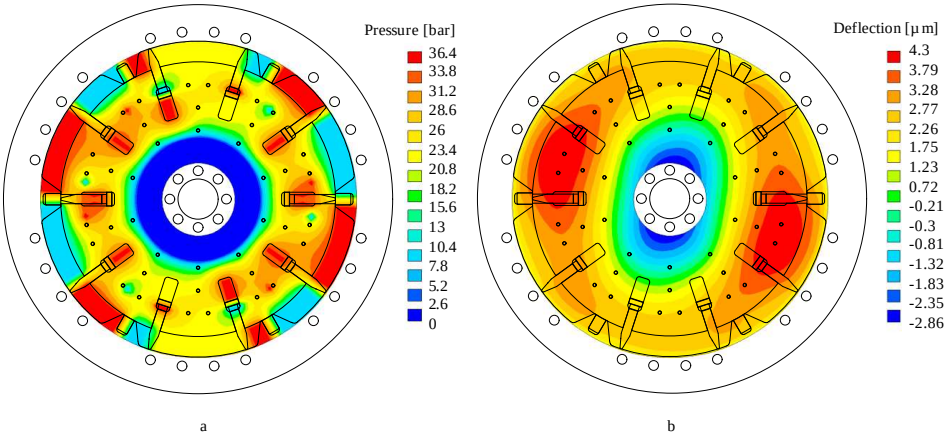

Figure 3.3: The simulated pressure distribution (a) and the deflection of the inner housing (b) to one test condition of the prototype motor. Sørensen et al. (2012*a*)

3.4 Hydromechanical Loss

The hydromechanical loss is difficult to model in a simple way since it depends on a wide variety of friction losses. They include laminar and turbulent flow induced pressure drops in the displaced fluid as well as a combination of friction caused by boundary layer, mixed layer and elastohydrodynammic lubrication between moving parts. These phenomena depend on the operating conditions as well as the topology and geometry of the hydrostatic machine.

The complex behaviour of the hydromechanical loss complicates a model based prediction of the performance. Therefore the design of hydrostatic machines rely heavily on fine machining tolerances and an excessive testing to determine the friction behaviour of the specific machine. In general, experimental results are the basis of torque loss models, Ivantysyn and Ivantysynova (2003), Ivantysynova (2003), Murrenhoff et al. (2008).

The most important detail of the motor, with regard to loss, is the gap between the SOI. This gap height is influenced by the operational pressures of the motor and the compensation pressures (described in section 2.3). The aim of the compensation pressures is to decrease the structural deflections of the SOI, and thereby decrease the volumetric loss across the end faces of the rotor. But this decrease of deflection is a trade of between volumetric and hydromechanical loss. Because still, the SOI have to be seperated by an oil film to avoid an introduction of mechanical friction and thereby a potential increase of the total loss and wear of the sliding surfaces. The impact of the compensation pressures with regard to the friction loss of the motor is the subject of Sørensen et al. (2012*a*).

The aim of Sørensen et al. (2012*a*) was not to determine an optimal compensation pressure level, which would keep the total losses of the motor at a minimum. But instead to investigate the impact of different compensation pressure levels, with regard to deflections and friction losses related to the SOI.

3.4.1 Torque Loss of the Prototype Motor

The total torque loss of the prototype motor and the corresponding gap heights, measured at the circle of the MCA location, are plotted in figure 3.4. The graphs are based on different load scenarios with different compensation pressures. Both graphs are with the high pressure of the motor along the x-axis. The torque loss, T_{loss}, is given by

$$T_{loss} = T_{th} - T_{out} = \frac{\Delta p \cdot D}{2\pi} - T_{out}. \tag{3.10}$$

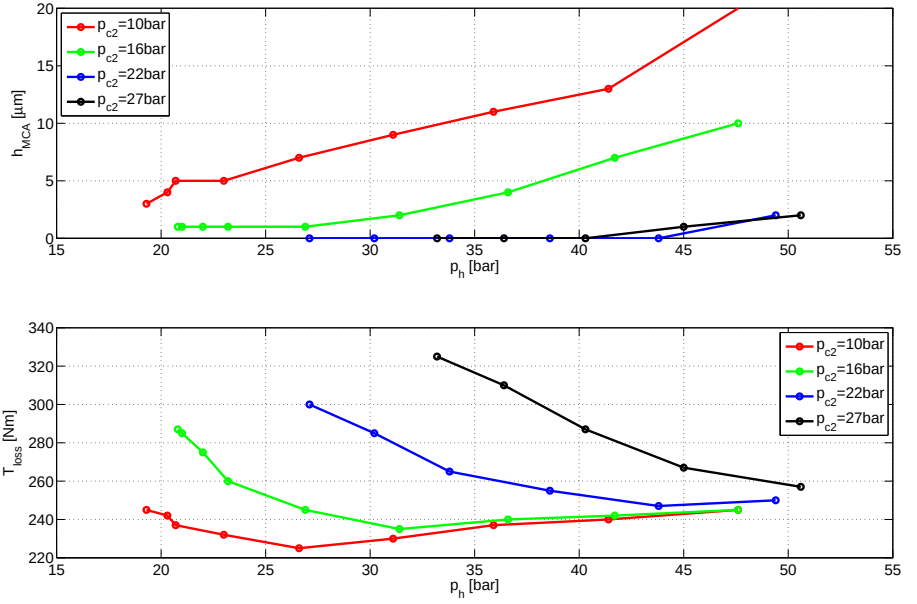

Figure 3.4: Experimental measurements on the prototype motor. h_{MCA} is deflection of the SOI, T_{loss} is total torque loss. p_h is the working pressure of the prototype and p_{c2} is the adjustable compensation pressure. Sørensen et al. (2012*a*)

The trend of the hydromechanical loss T_{loss} in figure 3.4 is clear. For all four p_{c2} values, T_{loss} is decreasing with the increase in p_h, until reaching a minimum, called $T_{loss,min}$. After $T_{loss,min}$, T_{loss} is increasing almost linearly with p_h. $T_{loss,min}$ is changing for the four different p_{c2} values. And for the $p_{c2} = 27bar$ graph $T_{loss,min}$ is outside the range of the measurements. The hypothesis is that before $T_{loss,min}$ there are asperity contacts and therefore mechanical friction between the SOI.

The friction loss between the SOI depends on the normal force between the surfaces. This force decreases when p_h increases. After $T_{loss,min}$ the lubricating regime between SOI is elastohydrodynamic (EHL) and the related friction loss is due to oil shearing. Hence, the dominating torque loss in the motor, from mechanical friction, is caused by the vane-stator and stop-rotor contacts, which increase with p_h. The measured h_{MCA} are in agreement with the just proposed loss behaviour. The gap height increase with p_h and the compensation pressure p_{c2} has a significant effect on h_{MCA}. The trend of the h_{MCA} curves in figure 3.4 is that the gap pressure between SOI has to overcome the compensation pressures before the gap height starts to increase with p_h. The h_{MCA} measurements are in μm which implies some uncertainties due to the roughness of the rotor surfaces (surface asperities) and thickness variations in the same order of magnitude. E.g. this can explain why the $p_{c2} = 27bar$ curve is not below the curve for $p_{c2} = 22bar$. It is expected that the curve for $p_{c2} = 27bar$ does not start to increase inside the pressure range of the tests. Furthermore, the h_{MCA} measurements cannot reflect when the surfaces are fully separated. It only measure along a certain radius of the rotor.

It is expected that $T_{loss,min}$ occurs when the minimum gap height between SOI is just above zero for the entire area. But due to an uneven height distribution over the SOI, the gap height for the entire SOI is not zero or above zero, when h_{MCA} starts to measure deflections above zero.

3.4.2 Identification of Torque Loss

The conceptual behaviour of the torque loss of hydrostatic displacement machines is described in equation 3.6. In the measurements behind the graphs in figure 3.4, the velocity and viscosity are held constant. In that case equation 3.6 reduces to

$$T_{loss} = C_{visc} \cdot \mu \cdot \frac{\omega}{h} + C_{mech} \cdot \Delta p + C_1, \tag{3.11}$$

where C_1 is the constant torque loss to a given velocity and viscosity. The term $C_{mech} \cdot \Delta p$ includes the mechanical friction between vane-stator and stop-rotor. The term $C_{visc} \cdot \mu \cdot \omega / h$ describes the torque loss due to viscous friction between the SOI. This term relies on that SOI remains separated and without mechanical contact. But, according to measurements (see figure 3.4), there exists mechanical contact between SOI. The friction loss in the gaps between SOI highly depends on the gap height, and therefore the compensation pressures. Therefore, the torque loss of the prototype motor, when constant velocity and temperature, is subdivided into

$$\begin{aligned} T_{loss} &= T_{cst} + T_{mech} + T_{SOI} && (3.12) \\ &= K_1 + K_2 \cdot \Delta p + T_{SOI}, && (3.13) \end{aligned}$$

where K_1 and K_2 are loss coefficients derived from measurements.

On the basis of the measurements (figure 3.4) it is evident that there is a transition in the lubrication regime between SOI, around $T_{loss,min}$. Depending on the pressure state the lubricating regime will, in general, go from boundary lubrication (BL) to mixed lubrication (ML) and then towards elastohydrodynamic lubrication (EHL). The relation between the shear friction τ_{fric} and the different friction regimes is given by the Stribeck curve, see figure 3.5. From the T_{loss} and h_{MCA} curves in figure 3.4 it seems that the friction regime between SOI is ML and at the beginning of EHL during the tests.

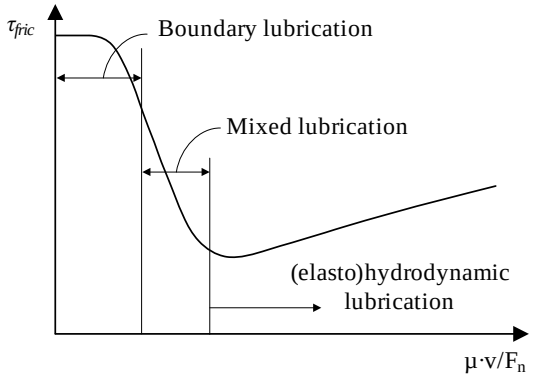

Figure 3.5: Stribeck diagram with lubrication regimes.

The friction in the Stribeck diagram of figure 3.5 is based on viscosity, μ, relative velocity, v, and normal force, F_n, between the gap surfaces Bayer (1994). Since the velocity and viscosity are constant during the tests, the friction loss variations only depend on normal force, according to figure 3.5. But there is only a normal force between SOI when the gap height is zero in some areas. Even if the gap height is above zero, there is potentially still asperity contacts, and therefore mechanical friction, due to the roughness of the surfaces. From that point of view, the normal force is not a valid parameter for the determination of the friction loss behaviour in this study. Instead, the gap height and the deflection of SOI are the parameters that influence the friction behaviour Wang and Wang (2006).

3.4.3 Torque Loss based on Gap Height

The gap height distribution between SOI is determined by the FSI simulation model, as described in section 3.3. Here, the finite difference model, that determines the pressure distribution, is numerically limited in the way that it only converges when all gap heights are above a small threshold value, $h_\epsilon \approx 2nm$. Hence, for any FSI simulation the inner housing and the rotor are given a position that ensures $h_{min}^{FSI} > h_\epsilon$ to any load situations, see figure 3.6.

The gap height from the FSI simulation is only valid for situations where the SOI are fully separated. To be able to include situations where the SOI are partly

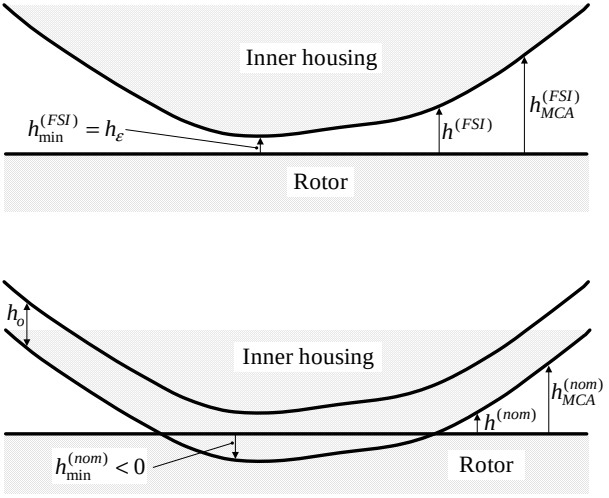

Figure 3.6: Illustration of $h^{(nom)}$, $h^{(FSI)}$ and h_o. Sørensen et al. (2012*a*)

separated or not separated at all, an offset gap height h_o is introduced, see figure 3.6. This offset value is subtracted from the FSI gap height to give the nominal gap height

$$h^{nom} = h^{FSI} - h_o. \tag{3.14}$$

The offset gap height, h_o, is identified by fitting the nominal gap height with the measured gap height by the MCA in situations where the SOI are fully separated, which gives $h_o = 7.5\mu m$, Sørensen et al. (2012*a*).

The total shear stress, τ_{fric}, in the ML regime is given by the sum of the shear stress of the asperity contacts, τ_{asp}, and the sharing of the oil, τ_{fluid}, as Gelinck and Schipper (2000)

$$\begin{aligned} \tau_{fric} &= \tau_{asp} + \tau_{fluid} \\ &= \mu_{fric}(h') \cdot p' + \mu \cdot \frac{v}{h'}, \end{aligned} \tag{3.15}$$

where $\mu_{fric}(h') \cdot p'$ is the shear stress of the asperity contacts and $\mu \cdot \frac{v}{h'}$ is the shear stress of the fluid. The friction coefficient function, $\mu_{fric}(h')$, is a function of the gap heights, h', given by

$$\mu_{fric}(h') = K_3 \cdot e^{-\frac{h'-h_{thr}}{h_{thr}}}, \tag{3.16}$$

where h_{thr} is a threshold gap height that determines if there is mechanical contact. p' and h' are defined as

$$h' = \begin{cases} h_{thr} & \text{if } h^{(nom)} < h_{thr} \\ h^{(nom)} & \text{if } h^{(nom)} \geq h_{thr} \end{cases}, \tag{3.17}$$

$$p' = \begin{cases} p - K_4 \cdot h^{(nom)} & \text{if } h^{(nom)} < h_{thr} \\ p & \text{if } h^{(nom)} \geq h_{thr} \end{cases} . \tag{3.18}$$

Singularities are avoided by the introduction of h' which gives a smooth transition from ML to EHL. Negative values of h^{nom} correspond to a certain amount of indentation of the SOI. This is taken into account by the simple linear stiffness that is introduced in equation 3.18. This is considered adequate to capture the increase in contact pressure between the asperities.

Hence, the total simulated torque loss of the prototype motor, T_{loss}^{sim}, when constant velocity and viscosity, is

$$\begin{aligned} T_{loss}^{(sim)} &= T_{cst}^{(sim)} + T_{mech}^{(sim)} + T_{SOI}^{(sim)} \\ &= K_1 + K_2 \cdot \Delta p + \tau_{fric} \cdot A \cdot r, \end{aligned} \tag{3.19}$$

where A is area and r is radius.

3.5 Summary of Contributions

This chapter presented simulation models of the motor. The contributions are:

- A finite difference model was established to compute the pressure level between the SOI.
- A link to a FEM model was established that allow a FSI simulation to be carried out.
- Models for volumetric and hydromechanical losses were developed.

4

Results

The aim of this chapter is to present the overall results of this project. The results relate to the theoretical modeling and the related experimental verification and to the general performance of the prototype motor.

4.1 Volumetric Loss

The results of the study of the volumetric loss are described in Sørensen et al. (2012*b*). The conclusions of the paper are that the overall volumetric loss of the prototype motor depends on the compensation pressure and that the simulation model reflects the measurements. Furthermore, the paper emphasizes that a force that counteract the structural deflections of the SOI, is essential for a functioning prototype.

In Sørensen et al. (2012*b*) simulated gap heights are compared with measured gap heights (measured with the MCA). The MCA has a resolution of $0.1\mu m$ and there is a good consistency with the simulated deflections. This is also emphasized with a comparison of the simulated and measured flow through the drain connections. The drain flows are plotted with regard to the gap heights at the radius where the MCA is mounted. These curves show an exponential relationship between the drain flow and the gap height, as expected according to the theory.

4.2 Torque Loss

The torque loss study of the project is described in Sørensen et al. (2012*a*). The lubricating regime between the SOI and the effects of the compensation pressure are the focus of the paper. The study is based on measurements where the lubricating regime between the SOI goes from mixed lubrication to elastohydrodynamic lubrication, which depends on the compensation pressure. In other words, the friction regime between the SOI is controlled by the compensation pressure.

The friction loss behaviour follows a Stribeck curve and the friction modeling of

the gap between the SOI is based on gap height. The simulation model includes all friction losses in the prototype motor. The loss coefficients are constants and their value are determined by parameter identification by the use of experimental measurements. The outcome is a simulation model that reflects the behaviour of the prototype. There is a good correlation between the simulated and the measured torque loss.

4.3 Total Efficiency of the Prototype Motor

As written previously, the aim of this project was not to optimize the dimensions and parameters of the new motor principle. Instead, the aim was to investigate the motor principle through simulation models and examine if the motor efficiencies could be on an acceptable level.

The studies regarding both the volumetric loss and the hydromechanical loss show that the compensation chambers are of big influence on the efficiencies of the prototype motor. The motor principle is, of nature, vulnerable against structural deflection. If the performance critical deflections should be minimized just by adding enough stiffness to the structure, it would be a very heavy construction. Furthermore, the compensation pressures open up for a control of the gap heights, and therefore the friction regime, between the SOI.

As described, the pressure level of the compensation pressures has not been optimized. Instead, it has only been adjusted to an acceptable level. The effect of the compensation pressure level is illustrated in figure 4.1. The figure shows measured pressures, output torque, rotor velocity and efficiencies during a characteristic test sequence. The rotational direction, input flow and the loading on the motor are constant. Only the compensation pressure is adjusted. It is varied between approximately $22bar$ and $8bar$. Still, the output torque is constant, but the velocity of the rotor decreases with the decrease in compensation pressure. The gap height between the SOI increases and so does the leakage flow. This is also evident by the decrease in volumetric efficiency, η_{vol}, as given by the lower graph in figure 4.1.

Throughout the test sequence in figure 4.1, the lubricating regime between the SOI is considered elastohydrodynamic. There is no transition in the friction loss (the graph for the hydromechanical efficiency), when the compensation pressure is varied. Hence, the total efficiency of the prototype motor could maybe be increased, to the given loading, just by increasing the compensation pressure to more than the $\approx 22bar$ limit in the test sequence.

For commercial hydrostatic motors, the total efficiency is indicated by three dimensional level curves, with the total efficiency given as a function of the present velocity and torque of the motor. To be able to evaluate the performance of the prototype of this project, the total efficiency is illustrated in figure 4.2 by a colour

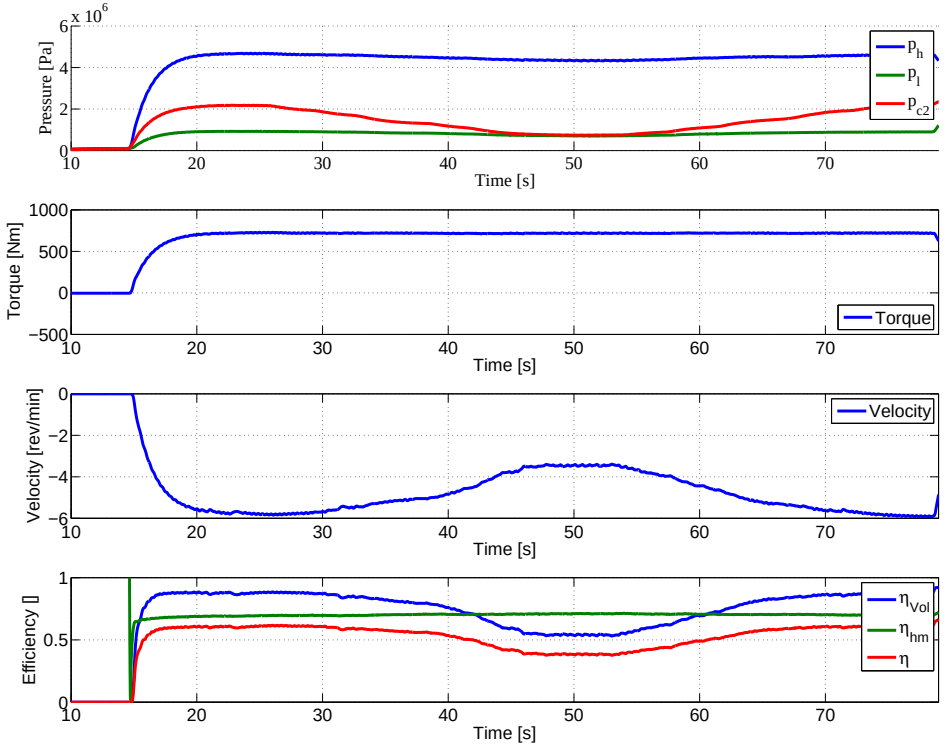

Figure 4.1: The effect of varying the compensation pressure with regard to the efficiencies for a characteristic test sequence.

plot. The plot is created from a number of tests, after which there is interpolated between the measurement points. All these tests are with the same compensation pressure on max $28bar$. I.e, the compensation pressure follow the high pressure up until $28bar$, after which it maintains this value.

It is noticeable that the highest total efficiency ($\eta \approx 0.65$) is in the highest torque range of the measurements. The reason for this is limitations in the test setup. Higher torques ($> 1000Nm$) would break the couplings of the test setup. Although the max pressure of the prototype was far from the max. During the tests behind the plot of figure 4.2, the max pressure was below $60bar$.

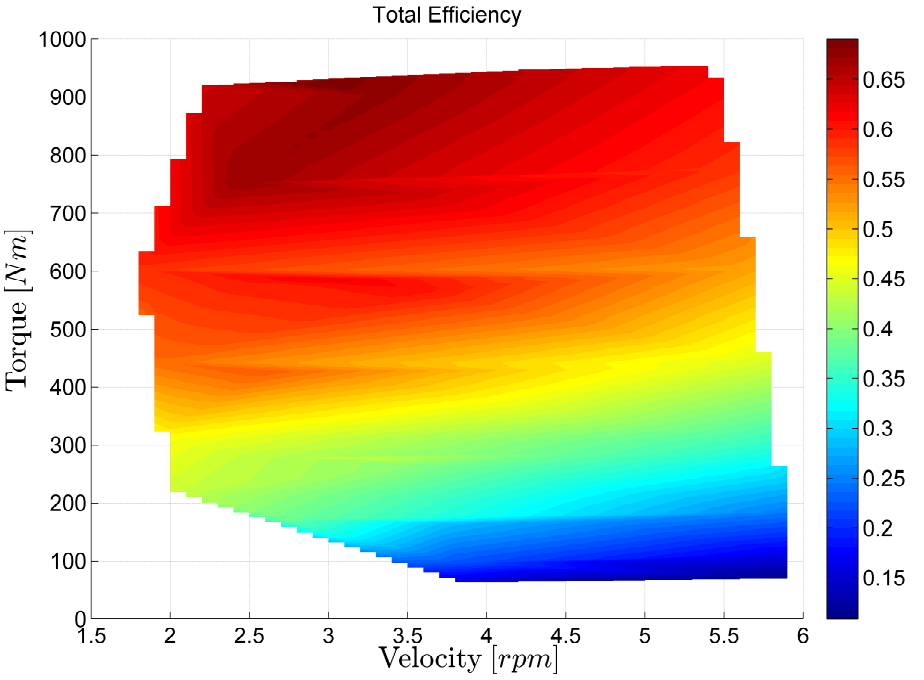

Figure 4.2: Total efficiency of the prototype motor. All the measurements behind the colourplot are with the same compensation pressure level.

4.4 Summary of Contributions

This chapter presented the results of the project. The contribution are:

- A good correlation was, in general, obtained between simulated data, measured data, and the general theory within leakage and friction.
- The efficiencies of the motor can be adjusted by the compensation pressure level.
- The prototype is capable of maintaining quite good efficiencies within certain loading conditions.

5

Conclusions

The objective of the research work was the development of a new type of hydrostatic motor. In this context development covers prototype design and the development of models to describe variations in efficiency performance.

The efficiencies of the motor principle put forward in this project is highly influenced by structural deflections caused by internal fluid pressures. However, these deflections can be minimized and kept almost constant over a wider range of operating conditions, by the addition of compensation pressures. The deflections of interest and the corresponding compensation pressures are examined through prototype testings and FSI modeling with the aim of an identification of the loss characteristic.

The compensation pressures must be applied carefully to minimize the volumetric losses without causing excessive torque losses by spoiling the lubricating film. The FSI model describes the torque losses associated with mechanical and viscous friction under different lubricating conditions. The behaviour of the friction loss follows that of the Stribeck curve which only changes with the gap height in this project. This gap height dependency ensures an acceptable calculation time compared with the use of nonlinear contact elements when evaluating asperity contact forces.

The coefficients of the developed friction loss model are determined by prototype measurements. There is a good correlation between the numerical and experimental results, both with regard to the volumetric and the torque losses. Furthermore, the theoretical and experimental work are complementing one another in the detective work regarding troubleshooting and the explaination of all the different motor behavior during the project. Discrepancies between theory and prototype measurements have been balanced by either an extension of the simulation model and/or more test data.

Contributions

The main scientific contributions within the research work regarding a model based approach for the development of hydraulic displacement machines are the

following:

- Proof of concept of new hydraulic motor principle. At this pre-step of the product development phase the total efficiency of the prototype motor is proven satisfactorily, especially when taking into account that no special measures were applied in order to further improve it.
- Introduction of pressure compensation adjustment that stabilizes the deflections and losses over a wider range of operating conditions. Furthermore, by controlling these compensation pressures, the sharing of volumetric loss and torque loss can be adjusted.
- Development of a FSI simulation model to examine the effect of structural deflections on the efficiencies.
- Establishment of the torque loss model based on gap heights. The friction losses are highly motor dependent due to the influence of operating conditions as well as the topology and geometry of the hydrostatic machine.
- The ability to measure the structural deflections of concern of the prototype motor and their accordance with the simulated deflections.

Recommendations for Further Work

Here some recommendations are given for further research topics related to the discoveries of this project.

A study regarding an optimization of the number of vanes and chambers. The FSI simulation model can serve as a part of the objective function by an evaluation of efficiencies. E.g. the prototype motor is with 10 vanes, 6 chambers and a displacement of $1.75 l/rev$. What will happen if it have 8 chambers and 12 vanes instead? The displacement is increased for the same outer dimensions. But how will the efficiencies evolve when changing these specifications? Will the losses increase correspondently or will the efficiencies change? This study could turn out to a more general optimization of the motor. An optimization with several optimization parameters such as dimensions, tolerances and specifications can examine the tendencies and performance improvements.

Another apparant optimization topic is the compensation pressure. The counteracting forces that are preventing the critical deflections are proportional to the area. An optimization study of this area can maybe increase the range of operating pressures with an acceptable efficiency. And it can determine the dependency between operating pressures, compensation pressure, compensation area and structural deflections. Again, the FSI simulation model can serve as the calculation basis.

Bibliography

Bayer, R.G. (1994), *Mechanical Wear Prediction and Prevention*, Marcel Dekker.

Beschorner, K., C.F. Higgs and M. Lovell (2009), 'Solution of reynolds equation in polar coordinates applicable to nonsymmetric entrainment velocities', *Journal of Tribology* **131**.

Conrad, F., P.H. Sørensen and E. Trostmann (1991), 'On the loss functions in hydrostatic machines', *Presented at the ASME Winter Annual Meeting* .

Fenger, Per E. (2010), 'Hydraulic motor or pump', Patent, 09 2010. WO 2010097086.

Gelinck, E.R.M. and D.J. Schipper (2000), 'Calculation of stribeck curves for line contacts', *Tribology International* **33**, 175–181.

Hamrock, B.J., S.R. Schmid and B.O. Jacobsen (2004), *Fundamentals of Fluid Film Lubrication*, second edn, Marcel Dekker.

Hibi, A. and T. Ichikawa (1977), 'Mathematical model of the torque characteristics for hydraulic motors', *Bulletin of the JSME* **20**(143).

Inaguma, Y. (2011), 'Friction torque characteristics of an internal gear pump', *Proceedings of the Institution of Mechanical Engineers, Part C: Journal of Mechanical Engineering Science* **225**.

Inaguma, Y. and A. Hibi (2005), 'Vane pump theory for mechanical efficiency', *Proceedings of the Institution of Mechanical Engineers, Part C: Journal of Mechanical Engineering Science* **219**.

Ivantysyn, J. and M. Ivantysynova (2003), *Hydrostatic Pumps and Motors: Principles, Design Performance, Modelling, Analysis, Control and Testing*, Tech Books International.

Ivantysynova, M. (1999), 'Ways for efficiency improvements of modern displacement machines', *The Sixth Scandinavian International Conference on Fluid Power* .

Ivantysynova, M. (2003), 'Prediction of pump and motor performance by computer simulation', *First International Conference on Computational Methods in Fluid Power Technology* .

Ivantysynova, M. and J. Baker (2009), 'Power loss in the lubricating gap between cylinder block and valve plate of swash plate type axial piston machines', *International Journal of Fluid Power* **10**(2), 29–43.

McCandlish, D. and R.E. Dorey (1984), 'The mathematical modelling of hydrostatic pumps and motors', *Proc Instn Mech Engrs* **198B**(10).

Murrenhoff, H., U. Piepenstock and T. Kohmäscher (2008), 'Analysing losses in hydrostatic drives', *Proceedings of the 7th JFPS International Symposium on Fluid Power* .

Sørensen, Rasmus M., Michael R. Hansen and Ole Ø. Mouritsen (2012*a*), 'Numerical and Experimental Study of Friction Loss in Hydrostatic Motor', *Modeling, Identification and Control* **33**(3), 99–109.

Sørensen, R.M., M.R. Hansen and O.Ø. Mouritsen (2011), 'Hydraulic yaw system for wind turbines with new compact hydraulic motor principle', *EWEA 2011 Scientific Proceedings* pp. 111–114.

Sørensen, R.M., M.R. Hansen and O.Ø. Mouritsen (2012*b*), 'Numerical and experimental study of hydrostatic displacement machine', *International Journal of Fluid Power* **13**(2), 29–40.

Stubkier, S. (2013), *Hydraulic Soft Yaw System for Multi MW Wind Turbines*, Department of Energy Technology, Aalborg University.

Wang, Y. and Q.J. Wang (2006), 'Development of a set of stribeck curves for conformal contacts of rough surfaces', *Tribology Transactions* **49**, 526–535.

Wilson, W.E. (1946), 'Rotary pump theory', *Transaction of the ASME* pp. 371–383.

Paper A

Numerical and Experimental Study of Hydrostatic Displacement Machine
Rasmus M. Sørensen, Michael R. Hansen, Ole Ø. Mouritsen
Published in *International Journal of Fluid Power* 13 (2012) No. 2 pp 29-40

Numerical and Experimental Study of Hydrostatic Displacement Machine

Rasmus M. Sørensen*, Liftra & Department of Mechanical and Manufacturing Engineering, Aalborg University, Denmark
Michael R. Hansen, Department of Engineering, University of Agder, Norway
Ole Ø. Mouritsen, Department of Mechanical and Manufacturing Engineering, Aalborg University, Denmark

Abstract

This paper presents a simulation tool to determine the structural deflections and corresponding leakage flow in a hydrostatic displacement motor. The simulation tool is applied to a new motor principle that is categorized as an extreme low speed high torque motor with dimensions that calls for attention to the volumetric efficiency. To counteract structural deflections the motor is equipped with compensation pressure volumes that may be used to limit the leakage flow across the end faces of the circular rotor. This leakage flow is investigated by solving Reynolds equation for the pressure distribution across both end faces. The fluid pressure is combined with structural calculations in a fluid structural interaction simulation which evaluates the influence of structural deflections on the gaps and the leakage flow.

The numerical work is validated by prototype tests. Both deflections and leakage flows are measured and compared with those from the simulations with good correlation. The deflections, and hence leakage flow, are reduced by the use of compensation pressure volumes, which is validated both numerically and experimentally.

Keywords: Hydrostatic motor, fluid structure interaction, leakage flow, experimental verification.

1. Introduction

The development and manufacturing of hydraulic motors is both time consuming and expensive due to its strong dependency on tolerances and prototype design. The manufacturing tolerances and surface roughness of the internal parts require special machining facilities and extra manufacturing steps. Also, assembly and testing must be carried out with tight tolerances on parameters such as bolt pretension, choice of fluid and fluid temperature. When developing new motors whether it is a new type of motor or simply scaling of an existing this is even more pronounced. The use of a model based approach to the design is complicated by the fact that two important design criteria; volumetric efficiency and hydromechanical efficiency are difficult to evaluate due to their strong relationship to tribology phenomena. Therefore, the modelling typically requires handling of friction, lubrication and complex structural deflections.

Fluid film lubrication and elastic surface deformations have been of high interest for several researchers and in different applications. In (Ivantysynova, et al., 2009), (Huang, et al., 2006), (Ivantysynova, et al., 2009) and (Wieczorek, et al., 2002) the lubricating gap of axial piston machines are investigated. The dynamic simulation models in these papers considers, among others, non-isothermal fluid flow, squeeze effect in the lubricating gap due to piston motion and effects due to deformation of parts caused by fluid pressure. The experimental validation is based on measured pressures and temperatures in the lubricating gap. In (Manring, et al., 2002) and (Karadere, 2010) the fluid film lubrication and elastic surface deformation of hydrostatic thrust bearings are investigated. The main focus in these two papers is the effects of deformed gap surfaces. Depending on the deformation modes, the load carrying capacity and power costs of a thrust bearing are influenced. In (Koç, 1990) the numerical solution of the Reynolds equation governing the fluid film of thrust bearings is of concern.

In this paper fluid-structural interaction modelling is used to evaluate a new motor design with emphasis on the external leakage (drain) paths across the end faces of the rotor. This includes an investigation of the effect of using compensation pressure volumes to manipulate the external leakage paths across the rotor faces.

The aim of the model development is a computational tool that can predict the effects and consequences of an up-scaling or modification of the motor principle, and, subsequently, minimizing the demands for prototyping.

The aim is to up-scale the motor to displacements in the range of 200…500 l/rev, for extraordinary low speed high torque applications. Hence, minimization of the leakage paths and the structural deflections are envisaged to be crucial in order to reach useful volumetric efficiencies.

2. Motor Principle

The hydraulic motor principle investigated in this paper is described in (Sørensen, et al., 2009) and (Sørensen, et al., 2011). It is categorized as an extreme low speed high torque motor. The volumetric efficiency is critical for slowly rotating motors. In the present motor principle it is especially the leakage flow into the drain that is affecting the volumetric efficiency. The drain is located in the centre and on both sides of the rotor. The oil is flowing into the drain across the end faces of the rotor from the high pressure chambers (see Fig. 1). The rotor is rotating because of pressure difference across the vanes. The stops and the rotor form six chambers that are further divided by either one or two vanes. However, it can be designed with any number of chambers as a trade off between specific displacement (displacement per motor volume) and complexity. The vanes are moved in radial direction when passing a stop. This radial movement of the vanes is actuated by hydraulic pressures which due to the inlet/outlet system are causing an axial force imbalance at the rotor.

The height of the gaps between the moving parts in hydraulic motors is crucial for the efficiency and the performance. These gaps both serve as sliding bearings and leakage paths. Hence, within the entire operational range of the motor these gaps should be capable of securing fluid film lubrication without causing excess leakage flow.

The hydraulic motor principle shown in Fig. 1 has several leakage paths along the vanes and the rotor, but only the lubricating gaps at the end faces of the rotor (between the rotor and the inner housings) are of concern in this paper. The pressure distribution in these lubricating gaps is creating a significant force at the housings because of the large area from the outer radius of the chambers to the drain connections located close to the centre of the rotor. This force is causing a deflection of the inner housings which must be minimized to maximize the volumetric efficiency of the motor. To counteract deflections of the lubricating gap of concern, the motor has compensation pressure volumes between the inner and outer housings (see location of compensation volumes in Fig. 1). All the compensation pressure volumes are enclosed by o-ring sealing, which are, among other details, not illustrated in Fig. 1.

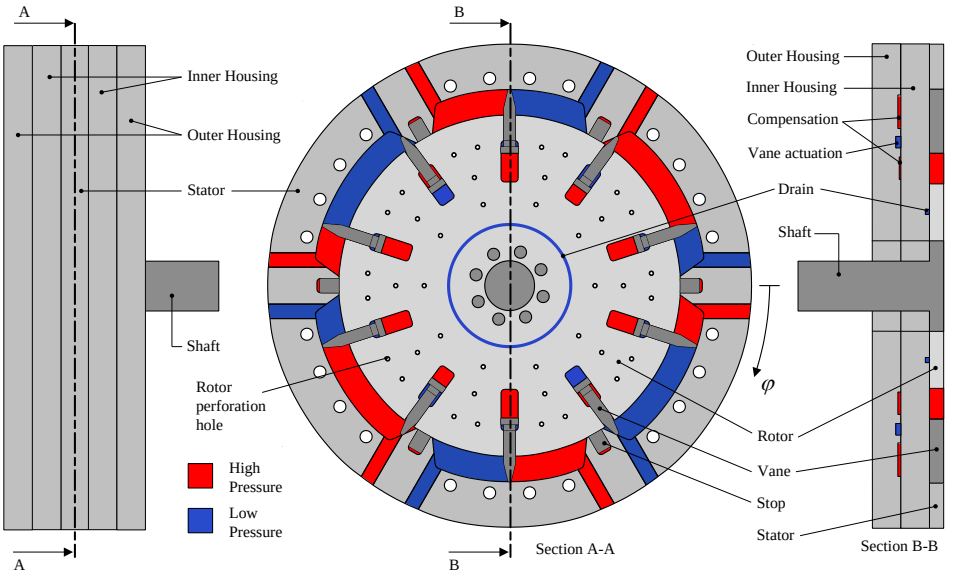

Figure 1. Side and end view of motor principle.

3. Fluid Structure Interaction Simulation Model

The fluid structure interaction is handled by using the partitioning approach as defined in (Felippa, et al., 2001). The fluid and the structural calculations are carried out separately. The discretization is the same for both the structural and the fluid calculations which is easing the interchange of state variables.

Pressure distribution in the gaps between rotor and housings

The pressure distribution in the lubricating gaps between the end faces of the rotor and the inner housings are given by the Reynolds equation for fluid film lubrication.

The general Reynolds equation is (Hamrock, et al., 2004)

$$\begin{aligned} 0 &= \frac{\partial}{\partial x}\left(-\frac{\rho\cdot h^3}{12\cdot\eta}\cdot\frac{\partial p}{\partial x}\right)+\frac{\partial}{\partial y}\left(-\frac{\rho\cdot h^3}{12\cdot\eta}\cdot\frac{\partial p}{\partial y}\right) \\ &+\frac{\partial}{\partial x}\left(\frac{\rho\cdot h\cdot\left(u_{\mathrm{m}}+u_{\mathrm{n}}\right)}{2}\right) \\ &+\frac{\partial}{\partial y}\left(\frac{\rho\cdot h\cdot\left(v_{\mathrm{m}}+v_{\mathrm{n}}\right)}{2}\right) \\ &+\rho\cdot\left(w_{\mathrm{m}}-w_{\mathrm{n}}\right)-\rho\cdot u_{\mathrm{m}}\cdot\frac{\partial h}{\partial x} \\ &-\rho\cdot v_{\mathrm{m}}\cdot\frac{\partial h}{\partial y}+h\cdot\frac{\partial\rho}{\partial t}, \end{aligned} \tag{1}$$

where subscript m denotes the surface of body m and subscript n denotes the surface of body n (see Fig. 2).

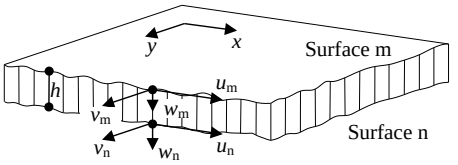

Figure 2. Illustration of the fluid film between surface m and surface n.

It is assumed that the rigid body motion of the rotor is rotational and axial and that the density and viscosity of the oil is constant. Furthermore, the Reynolds equation is expressed in polar coordinates, because of the geometry and rotational motion of the rotor. Therefore the pressure distribution in the gaps between the housing and the end faces of the rotor is, refer to (Beschorner, et al., 2009) and (Ivantysynova, et al., 2009),

$$\begin{aligned} &\frac{\partial}{\partial r}\left(r\cdot h^3\cdot\frac{\partial p}{\partial r}\right)+\frac{1}{r}\cdot\frac{\partial}{\partial\theta}\left(h^3\cdot\frac{\partial p}{\partial\theta}\right) \\ &=6\cdot\eta\cdot r\cdot\omega\cdot\frac{\partial h}{\partial\theta}+12\cdot\eta\cdot r\cdot\frac{\partial h}{\partial t} \end{aligned} \tag{2}$$

Equation (2) is solved numerically using the finite difference method for one rotor position. By dividing the area into elements (see Fig. 3) and approximating the derivatives in Eq. (2) by finite differences, $p_{\mathrm{i,j}}$ is expressed by its surrounding pressures and can be determined by looping through the mesh until the pressure variation from previous iteration ($p_{\mathrm{i,j}}^{\mathrm{cur}} - p_{\mathrm{i,j}}^{\mathrm{prev}}$) is smaller than a convergence tolerance.

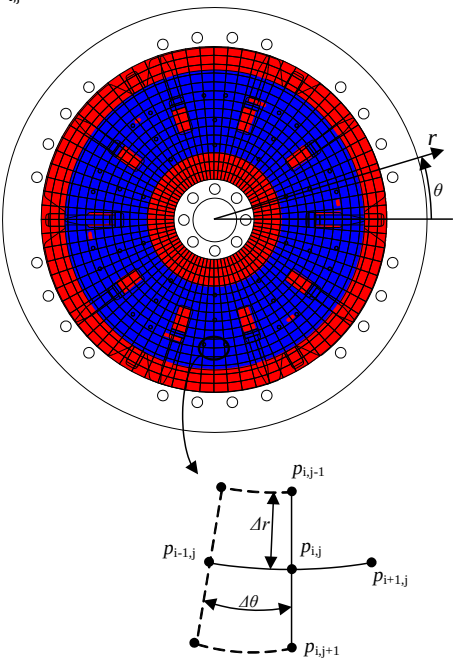

Figure 3. Finite difference mesh and boundary conditions. The colour red indicates that the pressure of the node is prescribed whereas blue indicates that the pressure is to be determined in the finite difference analysis.

The rotor is perforated to balance the pressure at each side of the rotor. Therefore a finite difference relaxation is carried out in parallel for both sides of the rotor. For the nodes placed within the area of perforation holes, the pressure is therefore affected by the pressure at the opposite side of the rotor. After solving Eq. (2) for $p_{\mathrm{i,j}}$ at both side of the rotor, the nodes are stated as the mean pressure of the two sides, as

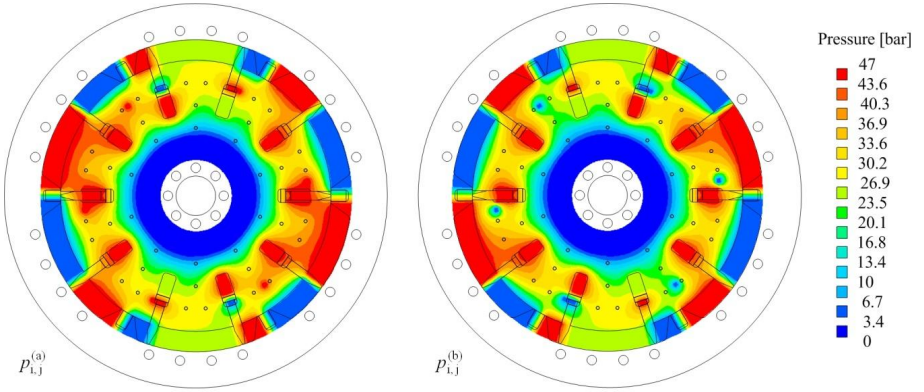

Figure 4. The pressure distribution in the lubricating gaps for one rotor position. The gaps are mirrored to each other. $\boldsymbol{p}_{\mathbf{i,j}}^{(\mathbf{a})}$ *is the gap pressure with high pressure connected to the vane actuations and* $\boldsymbol{p}_{\mathbf{i,j}}^{(\mathbf{b})}$ *with tank pressure to the vane actuations. The boundary conditions for this pressure distribution is* p_1*=47bar in the high pressure side of the vanes,* p_2*=6bar in the low pressure side of the vanes and* p_t*=1bar in the drain connection.*

$$p_{i,j}^{(a)} = p_{i,j}^{(a)} - 0.5 \cdot \left(p_{i,j}^{(a)} - p_{i,j}^{(b)} \right) \quad (3)$$

$$p_{i,j}^{(b)} = p_{i,j}^{(b)} - 0.5 \cdot \left(p_{i,j}^{(b)} - p_{i,j}^{(a)} \right), \quad (4)$$

where superscript (a) denotes one end face of the rotor and superscript (b) denotes the other end face of the rotor.

The boundary conditions to this finite difference method are the fixed pressures in the volumes. It is assumed that the pressure decreases linearly across both stops and vanes.

The pressure distribution in the fluid films across the end faces of the rotor for one motor pressure state is illustrated in Fig. 4.

The Structural deflections

The objective of the FEM models is to determine the structural deflections of the inner housing and the end face of the rotor which is forming the lubricating gaps of concern (see Fig. 5). The input to the FEM simulations is the pressure distribution in the fluid film and in the compensation volumes and the output is the deflection of the end faces, i.e., the variation of the gap.

The pressure in the compensation volumes is applied as pressures in the FEM simulation, whereas the pressure in the lubricating gap is added as nodal forces. The pressures from the fluid calculations is recalculated as nodal forces by

$$F_{i,j} = p_{i,j} \cdot r_{i,j} \cdot \Delta r \cdot \Delta \theta \quad (5)$$

The total height of the lubricating gap h is influenced by the deflection of the inner housing δ_{housing}, the rotor δ_{rotor} and the initial gap height h_{ini}, given by (see Fig. 5)

$$\Delta h_{i,j} = \delta_{i,j,\text{rotor}} + \delta_{i,j,\text{housing}} \quad (6)$$

$$h_{i,j} = h_{\text{ini}} + \Delta h_{i,j} \quad (7)$$

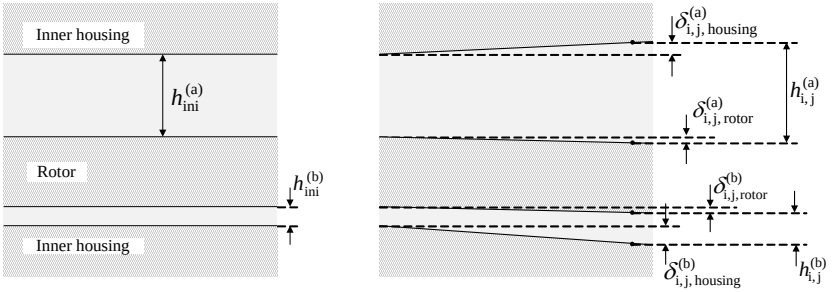

Figure 5. Illustration of initial gap and deformed gap.

Different FEM models have been used in the simulations. In Model I both inner housings and the rotor are individual FEM models, see Fig. 6. The output of the FEM analysis is used in the overall fluid-structure analysis. The deflections are used to compute $\Delta h_{i,j}^{(a)}$ and $\Delta h_{i,j}^{(b)}$. The resultant axial force on the rotor introduces an axial rotor velocity, $\delta h/\delta t$ (Eq. (2)). Simulations have shown that changing the rotor to a rigid body in this analysis reduces computational costs and has negligible effect on both pressure distribution and leakage flow across the end faces. The model with rigid rotor is referred to as Model II and has been preferred over Model I because of the reduced computational costs.

As described in the next section on the fluid-structure interaction the rotor position is updated from the $\delta h/\delta t$ term, and, eventually, reaches the inner housing. The rotor is forced against an inner housing due to asymmetry in the vane actuation commutation. As the rotor approaches the inner housing the lubrication film height will become zero (or negative) in certain regions corresponding to structural contact. Because of this Model II (and Model I) can only be used to describe the gap conditions in a satisfactory way up until mechanical contact is observed. In practice, the fluid film remains, however, its behavior in the areas with small or no gap is that of mixed lubrication and should be described by means of more complex models that also include surface details.

When mechanical contact is observed a third model, Model III, is employed where a flexible rotor is connected to the inner housing via contact elements, see Figure 6. Because of the mixed lubrication conditions, the tangential friction coefficient between the rotor and inner housing is set to μ=0.15, according to the one used for oil lubricated threat-nut combination in (Norton, 2000). The mixture of pressure and contact forces between the rotor and the inner housing is now represented by the normal reactive forces of the contact elements.

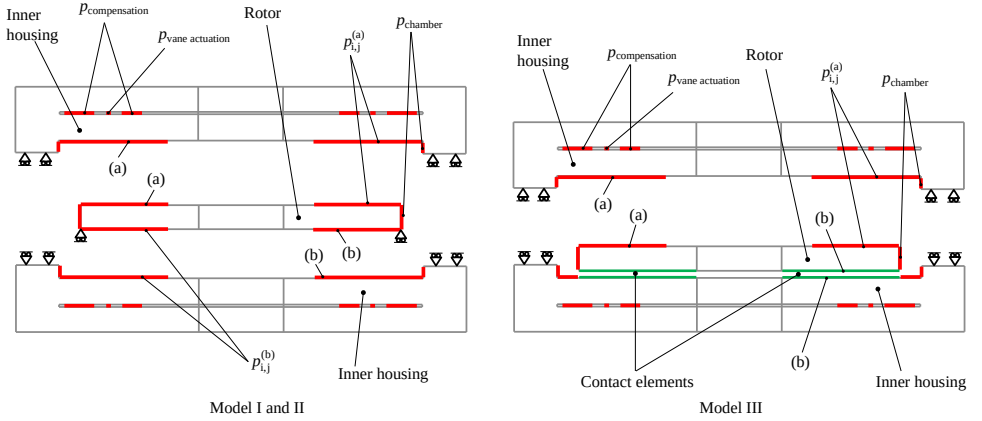

Figure 6.The principles behind Model I and II are shown to the left and the principles behind Model III are shown to the right.

The different FEM models in Fig. 6 have a number of boundary conditions in common: There are no displacements in the normal direction to the section cut of the stator. The compensation pressure volumes are included between the inner and outer housing. The applied compensation pressures are symbolized by bold red lines between inner and outer housing. The bold red lines at the gap of interest are where all the individual forces in the fluid are applied based on Eq. (5). They are located between the rotor and the inner housing and are reaching from the outer radius of the chambers into the drain connection. The vertical bold red lines symbolize the average chamber pressure on the stator in radial direction.

All the FEM models are meshed by three dimensional 8 node hexahedral elements. The applied mesh for the determination of $\delta^{(a)}_{i,j,housing}$ is shown in Fig. 7.

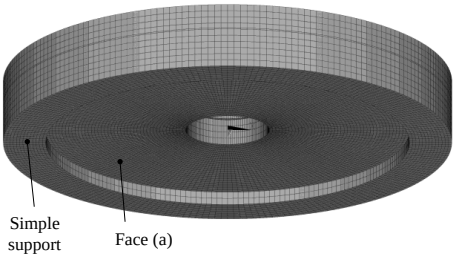

Figure 7. The applied mesh for the determination of $\boldsymbol{\delta^{(a)}_{i,j,housing}}$*. The FEM mesh consists of three dimensional 8 nodes hexahedral elements.*

The Interaction between the Fluid and the Structural simulations:

The pressure distribution in the lubricating gap is influenced by the gap height and the gap height is influenced by the pressure distribution. To be able to convert node forces from the fluid- to the structural calculations and to convert node deflections from the structural- to the fluid calculations, the node numbering and coordinates are equal.

The simulation model is handling the lubricating gap between the rotor and the inner housing at both side of the rotor. The two sides are analyzed simultaneously to be able to determine the axial position of the rotor and include the effect of the pressure equalizing perforation holes.
The simulation model is illustrated by a flow chart in Fig. 8. Initially all the constants, initial values and boundary conditions are specified. Next step is the initialization of the most outer loop of the simulation model, which is the time loop that updates the part of the gaps that are not influenced by the deflections, $h^{(a)}_{ini}$ and $h^{(b)}_{ini}$. The time dependent term, $\partial h/\partial t$ of Eq. (2), is solved for via a Newton Raphson iteration loop, see Fig. 8. Hence, the axial rigid body velocity of the rotor relative to the inner housings is computed in each time step and is used to update the gap heights as

$$h^{cur}_{ini} = h^{prev}_{ini} + \frac{\partial h}{\partial t} \cdot \Delta t \qquad (8)$$

where Δt is the step size of the time integration. Initially, the rotor is in the centre between the inner housings, $h^{(a)}_{ini} = h^{(b)}_{ini}$.

The first step in the fluid structure interaction (FSI) loop of the program is to recalculate the node pressures into node forces using Eq. (5). This is carried out in the main Matlab program and the node forces are written to a separate text file in the FEM solver (ANSYS in this study) node force syntax. This text file is the force input to the structural FEM solver analysis. The output from the FEM solver analysis is the node deflection for the nodes that are forming the lubricating gap. These node deflections are again communicated to the main Matlab program in a text file and added to the initial gap heights to express the total gap height for each node location. After the determination of the gap height in the individual nodes, the fluid calculations are performed. For every node Eq. (2) is solved by the finite difference method by looping through the entire mesh. This procedure is continued until the convergence statement is fulfilled.

The last part of the FSI loop is to evaluate the FSI convergence statement. This convergence statement is based on the total change of pressure, compared to the previous FSI iteration with the previous gap heights. When this total change of pressure is sufficiently small, the gap heights and pressures have converged.

The last step in the simulation model is to determine the theoretical external leakage flow based at the determined pressures and gap heights. The leakage flow pr. node is

$$Q_{i,j} = -\frac{1}{12 \cdot \eta} \cdot h^3_{i,j} \cdot \frac{\partial p_{i,j}}{\partial r} \cdot r \cdot \Delta\theta \qquad (9)$$

The force imbalance at the rotor in axial direction is balanced by the pressure in the lubricating gaps. In (Ivantysynova, et al., 2009) force balance for external forces and fluid film pressure is used to determine the gap height of the fluid film between the cylinder block and valve plate in an axial piston machine. Similarly, in (Isaksson, et al., 2009) the fluid film gap height is modified to balance external forces and fluid film pressure in a radial piston machine.

In the simulation model the axial forces at the rotor is balanced by the squeeze effect in the fluid film until the rotor comes to rest or approaches an inner housing to an extent where the gap height becomes zero (or negative) in certain regions. Then the force balance is obtained by modifying the axial velocity of the rotor ($\partial h/\partial t$ in Eq. (2)). The equations are solved for $\partial h/\partial t$ using the Newton Raphson solver.

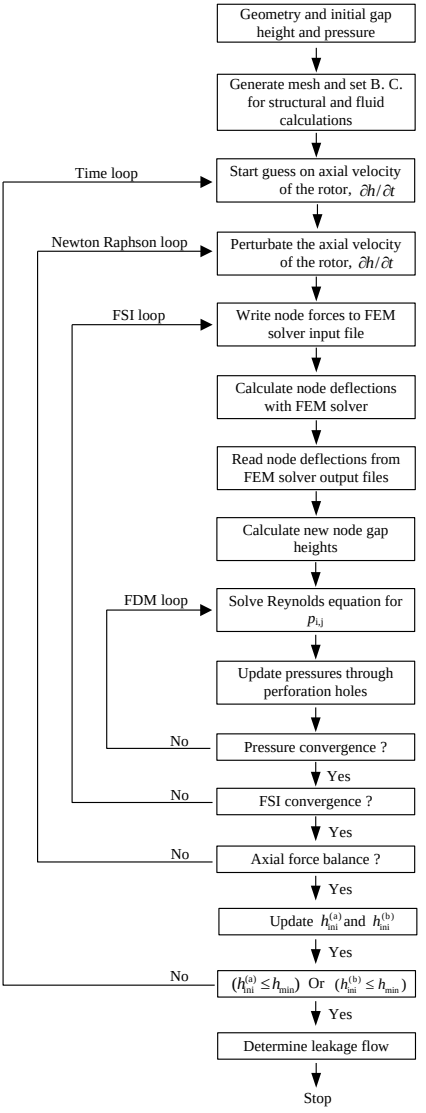

Figure 8. The flow chart of the simulation model.

The input to the simulation model is measured pressures. The boundary conditions for the simulation model are the pressure state in the high and low pressure volumes around the vanes, which are those governing the pressure distribution in the gap, and the pressure in the compensation volumes. The pressure difference across the vanes depends on the loading of the motor output shaft.

A trend of the simulation model is that the rotor is forced against one of the inner housings and maintains this position steady state. Then the lubricating gap height at the one side of the rotor is maximized and at the other side there is no lubricating gap, but instead mixed film lubrication.

4. Experimental Verification by Prototype Tests

The simulation model is verified by comparing simulated results and measured results. The measured results are generated by doing measurements on a prototype motor.

The data for the prototype motor and the motor conditions during the tests are listed in table 1.

Outer motor diameter	d=340mm
Outer motor height	l=100mm
Height of rotor	s=20mm
Number of chambers	n_{ch}=6
Number of vanes	n_{vane}=10
Maximum working pressure during tests	p_1=57bar
Prototype displacement	D=1.75 l/rev
Maximum rotational speed during tests	ω=5 rev/min
Maximum output torque during tests	T=1000 Nm
Input flow during tests	Q_1=10 l/min

Table 1. The specifications of the prototype motor and the operating conditions during the tests.

The structural deflections are measured with a moving coil actuator (MCA) that is fitted with a 0.1µm encoder. The body of the MCA is mounted on the inner housing of the prototype motor as illustrated in Fig. 9. The MCA is controlled in force mode and maintains a force of 1.7N during the test. Then the piston of the MCA is always touching the rotor during tests. The build-in encoder of the MCA is measuring the position of the piston and therefore the relative distance, or deflections, between the housing and the rotor. The measurements are performed when the rotor rotates and therefore the MCA tip is sliding across the face of the rotor. Hence, the output from the MCA is gap heights at a circle of points.

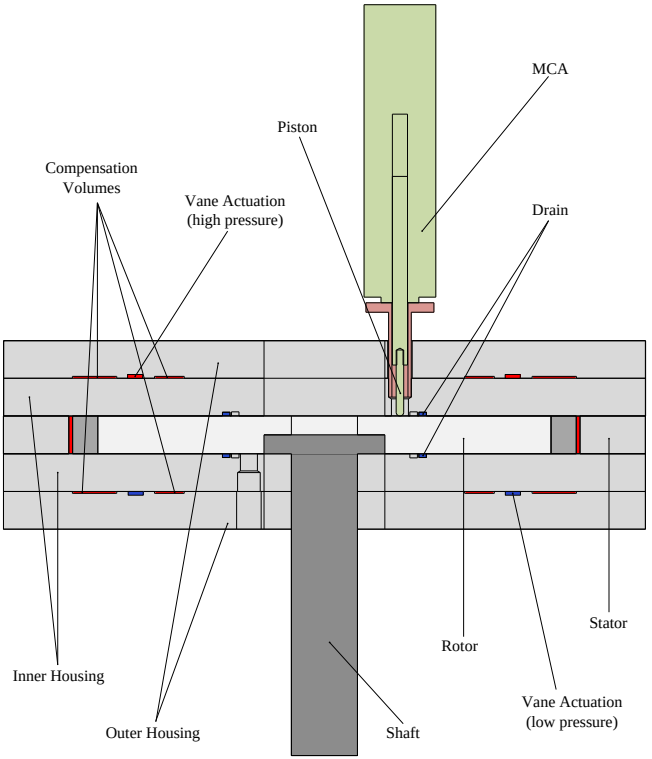

Figure 9. The prototype motor in a section cut with compensation volumes and the moving coil actuator mounted.

Furthermore, the location of the compensation volumes and the vane actuation connections are shown in the cut through view on Fig. 9.

Apart from the MCA the test setup is equipped with flow and pressure transducers. A part of the hydraulic diagram of the test setup is shown in Fig. 10. The oil flow into and out of the motor is measured. The two drain connections are each fitted with a flow transducer to be able to measure the drain flows individually. These two flow transducers are a second option to validate the theoretical simulations because of the relation between the structural deflections and the drain flow. The pressure transducers are measuring the pressure state in the motor during the tests. The measured pressures are the boundary conditions for the theoretical simulations.

The test setup is equipped with a pressure reducing valve to reduce the pressure in the compensation volumes. The pressure reducing valve is adjustable, but the reduction pressure is kept constant at p_{comp}=35bar during all the tests. Then the effect of the compensation volumes can be validated by comparing deflections when p_1< 35bar, i.e. $p_{comp}=p_1$, and when p_1>35bar, i.e. $p_{comp}<p_1$.

The prototype motor is loaded by a powder brake, through a gearbox, in the test setup. The resistance torque of the powder brake is electronically adjustable. The torque performance of the prototype motor is measured by strain gauges on the output axle. The angular position and velocity of the motor are measured with an optical encoder mounted on the test setup.

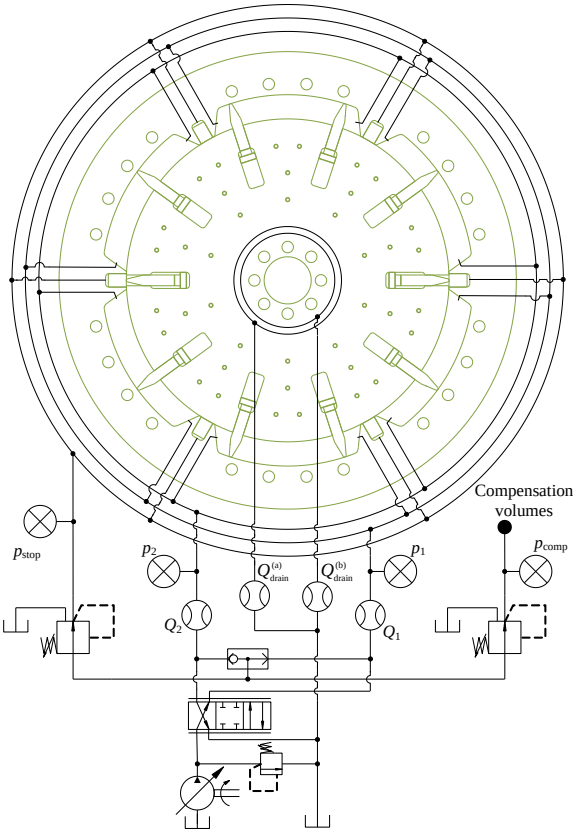

Figure 10. A part of the hydraulic diagram of the test setup with pressure and flow transducers and two pressure reducing valves.

The prototype motor is shown in Fig. 11 in both the test setup and when partly disassembled.

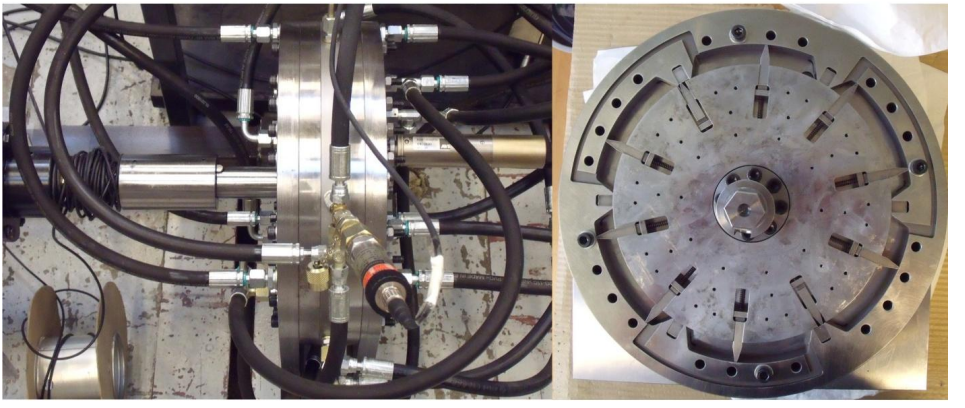

Figure 11. The prototype motor in the test setup and when partly assembled.

5. Comparison of Simulated Results and Experimental Results

The experimental results are based on measurements during a considered steady state run. As concluded by the end of section 4, the rotor of the prototype is forced against one of the inner housing, which is the case until the rotational direction of the motor is changed. Therefore rigid body motion of the rotor in axial direction is not handled in the experimental measurements or the result comparison.

The loading of the motor and the input flow are kept constant during a test run and the mean values are extracted from the measurement devices. This procedure is continued to generate all the test data, by only changing the resistance torque of the powder brake. By changing the resistance torque the high pressure, and hence deflections and drain flow, become different for the individual test sequences. The input flow to the motor is kept constant during all the measurements.

The measured deflections and drain flows are extracted to a representative time point for all the different load cases. The simulated results are based at one fixed rotor angle, which approximately represents the mean theoretical drain flow. This rotor angle is the one used in Fig. 3, 4 and 10.

In Fig. 12 to the left both the simulated and measured deflection of the gap are plotted with respect to the high pressure p_1. There is no rigid body motion included on the graph. Both the measured and simulated curves in Fig. 12 have a bend at 35bar, which is the pressure limit for the compensation pressure p_{comp} as controlled by the pressure reducing valve. The reason for reducing the compensation pressure is to be able to investigate the effect on the deflection. The vertical axis is gap deflection as described by Eq. (6). The simulated deflections are showing a good correlation with the measured deflections.

The simulated deflections do not completely follow one path because of variations in the measured p_{comp} and p_2 to the same measured p_1. These pressures are input to the simulation model, which then is causing variations in the simulated Δh to the same p_1.

The deflection curves are not intersecting in Δh=0. The reason is the significant measured p_2 pressures which are above tank pressure.

The measured and simulated drain flows $Q_{\text{drain}}^{(a)}$ with respect to h are shown in Fig. 12 to the right. All the point marks are measured and simulated flows during a considered steady state test sequence. In all the measurements the corresponding drain flow $Q_{\text{drain}}^{(b)}$ and gap height $h^{(b)}$ are zero, due to the axial force imbalance on the rotor.

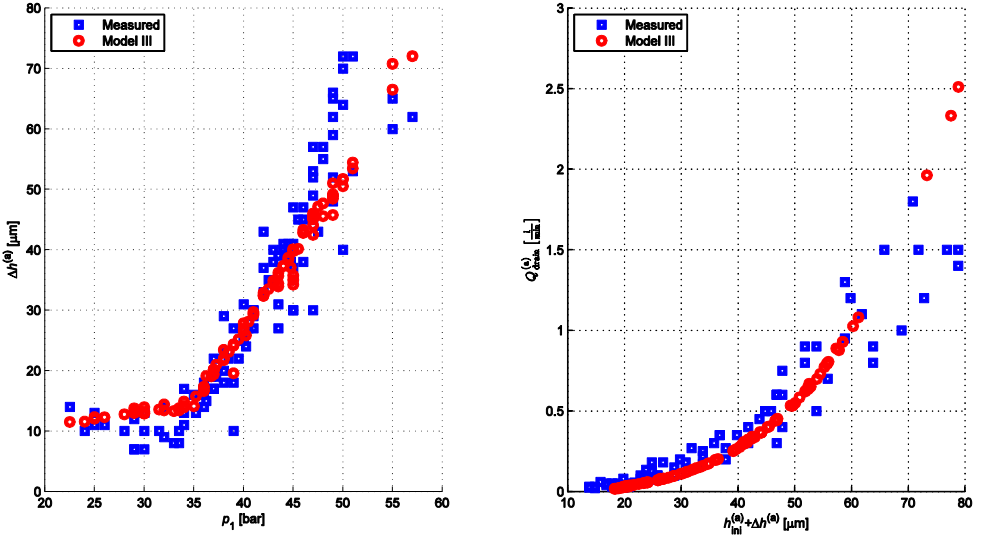

Figure 12. To the left is measured and simulated deflection with respect to the measured high pressures and to the right is leakage flow with respect to the total gap height.

6. The Effect of Axial Balancing of the Rotor

To quantify the effect of the compensation volumes onto the external leakage flow, the individual external leakage flows are determined by the simulation model (see Fig. 13). The upper graph is showing the external leakage flow of the motor with no compensation pressures. It is plotted with respect to p_1. The second graph is the drain flow for the motor with compensation pressures. The compensation pressure is not restricted by a pressure reducing valve, which means that $p_{comp}=p_1$ to every load situations in Fig. 13. The effect of the compensation pressures on Q_{drain} is remarkable. This trend has also been demonstrated experimentally, but the measurements are not useful for a comparison. The prototype gets unsteady or unable to rotate without the use of the compensation pressures, because of too much volumetric loss.

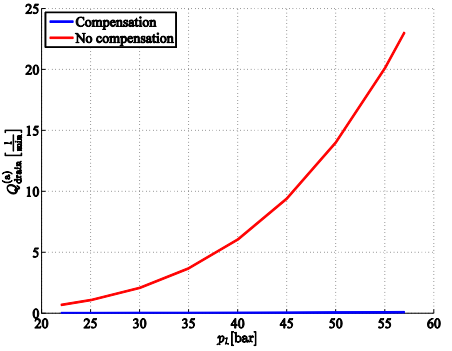

Figure 13. The effect of the compensation pressure volumes on the drain flow. The graphs are showing the drain flow with and without compensation pressures.

7. Conclusions

The lubricating gap height and leakage flow are determined by employing different fluid structure interaction simulation models. The basic simulation model (Model I) determines the pressure distribution in the lubricating gaps between the rotor and the inner housing by solving Reynolds equation and determines the structural deflections of the surfaces that form the gap by FEM simulations. Furthermore, the Model I computes the axial velocity of the rotor that generates force equilibrium due to the squeeze effect. A somewhat simpler model (Model II) neglects the flexibility of the rotor. Both models converge towards a situation where the rotor comes in structural contact with the inner housing leading to a third model (Model III) where the mixed lubrication regime between rotor and inner housing are modelled as a frictional contact model. This model seems to be in good accordance with the experimental data, especially regarding the measured structural deflections. This validates the simulation model which is targeted to serve as a design tool when up-scaling the motor.

The combined numerical and experimental investigation carried out on a prototype of the new motor principle reveals that the leakage gaps caused by elastic deformations can be prevented by the use of pressure compensation volumes. The elastic deformations of the hydrostatic motor principle put forward in this paper can be kept at an acceptable level by the use of compensation volumes. They both save material costs and improve the compactness of the motor. This is especially significant for larger motors.

Nomenclature

d	Diameter	m
D	Displacement	m^3/rev
F	Force	N
h	Gap height	m
l	Outer motor height	m
n_{ch}	Number of chambers	
n_{vane}	Number of vanes	
p	Pressure	Pa
Q	Flow	m^3/s
r	Radius, radial coordinate	m
s	Height of rotor	m
T	Torque	N·m
t	Time	s
u	Velocity along x axis	m/s
v	Velocity along y axis	m/s
w	Velocity along z axis	m/s
x	Cartesian coordinate	m
y	Cartesian coordinate	m
δ	Structural deflection	m
Δh	Total gap deflection	m
Δp	Pressure difference	Pa
Δr	Radial element division	m
Δt	Time step	s
$\Delta\theta$	Tangential element division	rad
η	Dynamic viscosity	Pa·s
θ	Angular coordinate	rad
μ	Coefficient of friction	
ρ	Density	kg/m^3
φ	Angular position	rad
ω	Angular velocity	rad/s

References

Beschorner, K., Higgs III, C. F. and Lovell, M. 2009. Solution of Reynolds Equation in Polar Coordinates Applicable to Nonsymmetric Entrainment Velocities. *Journal of Tribology.* Volume 131, 2009.

Felippa, C. A., Park, K. C. and Farhat, C. 2001. Partitioned analysis of coupled mechanical systems. *Computer Methods in Applied Mechanics and Engineering.* Volume 190, 2001.

Hamrock, B. J., Schmid, S. R. and Jacobsen, B. O. 2004. *Fundamentals of Fluid Film Lubrication.* 2. Edition. s.l. : Marcel Dekker Inc, 2004.

Huang, C. and Ivantysynova, M. 2006. An Advanced Gap Flow Model Considering Piston Micro Motion and Elastohydrodynamic Effect. *Proc. of the 4th FPNI PhD Symposium, Sarasota.* 2006.

Isaksson, P., Nilsson, D. and Larsson, R. 2009. Elasto-hydrodynamic simulation of complex geometries in hydraulic motors. *Tribology International 42.* 2009.

Ivantysynova, M. and Baker, J. 2009. Power loss in the lubricating gap between cylinder block and valve plate of swash plate type axial piston machines. *International Journal of Fluid Power.* No. 2, 2009.

Ivantysynova, M. and Pelosi, M. 2009. A novel fluid-structure interaction model for lubricating gaps of piston machines. *Fluid Structure Interaction V.* 2009.

Karadere, G. 2010. The effects of the total bearing deformation on the performance of hydrodynamic thrust bearings. *Industrial Lubrication and Tribology.* Volume 62, 2010.

Koç, E. 1990. An investigation into the numerical solution of Reynolds' lubrication equation with special reference to thrust bearings. *Tribology International.* Vol 23, 1990.

Manring, N. D., Johnson, R. E. and Cherukuri, H. P. 2002. The Impact of Linear Deformations on Stationary Hydrostatic Thrust Bearings. *Journal of Tribology.* Vol 124, 2002.

Norton, R. L. 2000. *MACHINE DESIGN An Integrated Design.* s.l. : Prentice Hall, 2000.

Sørensen, R. M., et al. 2011. Hydraulic Yaw System for Wind Turbines with New Compact Hydraulic Motor Principle. *Proc. of the European Wind Energy Association Conference, Bruxelles.* 2011.

Sørensen, R. M., et al. 2009. Investigation of Hydraulic Motor Principle for Low Speed High Torque Applications. *Proc. of the 22th. Nordic Seminar on Computational Mechanics, Aalborg.* 2009.

Wieczorek, U. and Ivantysynova, M. 2002. Computer Aided Optimization og Bearing and Sealing Gaps in Hydrostatic Machines - The Simulation Tool CASPER. *International Journal of Fluid Power.* 2002, 1.

Paper B

Numerical and Experimental Study of Friction Loss in Hydrostatic Motor
Rasmus M. Sørensen, Michael R. Hansen, Ole Ø. Mouritsen
Published in *Modeling, Identification and Control*, Vol 33, No. 3, 2012, pp. 99-109, ISSN 1890-1328

Modeling, Identification and Control, Vol. 33, No. 3, 2012, pp. 99–109, ISSN 1890–1328

Numerical and Experimental Study of Friction Loss in Hydrostatic Motor

Rasmus M. Sørensen [1] Michael R. Hansen [2] Ole Ø. Mouritsen [3]

[1] *Liftra Aps & Department of Mechanical and Manufacturing Engineering, Aalborg University, DK-9220 Aalborg East, Denmark. E-mail: rms@liftra.dk*

[2] *Department of Engineering, University of Agder, N-4876 Grimstad, Norway. E-mail: michael.r.hansen@uia.no*

[3] *Department of Mechanical and Manufacturing Engineering, Aalborg University, DK-9220 Aalborg East, Denmark. E-mail: oom@aau.dk*

Abstract

This paper presents a numerical and experimental study of the losses in a hydrostatic motor principle. The motor is designed so that the structural deflections and lubricating regimes between moving surfaces and, subsequently, the leakage and friction losses, can be controlled during operation. This is done by means of additional pressure volumes that influence the stator deflection. These pressures are referred to as compensation pressures and the main emphasis is on friction or torque loss modeling of the motor as a function of the compensation pressures and the high and low pressures related to the load torque. The torque loss modeling is identified as a Stribeck curve which depends on gap height. The asperity friction is decreasing exponentially with an increase in gap height. The parameters of the torque loss model are based on prototype measurements that include the structural deflections of the lubricating gap faces.

Keywords: Hydrostatic motor, friction loss, mixed lubrication, experimental verification

1 Introduction

The performance of hydrostatic displacement machines is strongly related to their efficiencies. The design and manufacturing tolerances are a trade-off between volumetric and hydromechanical loss. The general trend is that if the volumetric loss goes down the hydromechanical loss goes up, and vice versa, because of their opposite nature. Except for the division into volumetric and hydromechanical losses there exist no unified modeling techniques that describe the losses in hydrostatic machines in detail (Ivantysyn and Ivantysynova, 2003). Especially, the hydromechanical loss is difficult to model in a simple way since it depends on a wide variety of friction losses. They include laminar and turbulent flow induced pressure drops in the displaced fluid as well as a combination of friction caused by boundary layer, mixed layer and elastohydrodynamic lubrication between moving parts. These phenomena depend on the operating conditions as well as the topology and geometry of the hydrostatic machine.

In general, the complex behavior prevents model based prediction of the performance and therefore design of hydrostatic machines rely heavily on fine machining tolerances and excessive testing of volumetric and hydromechanical losses for the entire operating range, see (Ivantysyn and Ivantysynova, 2003), (Ivantysynova, 2003) and (Murrenhoff et al., 2008).

In this work the hydromechanical efficiency is examined for a new motor concept. The concept has been presented in earlier work (Sørensen et al., 2011). The most important characteristics of the motor principle are a high specific displacement (displacement per motor volume), a minimum of manufacturing tolerance

doi:10.4173/mic.2012.3.2

dependencies and the ability to adjust structural deflections of leakage gaps by applying so-called compensation pressures via designated pressure pockets.

Work has already been done on the leakage characteristics of the motor principle with regard to compensation pressure (Sørensen et al., 2012). In (Sørensen et al., 2012) the conclusion is that the volumetric efficiency of the motor principle is highly influenced by the gap flow across the large end faces of the rotor and the housing, and that an increase in these gap heights can be prevented by the use of compensation pressures. In fact, both theoretical and experimental studies clearly revealed that any succesful application of the motor depends on the use of the compensation pressure to reduce leakage flow. Obviously, this compensation must be applied carefully to avoid excessive friction losses.

Therefore, this paper is on the investigation of the torque losses of the motor principle. The main contributions are:

- The set up of an experimentally verified model to describe the surface gap between the rotor and the inner housing
- The set up of an experimentally verified model to describe the torque loss between the rotor and the inner housing
- The development of an understanding of the interaction between the rotor and the inner housing.

2 Motor Principle

The hydraulic motor principle investigated in this paper is shown in figure 1. The stops and the rotor form six chambers that are further divided by one or two vanes. However, it can be designed with different number of chambers and vanes as a trade off between specific displacement and complexity. The rotor is subjected to a torque because of pressure difference across the vanes. The vanes are moved in radial direction when passing a stop. This radial movement of the vanes is facilitated by means of alternating high and low hydraulic pressures in pockets in the housing. These pressures are referred to as vane actuation pressures (p_v) and they are reversed together with the rotational direction of the rotor. In figure 1 vane actuation pressures corresponding to a clockwise rotation are shown. The vane actuation pressures are symmetrical on both side of the rotor to avoid an axial force imbalance on the rotor. When not passing a stop the vanes are forced against the stator which seals with the vane tip. To avoid high demands on tolerances on the dominant radial dimension the stops are designed as small pistons that are forced against the rotor by a pressure.

The two large areas between the rotor and the inner housing (the face on the middle view of figure 1) strongly influence the efficiency of the motor. These areas have, as all the gaps between moving parts, double

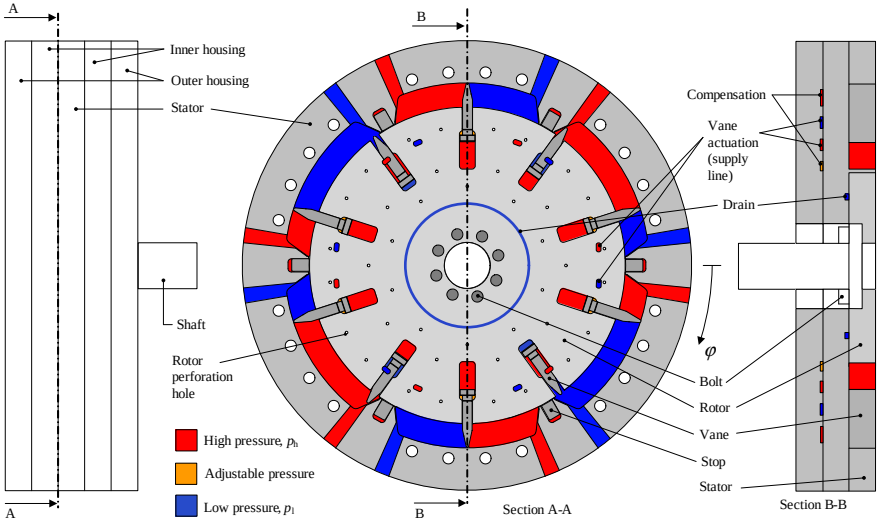

Figure 1: The motor principle.

contradicting functionality, namely sealing and lubrication. If the performance criteria of either of these functionalities are not given proper attention the motor will not be useful for practical applications. The main challenge is to maintain the performance with respect to both performance criteria over a wider range of operating conditions. The pressure distribution in these gaps is creating a significant force at the inner housings because of the large area from the outer radius of the chambers to the drain connections located close to the centre of the rotor. These forces are causing a deflection of the inner housings which must be minimized to maximize the volumetric efficiency of the motor. To counteract these deflections, the motor has compensation pressure volumes between the inner and outer housings (see location and geometry in figure 1, 2 and 3).

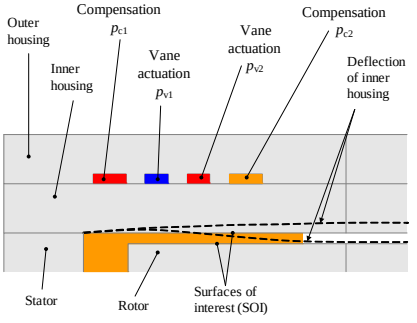

Figure 2: A section view of the motor principle with potential deflections of an inner housing illustrated by the dotted lines.

Besides the pressure distribution in the gap and the compensation pressures, the pressures in the supply lines to the vane actuation also influence the deflections of the inner housings. Therefore the deflection of the inner housings can potentially be in two directions as illustrated by the dotted lines in figure 2. The deflection behavior depends on the area and pressure magnitude of the individual volumes illustrated in figure 2. The layout of the vane actuation supply lines and compensation pressure volumes is restricted by the available space outside the sealings and oil channels. The layout of these volumes is illustrated in figure 3 without oil inlet channels. The volumes are sealed by o-rings.

The surfaces of interest (SOI) in this paper are shown in figure 2 with potential gaps illustrated by the dotted lines. The pressures in the vane actuation supply lines follow the low and high pressure levels of the motor.

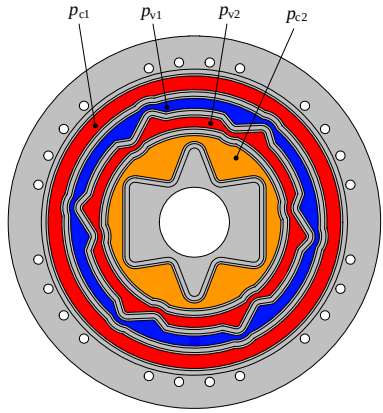

Figure 3: The geometry of the compensation and vane actuation supply pressure volumes, which are between the inner and outer housing.

One is connected to the low pressure part and the other to the high pressure part, depending on the rotational direction.

The velocity of the motor and the oil viscosity are held constant in this work, because the torque loss due to these phenomena are not remarkably different as compared to existing hydrostatic motor principles. The remaining friction losses that are singled out for attention are:

- the friction force of the boundary lubrication between stops and rotor
- the friction force of the boundary lubrication between vanes and stator
- the friction force of the boundary, mixed or elasto-hydrodynamic lubrication (EHL) between the end faces of the rotor and the inner housings

3 Experimental Work

The aim of the experimental work is to investigate the torque loss and the influence of the compensation pressures on the torque loss. In the experiments p_{c1} is equal to the high pressure, p_h, of the prototype and p_{c2} is adjusted to different pressure levels to examine the changing lubrication regime between the SOI.

3.1 Experimental Test Setup

To be able to determine the torque losses of the prototype motor the test setup has pressure transducers to

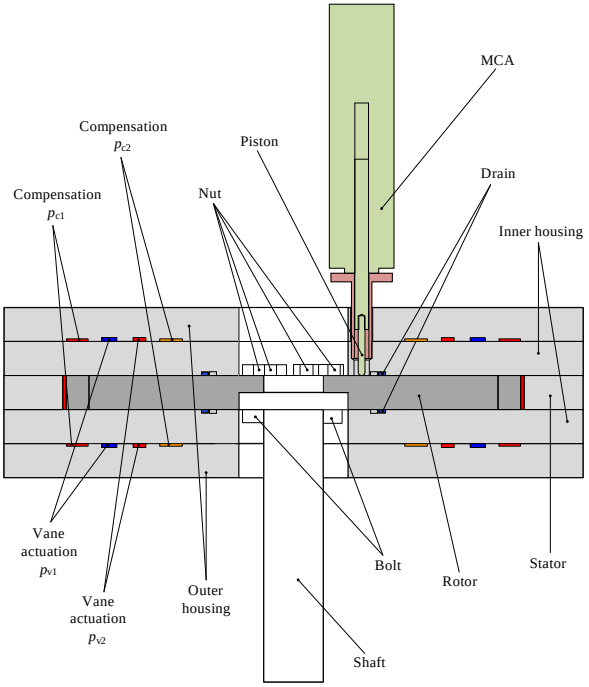

Figure 4: Section cut of the prototype motor. The moving coil actuator (MCA) is mounted on the inner housing and the piston is forced against the end face of the rotor during tests.

measure p_h and p_l, see figure 1, yielding the pressure difference, $\Delta p = p_h - p_l$, and a strain gauge transducer to give the output torque T_{out}. Further the test setup has flow transducers, a temperature transducer and an absolute encoder for motor velocity. The prototype motor is loaded by a powder brake, through a gearbox.

The structural deflections of the inner housing are measured with a moving coil actuator (MCA). The MCA is fitted with a $0.1\mu m$ encoder to measure the position of the MCA piston. The body is mounted on the inner housing of the prototype motor as illustrated in figure 4. The MCA is controlled in force mode and maintains a force of $1.7N$ during the tests so that the piston always is in contact with the rotor. The built-in encoder of the MCA measures the position of the piston and therefore the relative distance between the inner housing and the rotor. The measurements are performed when the rotor rotates and therefore the MCA tip is sliding across the face of the rotor. The extracted gap heights are mean values during one motor revolution to minimize deviations due to e.g. surface roughness and variations in the thickness of the rotor.

The adjusted compensation pressure p_{c2} is restricted by a pressure reducing valve. During the tests, the pressure level is adjusted to $p_{c2} = 10, 16, 22, 27bar$.

The data for the prototype motor and the motor conditions during the experimental tests, are listed in table 1.

3.2 Experimental Results

The total torque loss of the prototype motor is

$$T_{loss} = T_{th} - T_{out} = \frac{(p_h - p_l) \cdot D}{2 \cdot \pi} - T_{out}, \quad (1)$$

where D is the displacement. The measured T_{loss} and the measured deflections of the inner housing h_{MCA} are shown in figure 5. The trend in the measurement is clear. T_{loss} is decreasing with the increase in p_h until reaching a minimum $T_{loss,min}$, whereafter T_{loss} is increasing almost linearly with p_h. $T_{loss,min}$ is changing for the different p_{c2} values and for $p_{c2} = 27bar$ the minimum is not inside the pressure range of the tests. The hypothesis put forward here is that before $T_{loss,min}$

Table 1: The prototype specifications and the operating conditions during the tests.

Outer motor diameter	$d = 340mm$
Outer motor height	$l = 100mm$
Height of rotor	$s = 20mm$
Number of chambers	$n_{ch} = 6$
Number of vanes	$n_{vane} = 10$
Prototype displacement	$D = 1.75l/rev$
Maximum pressure during tests	$p_h = 51bar$
Compensation pressure p_{c2}	$p_{c2} = 10, 16, 22, 27bar$
Rotational speed during tests	$n = 6rev/min$
Maximum output torque during tests	$T_{out} = 950Nm$
Input flow during tests	$Q_{in} = 11.5l/min$

there are asperity contacts and therefore mechanical friction between SOI. This friction loss depends on the normal force between SOI which decreases when p_h increases. After $T_{loss,min}$ the lubricating regime between SOI is EHL and the corresponding friction loss is due to oil shearing. Hence, the dominating torque loss variation is from the vane-stator and stop-rotor contacts, which increase with p_h. The measured h_{MCA} values are in agreement with the proposed loss behavior. They increase with p_h and the value of p_{c2} has a significant effect on h_{MCA}. The trend of the h_{MCA} curves is that the gap pressure distribution between the SOI has to overcome the compensation pressures before the gap height starts to increase. The h_{MCA} measurements are in μm which implies some uncertainties due to rotor surface asperities and thickness variations of the same order of magnitude. E.g. the curve for $p_{c2} = 27bar$ is expected to be below the curve for $p_{c2} = 22bar$ and then the gap height does not start to increase inside the pressure range of the tests.

It is expected that $T_{loss,min}$ occurs when the minimum gap height is just above zero for the entire SOI. But due to uneven height distribution over the SOI, the gap height for the entire SOI is not zero or above zero, when h_{MCA} starts to measure deflections above zero. This is also confirmed by the model put forward in section 4.

4 Torque Loss Modeling of the Prototype Motor

The aim of this section is to set up a model of the torque loss as a function of the pressure levels.

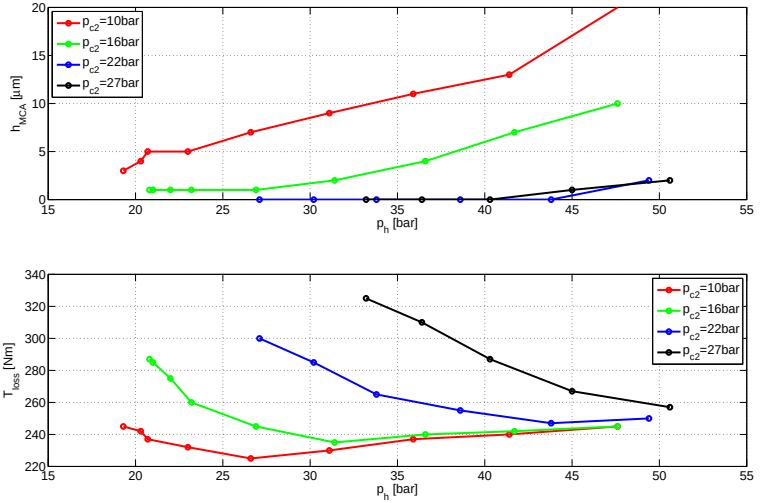

Figure 5: The measured deflections of the inner housing h_{MCA} (top graph) and the measured torque losses T_{loss} (bottom graph). Both are plotted with respect to the high pressure p_h.

4.1 Torque Loss of Hydraulic Motors

The friction loss of hydraulic motors depends on the tribology of the surfaces moving relative to each other and it depends on the operational parameters of the motor. They are speed n, pressure p and viscosity μ, which are related to the total torque loss T_{loss} as (Ivantysyn and Ivantysynova, 2003)

$$T_{loss} = T_{turb} + T_{visc} + T_{mech} + T_{cst} \quad (2)$$

$$= C_{turb} \cdot \mu \cdot n^2 + C_{visc} \cdot \mu \cdot \frac{n}{h} + C_{mech} \cdot \Delta p + C_{cst}, \quad (3)$$

where T_{turb} is torque loss due to friction in turbulent flow, T_{visc} is due to viscous friction, T_{mech} is due to mechanical friction and T_{cst} is constant torque loss mainly due to sealings. The gap height is denoted h.

Eqs. (2) and (3) describe the conceptual behaviour of the torque loss. The torque loss coefficients C are those varying for different torque loss models and different motor principles. In the litterature these loss coefficients were first given as constants (Wilson, 1946). Later on it was shown (McCandlish and Dorey, 1984) that both linear and nonlinear loss coefficients give more accurate results over a wider range of operating conditions.

In this work the velocity and viscosity are held constant. Hence, eq. (3) is reduced to

$$T_{loss} = C_{visc} \cdot \mu \cdot \frac{n}{h} + C_{mech} \cdot \Delta p + C_1. \quad (4)$$

The term $C_{mech} \cdot \Delta p$ takes the friction force between vane-stator and stop-rotor into account and C_1 is the constant torque loss to a given velocity and viscosity. The $C_{visc} \cdot \mu \cdot n/h$ term describes the torque loss due to viscous friction between the SOI. The term relies on the SOI to remain separated and without any mechanical contact. But, according to the measurements, mechanical contact between SOI exists. The torque loss in these gaps highly depends on the gap height and, subsequently, the compensation pressures. Therefore, with constant velocity and temperature, the torque loss of the prototype motor is subdivided into

$$T_{loss} = T_{cst} + T_{mech} + T_{SOI} \quad (5)$$

$$= K_1 + K_2 \cdot \Delta p + T_{SOI}, \quad (6)$$

where K_1 and K_2 are loss coefficients derived from measurements.

From the experiments it is evident that there is a transition in the lubricating regime between the SOI. Depending on the pressure state the lubricating regime will, in general, go from boundary lubrication (BL) via mixed lubrication (ML) and towards elastohydrodynamic lubrication (EHL). The Stribeck curve that relates the shear friction, τ_{fric}, to the different friction regimes is illustrated in figure 6. From the T_{loss} and h_{MCA} curves in section 3 it seems that the lubrication between the SOI is ML and at the beginning of EHL during the tests.

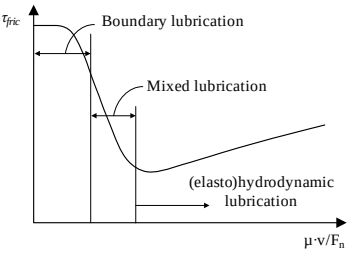

Figure 6: Stribeck diagram with lubrication regimes denoted.

The friction in the diagram of figure 6 is based on viscosity μ, velocity v and the normal force F_n between the gap surfaces (Bayer, 1994). The viscosity and velocity are constant during the tests. Hence, the friction loss variations only depend on normal force, according to figure 6. But there is only a normal force between the SOI when the gap height is zero in some regions. Even though the gap height is above zero, there is potentially still asperity contact, and mechanical friction, due to the roughness of the surfaces. From that point of view, F_n is not a valid parameter for the determination of the friction loss behavior in this case. Instead, the gap height distribution and the deflections of the surfaces are the parameters that influence the friction behaviour (Wang and Wang, 2006).

4.2 Computation of Gap Height by Fluid Structure Interaction (FSI) Simulation

The pressure distribution in the lubricating film between the SOI is influenced by the gap height which again influences the structural deflections. In this work the simultaneous computation of pressure and gap height is carried out by means of finite difference and finite element analyses, respectively, see also (Sørensen et al., 2012).

4.2.1 Gap Pressure

It is assumed that the rigid body motion of the rotor is only rotational and the density and viscosity of the oil is constant. Furthermore, the Reynolds equation is expressed in polar coordinates, because of the geometry and rotational motion of the rotor. Therefore the pressure distribution in the gaps between SOI is

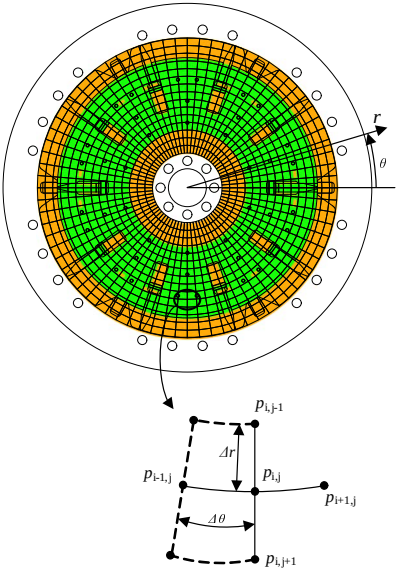

Figure 7: Finite difference mesh and boundary conditions. The color orange indicates that the pressure of the node is prescribed and green indicates that the pressure is to be determined.

(Beschorner et al., 2009)

$$\frac{\partial}{\partial r}\cdot\left(r\cdot h^3\cdot\frac{\partial p}{\partial r}\right)+\frac{1}{r}\cdot\frac{\partial}{\partial\theta}\cdot\left(h^3\cdot\frac{\partial p}{\partial\theta}\right)=6\cdot\eta\cdot r\cdot\omega\cdot\frac{\partial h}{\partial\theta}. \quad (7)$$

Eq. (7) is solved numerically using the finite difference method for one rotor position that is representative for the mean pressure state over one motor revolution. By dividing the area into elements (see figure 7) and approximating the derivatives in eq. (7) by finite differences, $p_{i,j}$ is expressed by its surrounding pressures and can be determined by looping through the mesh until the pressure variation from previous iteration ($p_{i,j}^{cur}-p_{i,j}^{prev}$) is smaller than a convergence tolerance.

4.2.2 Gap Height

The objective of the FEM model is to determine the structural deflections of the inner housing, which, with the end faces of the rotor, are forming the lubricating gaps of concern. The deflections of the rotor is assumed negligible because of the axial force balance. The input to the FEM simulations is the pressure distribution in the lubricating gap between the SOI and the vane actuation and compensation pressures. The output is the deflection of the face that forms the gap.

The pressures in the lubricating gap is added as nodal forces. The pressures from the fluid calculations are recalculated as nodal forces by

$$F_{i,j}=p_{i,j}\cdot r_{i,j}\cdot\Delta r\cdot\Delta\theta. \quad (8)$$

The principle behind the FEM model is shown in figure 8. The stator and the inner and outer housing are glued together to one body with a gap between the inner and outer housing. The boundary condition is no displacement in the normal direction to the section cut of the stator. The areas with the applied forces are symbolized by bold red lines in figure 8. The FEM model is meshed by three dimensional 8 node hexahedral elements.

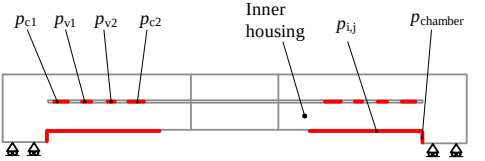

Figure 8: A section view of the FEM model with added pressures and boundary conditions.

4.2.3 FSI Results

The output from the FSI analysis is distribution of the gap height and the pressure between the SOI. The deflection of the inner housing that forms the gap and the pressure distribution in the gap to one test condition of the prototype motor are shown in figure 9. For the purpose of computational efficiency a linear FEM model was used in the FSI analysis, i.e., contact elements were not employed. The finite difference analysis is numerically limited in the way that it only converges as long as all gap heights are above a small threshold value, $h_\epsilon\approx 2nm$. Hence, for any FSI analysis the inner housing and the rotor are given an initial position that ensures $h_{min}^{(FSI)}>h_\epsilon$ for any load situations, see figure 10.

This gap height distribution is only valid for situations where the SOI are fully separated. In order to include situations where the SOI are partly separated or not separated at all, an offset gap height, h_o, is introduced. This offset value is subtracted from the FSI gap height to yield a nominal gap height, see also figure

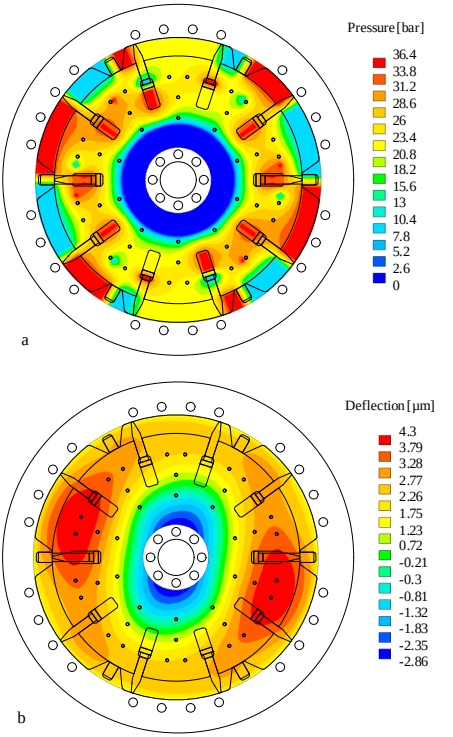

Figure 9: The simulated pressure distribution (a) and the deflection of the inner housing (b) to one test condition of the prototype motor.

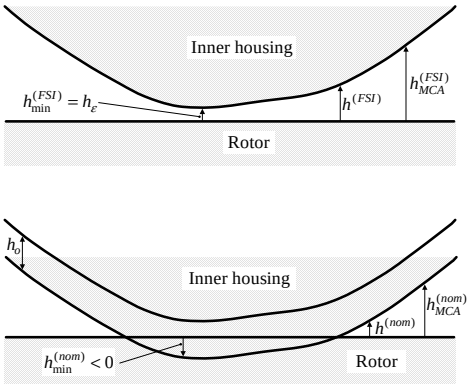

Figure 10: Illustration of $h^{(nom)}$, $h^{(FSI)}$ and h_o.

10:

$$h^{(nom)} = h^{(FSI)} - h_o. \tag{9}$$

The offset gap height is identified by fitting the nominal gap height with the measured gap height at the MCA in situations where the SOI are fully separated yielding a value of $h_o = 7.5\mu m$. The result of this is shown in figure 11 where a good accordance between gap increase vs. high pressure is observed for situations where the SOI are fully separated.

4.3 Torque Loss based on Gap Height

The total shear stress between the SOI, τ_{fric}, in the ML regime is given by the sum of the shear stress of the asperity contacts, τ_{asp}, and the shearing of the oil, τ_{fluid}, as (Gelinck and Schipper, 2000)

$$\tau_{fric} = \tau_{asp} + \tau_{fluid} \tag{10}$$

$$= \mu_{fric}(h') \cdot p' + \mu \cdot \frac{v}{h'}, \tag{11}$$

where $\mu_{fric}(h') \cdot p'$ is the shear stress of the asperity contacts and $\mu \cdot v/h'$ is the shear stress of the fluid. The friction coefficient function between the asperities, μ_{fric}, is a function of the gap heights, given by

$$\mu_{fric}(h') = K_3 \cdot e^{-\frac{h'-h_{thr}}{h_{thr}}}, \tag{12}$$

where h_{thr} is a treshold gap height that determines if mechanical contact. p' and h' are

$$h' = \begin{cases} h_{thr} & \text{if } h^{(nom)} < h_{thr} \\ h^{(nom)} & \text{if } h^{(nom)} \geq h_{thr} \end{cases}, \tag{13}$$

$$p' = \begin{cases} p - K_4 \cdot h^{(nom)} & \text{if } h^{(nom)} < h_{thr} \\ p & \text{if } h^{(nom)} \geq h_{thr} \end{cases}. \tag{14}$$

By introducing h' singularities are avoided and a smooth transition from ML to EHL is ensured. Negative values of the nominal gap height correspond to a certain amount of indentation in the SOI. This is taken into account by means of the simple linear stiffness introduced in eq. (14) that is considered adequate to capture the increase in contact pressure.

Hence, the total simulated torque loss of the prototype motor, $T_{loss}^{(sim)}$, is

$$T_{loss}^{(sim)} = T_{cst}^{(sim)} + T_{mech}^{(sim)} + T_{SOI}^{(sim)} \tag{15}$$

$$= K_1 + K_2 \cdot \Delta p + \tau_{fric} \cdot A \cdot r, \tag{16}$$

where A is area and r is radius.

5 Results and Comparison

The coefficients in the torque loss expressions are determined based on the measurements.

5.1 Parameter Identification

K_1	$161Nm$
K_2	$19.4 \cdot 10^{-6} m^3$
K_3	$1.66 \cdot 10^{-3}$
K_4	$2.38 \cdot 10^{12} Pa/m$
h_{thr}	$1.06 \cdot 10^{-6} m$

Table 2: Parameters derived from the tests.

The coefficients in the torque loss model are determined from the measurements by curve fitting as listed in table 2. The individual torque losses are shown in figure 12. The constant term is very dominating.

5.2 Comparison of Experimental and Simulated Torque Loss

Both the experimental and simulated total torque losses are shown in figure 13. The simulated total torque losses are determined by torque loss evaluations for every node on both side of the rotor. There is good correlation between the curves, which verify the friction model of section 4.3. The effect of p_{c2} on the hydro-mechanical efficiency when velocity and viscosity are constant is shown in figure 14.

6 Conclusions

In this paper a model describing the torque losses in a hydraulic motor principle has been developed and ex-

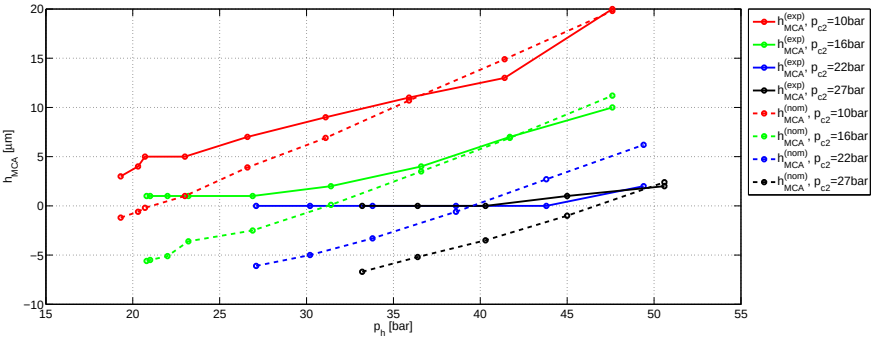

Figure 11: The simulated and experimental MCA deflections for the different p_{c2} values.

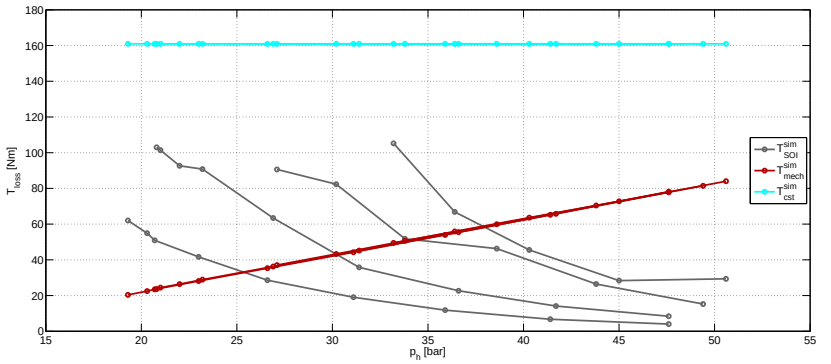

Figure 12: The individual simulated torque losses based on eq. (16) and after parameter identification.

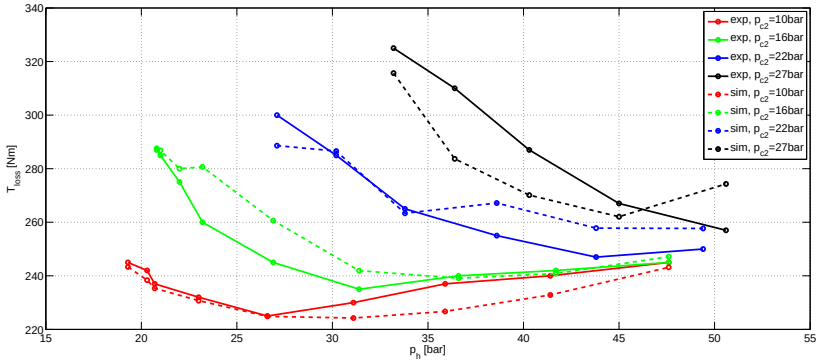

Figure 13: The simulated and experimental torque loss for the different p_{c2} values.

perimentally verified. The model describes the torque losses associated with mechanical and viscous friction under different lubricating conditions. The overall model is based on sub models of both the lubricating gap and the shear stress on the SOI. An FSI model is utilized for the computation of gap height and pressure distribution.

The most complex contribution to the hydromechanical loss is the friction loss between the SOI. The lubrication regime is either predominantly ML or predominantly EHL and the loss condition is highly dependent on the gap heights. In the FSI model there is mechanical contact if $h^{(nom)} < h_{thr}$. The behavior of the friction loss follows that of the Stribeck curve which only changes with the gap height in this study. The comparison of the simulated and measured hydromechanical loss shows a good correlation after the determination of the loss coefficients.

The correlation between the simulated and measured hydromechanical loss confirms the understanding of the interaction between the SOI. At the beginning of the T_{loss} curves there are ML between the SOI with transition towards EHL when the total gap height is above zero.

The aim of the model development is a computational tool that can predict the effects and consequences of an up-scaling or modification of the motor principle, and, subsequently, minimizing the demands for prototyping. The potential for a further increase in specific displacement is increased when the motor is up-scaled. The aim is to up-scale the motor to displacements in the range of $200 \ldots 500 l/rev$ in a very compact form, for extraordinary low speed high torque applications. Hence, minimization of structural deflec-

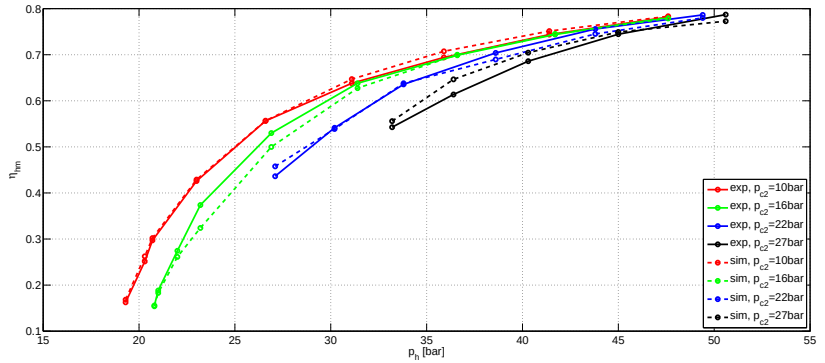

Figure 14: The simulated and experimental hydro-mechanical efficiency.

tions are envisaged to be crucial in order to reach useful efficiencies over a wide range of operating conditions.

References

Bayer, R. *Mechanical Wear Prediction and Prevention*. Marcel Dekker, 1994.

Beschorner, K., Higgs, C., and Lovell, M. Solution of reynolds equation in polar coordinates applicable to nonsymmetric entrainment velocities. *Journal of Tribology*, 2009. 131.

Gelinck, E. and Schipper, D. Calculation of **S**tribeck curves for line contacts. *Tribology International*, 2000. 33:175–181. doi:10.1016/S0301-679X(00)00024-4.

Ivantysyn, J. and Ivantysynova, M. *Hydrostatic Pumps and Motors: Principles, Design Performance, Modelling, Analysis, Control and Testing*. Tech Books International, 2003.

Ivantysynova, M. Prediction of pump and motor performance by computer simulation. *First International Conference on Computational Methods in Fluid Power Technology*, 2003.

McCandlish, D. and Dorey, R. The mathematical modelling of hydrostatic pumps and motors. *Proc Instn Mech Engrs*, 1984. 198B(10).

Murrenhoff, H., Piepenstock, U., and Kohmäscher, T. Analysing losses in hydrostatic drives. *Proceedings of the 7th JFPS International Symposium on Fluid Power*, 2008.

Sørensen, R., Hansen, M., and Mouritsen, O. Hydraulic yaw system for wind turbines with new compact hydraulic motor principle. *EWEA 2011 Scientific Proceedings*, 2011. pages 111–114.

Sørensen, R., Hansen, M., and Mouritsen, O. Numerical and experimental study of hydrostatic displacement machine. *International Journal of Fluid Power*, 2012. 13(2):29–40.

Wang, Y. and Wang, Q. Development of a set of **S**tribeck curves for conformal contacts of rough surfaces. *Tribology Transactions*, 2006. 49:526–535. doi:10.1080/10402000600846110.

Wilson, W. Rotary pump theory. *Transaction of the ASME*, 1946. pages 371–383.

Paper C

Investigation of Hydraulic Motor Principle for Low Speed High Torque Applications

Rasmus M. Sørensen, Michael R. Hansen, Ole Ø. Mouritsen

In *Proceedings of the 22th. Nordic Seminar on Computational Mechanics*, 2009, Aalborg, Denmark

Investigation of Hydraulic Motor Principle for Low Speed High Torque Applications

Rasmus Mørk Sørensen*
Department of Mechanical Engineering
Aalborg University, Aalborg, Denmark
e–mail: rms@me.aau.dk

Michael Rygaard Hansen
Department of Engineering
University of Agder, Agder, Norway
e–mail: michael.r.hansen@uia.no

Ole Ø. Mouritsen
Department of Mechanical Engineering
Aalborg University, Aalborg, Denmark
e–mail: oom@me.aau.dk

Per Fenger
Liftra Aps, Aalborg, Denmark
e–mail: pef@liftra.dk

Summary A new hydraulic high torque low speed motor principle is introduced. The motor is characterized by a specific displacement that is at least an order of magnitude higher than that of commercially available motors. The basic geometry, design variables and governing equations are presented. Comprehensive leakage flow calculations and a detailed dynamic simulation has been used together with testing of a prototype to predict the performance of the motor.

Introduction

Hydraulic motors have some basic advantages that may be utilized in different applications. First of all, it is possible to have a high torque density. This enables hydraulic motors to deliver high torques without occupying large amounts of space. This advantage is further developed in the motor principle put forward in this paper. To examine the motor principle thoroughly, experiments have been carried out both on simulation models and on a physical prototype. The main purpose of this study is simply to highlight the motor principle and describe the derived design considerations that will be implemented on the next generation.

Motor Principle

The motor principle is like a rolling vane motor [2] and a Rolling Abutment Motor [3] in the general design, but is overall more simple because any outside timing is avoided. The main difference is that the vanes are moving in radial direction and the stops are fixed. The motor is illustrated in figure 1 using 4 chambers, however, it can be designed with n-chambers. The rotor is rotating because of pressure difference around the 5 (n+1) vanes. The stops form 4 chambers with either one or two vanes inside. To maximize displacement and output torque, the number of chambers should be maximized. The volumetric efficiency is due to internal leakage flow, why gaps between the individual parts must be kept as low as possible without introducing actual mechanical contact between the moving parts since this would introduce hydromechanical losses.

In figure 1 the basic design variables are shown and the motor displacement pr. rev. is:

$$D = 2 \cdot \pi \cdot n \cdot R \cdot S \cdot H, \tag{1}$$

where n is number of chambers.

Performance

The performance and efficiency are influenced by various parameters. In this work leakage flow has been investigated theoretically with a view to specify acceptable production tolerances. The 1. dimensional leakage flow Q around the vanes and stops is given as

$$Q = \frac{w \cdot h^3}{12 \cdot \mu \cdot L} \cdot \Delta p \quad [1], \tag{2}$$

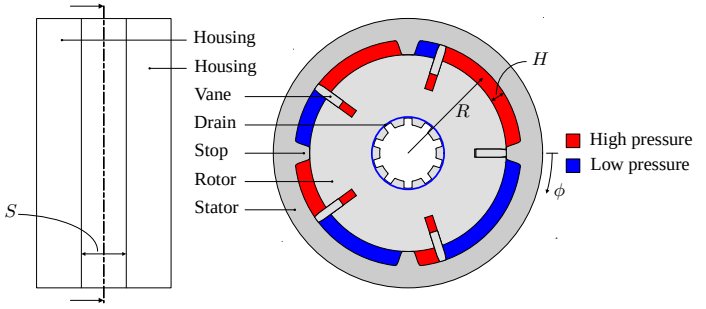

Figure 1: Motor principle with characteristic, design variables, name conventions and pressure volumes. A motor chamber is defined to consists of both the low- and the high pressure volume between 2 stops.

where w, h and L are the geometry of the leakage path and μ is the dynamic viscosity of the fluid. The leakage flow across both end planes of the rotor is 2. dimensional and thereby more complex to estimate. Reynolds equation in polar coordinates is used. For a constant gap height it yields the following differential equation:

$$\frac{\partial^2 p}{\partial r^2} + \frac{1}{r}\frac{\partial p}{\partial r} + \frac{1}{r^2}\frac{\partial^2 p}{\partial \beta^2} = 0, \tag{3}$$

where r is the radial coordinate and β is the angular coordinate. (3) solved for p by a numeric finite difference method to one rotor angle is illustrated in figure 2. Clearly, the pressure distribution varies when the rotor rotates, however, the leakage flow that is an integrated value has quite small variations. The pressure distribution obtained by solving (3) can be used to compute the leakage flow across the disc, in the r- and β direction respectively, as follows:

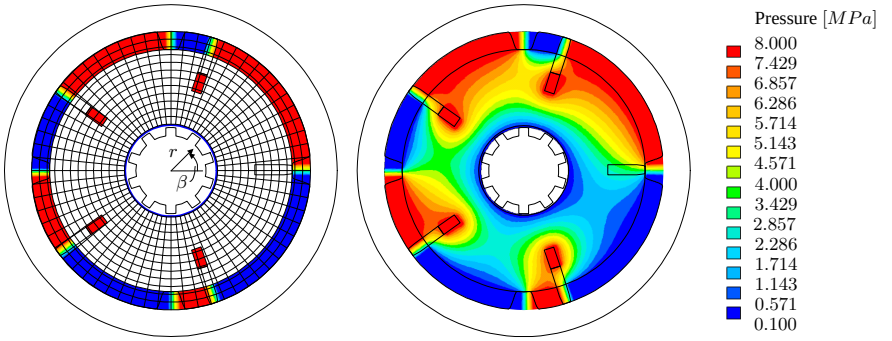

Figure 2: Left: Boundary conditions, coordinate system and unrefined finite difference mesh. Right: Pressure across rotor. (3) solved by the numeric finite difference method.

$$Q_r = -\frac{1}{12\mu} \cdot h^3 \cdot \frac{\partial p}{\partial r} \cdot r_k \cdot \Delta\beta \quad [4] \tag{4}$$

$$Q_\beta = -\frac{1}{12\mu} \cdot h^3 \cdot \frac{1}{r_k}\frac{\partial p}{\partial \beta} \cdot \Delta r + \frac{1}{2} h \cdot \omega \cdot r_k \cdot \Delta r \quad [4], \tag{5}$$

To scrutinize the behaviour of the motor principle, to specify production dimensions and tolerances and to get an overview of the coherence between different factors in the motor, the motor has

been subjected to a time domain simulation. The input to the dynamic simulation is a flow into the motor and the state variables comprise the pressure in the different chambers as well as the angular position and velocity of the rotor. The leakage flows from (2), (4) and (5) are used as lookup tables in this simulation. In figure 3 the result of the dynamic simulation is illustrated as power in and power out from the motor. This is with all gaps at $h = 0.02mm$ and without any influence from friction, i.e., all losses are volumetric. The irregularity after $\approx 6.5s$ is because the rotational direction is changing at that time by reversing the input flow. The small fluctuations in the curves are because of fluctuations in the leakage flow. The rotational speed in the dynamic simulation is $2\frac{rev}{min}$.

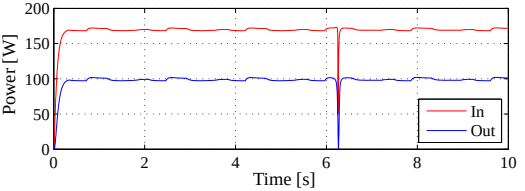

Figure 3: Power in (red) and out (blue) in the dynamic simulation. The efficiency is around 0.57.

Prototype

The prototype is designed with a displacement $D = 190\frac{cm^3}{rev}$. The motors outer dimensions is $200mm$ in diameter and $100mm$ in height. The specific displacement is $D' = \frac{D}{V} = 0.06\frac{1}{rev}$. Neither the size of the chambers nor the number of chambers have been optimized with respect to performance since the main purpose was to investigate the principle. Potentially, the performance, i.e., torque density, of the prototype could be increased by an order of magnitude simply by increasing S, H or N.

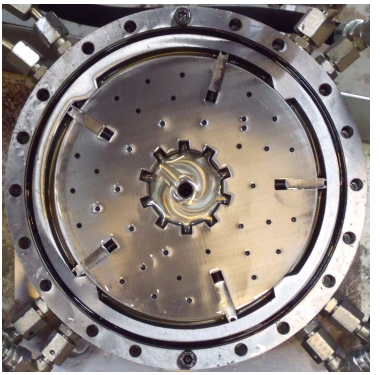

Figure 4: Prototype design.

A picture of the prototype is shown in figure 4. The vanes are forced against the stator by springs and hydrostatic pressure and are therefore always sliding along the stator. The curvature of the stops is forcing the vanes in when passing a stop. There are one oil inlet and one outlet to each chamber, fitted in each stop. The rotor is perforated with small holes to ensure the same pressure at each end plane and therefore minimize mechanical friction.

Experimental Results

The Prototype is tested in a test bench, shown in figure 5. The load on the motor is added by a powder brake through a gearbox. The resistance torque in the test bench is proportional to a voltage signal supplied to the powder brake. To be able to calculate the motors efficiency, the test bench is fitted with different measurement devices; The oil flow into and returned from the motor are measured with flow transducers, the pressure in the oil into and returned from the motor are measured with pressure transducers, the output torque from the motor is measured with a full bridge strain gauge circuit mounted at the output shaft and the angular velocity of the motor is measured by a high resolution encoder. Testing has shown, that the internal friction is quite high

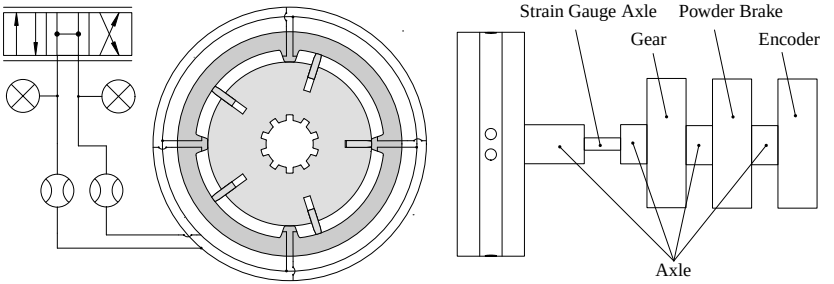

Figure 5: Test setup with all its components and their location. The parts named are just visualized by boxes, but their location is okay.

which affects the motion of the motor, however, the main focus has been on the leakage flow. In general, the leakage flow has increased with increased pressure level. In figure 6 the volumetric efficiency is shown together with the theoretical values obtained by means of simulation. The graphs fluctuates quite much because of irregularities in the angular velocity. The leakage flow is, in general, higher than expected. The main reasons for that are:

- the rotor is not radially balanced causing the leakage paths between stops and rotor/vane to be too high.
- the spring actuation of the vanes does not always function properly, i.e., the vanes are hanging.

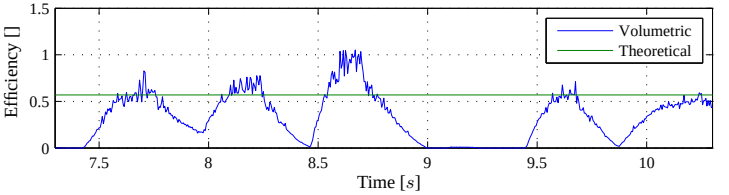

Figure 6: Prototype volumetric efficiencies during one rotation. Green is theoretical and blue is measured.

Concluding remarks

A hydraulic vane motor principle is presented. The motor principle is characterized by a very high torque density. Time domain simulation is carried out with a view to examine the volumetric efficiency as well as the general dynamic behavior of the motor during start, stop and reverse. The time domain simulation utilizes numerical results on leakage flows as lookup tables.

A prototype has been developed and tested. The prototype has a displacement of $D = 190\frac{cm^3}{rev}$ and a specific displacement of $D' = 0.06\frac{1}{rev}$. Simulation and measured results clearly indicate that the volumetric losses are higher in practice than in theory. The main reason for this has been identified as unbalanced radial force on the rotor as well as non-optimal vane behavior.

References

[1] M.R. Hansen and T.O. Andersen. *Notes on Fundamental Hydraulics*. Aalborg University, (2007).

[2] J. Ivantysyn and M. Ivantysynova. *Hydrostatic Pumps and Motors*. Technip Books International, New Delhi, First english edition, (2003).

[3] `www.vonruden.com/hydraulic_motors/rolseal/rol-seal_cutaway.html`. Von Ruden Manufacturing, Buffalo, Web page (12.08.2009).

[4] P.R. Trumpler. *Design of Oil Film Bearings*. MacMillian, (1966).

Paper D

Hydraulic Yaw System for Wind Turbines with New Compact Hydraulic Motor Principle

Rasmus M. Sørensen, Michael R. Hansen, Ole Ø. Mouritsen

In *Proceedings of the European Wind Energy Association Conference*, 2011, Brussels, Belgium

Hydraulic Yaw System for Wind Turbines with New Compact Hydraulic Motor Principle

Rasmus Mørk Sørensen * **Michael Rygaard Hansen** ** **Ole Ø. Mouritsen** ***
Per E. Fenger ****

* *Aalborg University & Liftra, Aalborg, Denmark (e-mail: rms@liftra.dk)*
** *University of Agder, Grimstad, Norway (e-mail: michael.r.hansen@uia.no)*
*** *Aalborg University, Aalborg, Denmark (e-mail: oom@m-tech.aau.dk)*
**** *Liftra, Aalborg, Denmark, (e-mail: pef@liftra.dk)*

Abstract:

This paper presents a new hydraulic yaw system for wind turbines. The basic component is a new type of hydraulic motor characterized by an extraordinary high specific displacement yielding high output torque in a compact form.

The focus in the paper is the volumetric efficiency of the motor, which is based on leakage flow. The most critical gaps in the motor, across the end faces of the rotor, are investigated both by a fluid structural interaction simulation model and by experimental prototype tests. The simulation model is the basis for the motor design and the manufacturing tolerances.

The volumetric efficiency is highly dependent on the structural deflections caused by the pressure distribution in the fluid films across the rotor. This gap height is measured with a $0.1\mu m$ resolution "SMAC Moving Coil Actuator" in the experimental test setup. When the pressure in the pressure compensation volumes is minimizing the deflections, the measured gap height is around $h = 10\mu m$ and the volumetric efficiency of the motor is around $\eta_v = 0.85$. By decreasing the initial gaps from the manufacturing process, this volumetric efficiency can be further increased.

Keywords: Hydraulic Motor; Wind Turbine; Yaw System; Efficiency; Structural deflections; Reynolds equation.

1. Introduction

Reliability is an important issue for wind turbine manufactures. The yaw system is related to reliability problems [1, 2]. Today the conventional yaw system of wind turbines with active yaw system, consists of a number of electric motors connected to a large gear rim through a gearbox [3, 4, 5, 6]. The motors are mounted at the nacelle and the gear rim is mounted at the tower. The torque from the electric yaw motors are transferred to the nacelle via a number of pinion-gear rim connections. The high speed reduction and torque increase from the yaw motors to the yaw gear rim is related to wear at the gear connections. The wind angle is fluctuating which causes the yaw system to reposition the nacelle. The amplitude of these wind angle fluctuations is low and therefore only few teeth at the yaw gear rim are active in transmitting the torque. It is possible to either fix or partially allow the position of the nacelle to slightly change when in the desired wind angle. Both approaches are subjected to problems. If the nacelle is fixed with brakes the wind loads at the yaw system are transferred to the nacelle and tower without damping, causing damaging vibrations in the structure. These vibrations are reduced if partially allowing the position of the nacelle to change when wind gusts. This solution is, however hard for the gear meshes in the yaw system. If wind gusts are allowed to move the nacelle, the angular velocity at the yaw gear rim is transferred through the gearbox to the electric motors without any damping. This causes peak loads at the individual teeth in the system. Another disadvantage in the conventional yaw system is the necessity of more than one yaw motor to deliver the required torque to the yaw gear rim. The tower and the nacelle are flexible structures which influences the individual gear meshes between yaw gear rim and the gearbox pinions. Therefore the yaw motors do not share the torque transmission equally, thereby further increasing the variation in load experienced by the individual particular teeth of the gear rim.

This paper is an outcome from research work on a new hydraulic yaw principle. The main goal of the research is to develop a new hydraulic motor principle [7, 8] that is suited for the wind turbine yaw system with a view to avoid the fundamental disadvantages associated with the pinion-gear rim connections used today. The motor is characterized by its specific displacement, i.e. its displacement per outer volume. It has a specific displacement substantially higher than that of commercially available hydraulic motors. Therefore it can deliver a very high torque output without occupying much space.

The motor principle is illustrated in figure 1. The design shown uses 6 chambers, however, it can be designed with n_{Ch} chambers. The rotor is rotating because of pressure difference across the vanes. The stops form 6 chambers with either one or two vanes inside. The vanes are moved in radial direction when passing a stop. To maximize displacement and output torque, the number of chambers and the motor dimensions must

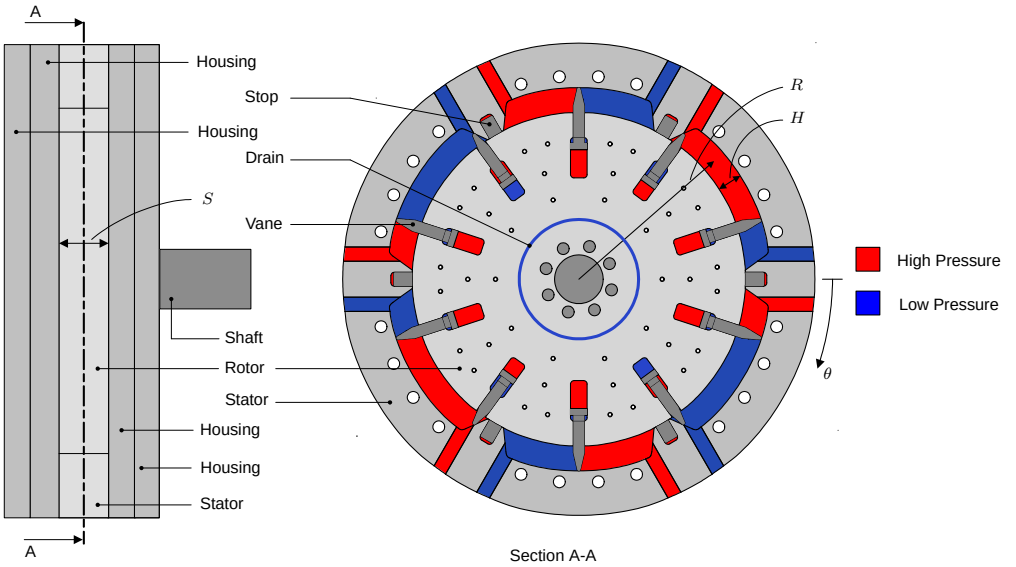

Fig. 1. Motor principle. The pressure difference across the vanes is forcing the rotor to rotate in clockwise direction. The red color symbolizes high pressure oil and the blue is low pressure oil.

be maximized. In figure 1 the basic design variables are shown and the motor displacement pr. rev. D is:

$$D = 2 \cdot \pi \cdot R \cdot S \cdot H \cdot n_{Ch}. \quad (1)$$

In (1) the basic design parameters of the motor may be found.

The vanes are shaped as a piston to be able to be actuated by pilot pressures. Small oil connections in the housing supplies the vanes and secures that they are forced in and out when passing a stop. In figure 1 this feature is illustrated by comparing the pressures at the vanes that are passing a stop, and the others. The oil connections to the chambers are from holes in the stator in each end of the chambers, see also figure 1. The task of the stops is to separate the chambers. To prevent leakage flow from chamber to chamber the stops are forced against the rotor. Using a hydraulic pressure to maintain contact increases the complexity of the motor and introduces additional friction. It does, however, reduces the demands for fine tolerances in the housing.

The main reason for leakage flow is the axial gaps (end faces) between rotor and housing. These gaps are necessary to avoid mechanical friction, but must be at a minimum to minimize leakage flow (the size of the gaps between the moving parts is in the $\frac{1}{100}mm$ range). The oil is flowing from the chambers and the vane actuation volumes to the drain across the end faces of the rotor. This flow is causing a hydrostatic pressure against the housing, and therefore deflections, which increases the gaps between rotor and housing. To prevent these deflections the motor is equipped with pressure compensating chambers in the housing.

State of Art for Hydraulic Motors

In table 1 the prototype is compared with two commercial large low speed high torque hydraulic motors from Bosch Rexroth [9] and Hagglunds [10]. Both motors are of the type radial piston motor, which is the dominating type when the need is a very high torque.

	Bosch Rexroth MRE8200 [9]	Hagglunds MB4000 [10]	Prototype
Motor type	Radial piston	Radial piston	
Displacement $\left[\frac{cm^3}{rev}\right]$	8 226	251 323	1 751
Motor volume $\left[cm^3\right]$	253 400	3 507 000	9 621
Specific displacement $\left[rev^{-1}\right]$	0.033	0.072	0.182

Table 1. Motor comparison.

As listed in table 1 the new hydraulic motor principle is favourable when comparing specific displacement, i.e. displacement per outer motor volume. Potentially, this allows for very compact motors used for direct drive applications with high torque requirements. One of the major challenges in the field of hydraulic motors is the efficiency. It depends on both design and manufacturing parameters. Manufacturing tolerances, which determine the internal gaps, is one important efficiency parameter. Gaps between the moving parts are necessary to avoid mechanical contact, but must be at a minimum to decrease the leakage flow.

In the wind turbine yaw system the motor is intended to be used in two ways and two sizes. Firstly the new yaw system consists of small hydraulic motors in mesh with the yaw gear rim. The overall structure is like the existing one, except that the high reduction gearbox is saved because the individual motors is delivering the necessary amount of torque, as illustrated in figure 2. The new motor principle has some advantages when up-scaling. The number of leakage gaps are not increasing linearly with the output torque. Therefore the second potential yaw application is one large yaw motor shaped as a ring in the same size as the existing yaw gear rim, as illustrated in figure 3. In this application the motor has e.g. 40 chambers located in a radius equal to that of the wind turbine tower. The stator of the motor is bolted on the tower and the rotor on the nacelle, or opposite. In this yaw system solution the motion is solely carried by the hydraulic oil. Every gear meshes are avoided. The new hydraulic yaw system is potentially a more simple, reliable and soft moving (because of the elasticity in the oil) system, compared to the existing electrical system.

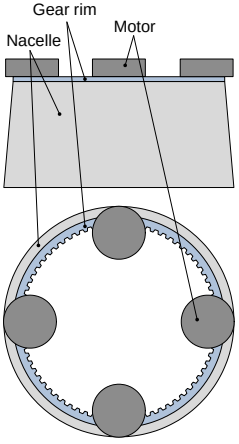

Fig. 2. Hydraulic yaw system with more small motors.

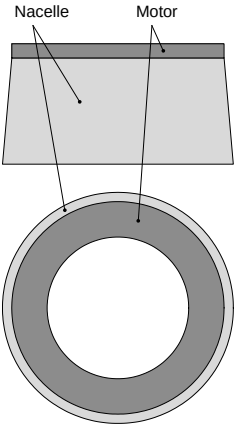

Fig. 3. Hydraulic yaw system with only one motor and no gearings.

This paper is concerned with this new hydraulic principle. The main contribution is a simulation model that is capable of handling the fluid-structure interaction around the main leakage paths of the motor. Also, experimental test data is put forward and compared with the developed simulation model with a view to strengthen the model based design approach in the ongoing upscaling of the motor to fit the yaw system of large commercial wind turbines.

2. Simulation Model

To validate the motor principle and its critical leakage ways, and to know about the manufacturing tolerance demands for the motor, a fluid structural interaction (FSI) simulation model of the motor is set up. The main validation parameter in this paper is the volumetric efficiency of the motor, expressed by the gaps between housing and the end faces of the rotor. The outputs from the simulation model are compared with experimental prototype tests.

The inputs to the FSI simulation model are the pressure level in the motor and the initial even gaps between housing and the end faces of the rotor, given by manufacturing tolerances. During run, a pressure distribution will appear in these gaps, when oil is flowing from the high pressure to the low pressure regions. This pressure distribution can be modeled by means of Reynolds equation, which is the differential equation governing the pressure distribution in fluid film lubrication.

It is assumed that the only rotor movement is rotational and the viscosity μ and density ρ of the oil are constant. Reynolds equation is expressed by polar coordinates (r, θ) (see figure 4), because of the geometry and rotational movement in the motor. Therefore the pressure distribution in the gaps between the housing and the end faces of the rotor is

$$\frac{\partial}{\partial r}\left(rh^3\frac{\partial p}{\partial r}\right)+\frac{1}{r}\frac{\partial}{\partial \theta}\left(h^3\frac{\partial p}{\partial \theta}\right)=6\mu r\omega\frac{\partial h}{\partial \theta} \quad [11], \quad (2)$$

where p is pressure, h is gap height and ω is the angular velocity of the rotor.

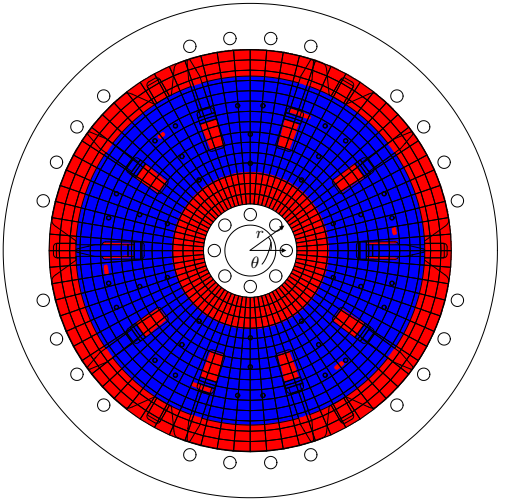

Fig. 4. Finite difference mesh (shown coarse for illustration) and boundary conditions. Where red the pressures are prescribed and fixed and where blue the pressures are determined during the relaxation.

(2) is solved numerically using the finite difference method for one rotor position. By dividing the area into small elements (see figure 4) and approximating the derivatives in (2) by finite differences, $p_{i,j}$ is expressed by its surrounding pressures. From the surrounding pressures $p_{i,j}$ is corrected for the entire mesh. The final $p_{i,j}$ is determined by looping through the mesh until the pressure variation from previous iteration ($p_{i,j}^{cur} - p_{i,j}^{prev}$) is

smaller than the convergence statement. The boundary conditions to this finite difference method is the fixed pressures in the drain, in the chamber volumes and in the radial actuation volumes of the vanes. It is assumed that the pressure decreases linearly across both stops and vanes.

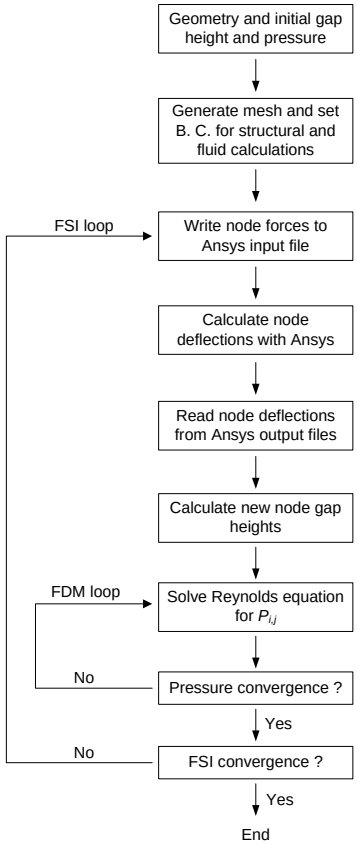

Fig. 5. Flow chart representing the FSI simulation model.

The structure of the FSI simulation model is shown in the flow chart in figure 5. The pressure distribution across the end faces of the rotor and the pressures in the chambers are causing deflections in the housing and the rotor. These deflections are determined in individual finite element method (FEM) analyses, which are a part of the FSI simulation model. The pressures are written to text files during the simulation and act as load input to the structural FEM calculations. The output from the FEM calculations are the deflections of the surfaces that form the gaps. These surface deflections, both rotor and housing, are added to the initial gap height and forms the input to the next iteration in the FSI simulation. In this next iteration a new pressure distribution is determined from the new gap distribution and so on.

The input to the FSI simulation model are the surrounding pressures that are obtained experimentally from the prototype. Also, an initial uniform gap height must be supplied to the FSI simulation. The pressure in the high pressure volumes of the chambers is $p = 39bar$, in the low pressure volumes $p = 6.5bar$, in the drain $p = 1bar$, in the compensation volumes $p = 35bar$ and the initial uniform gap height is $h = 0.02mm$. The pressure distribution from the FSI simulation model across one side of the rotor is shown in figure 6.

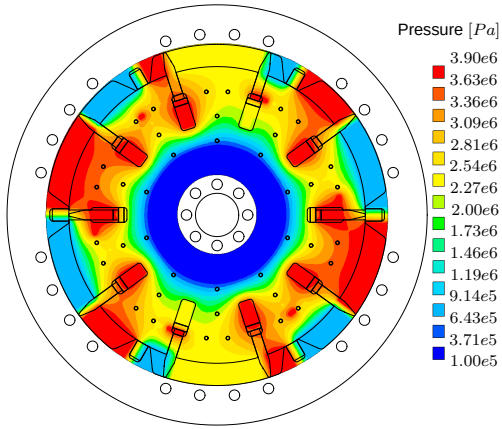

Fig. 6. Pressure distribution across one side of the rotor.

The change in gap height between one side of the rotor and its facing housing, corresponding to the pressure distribution in figure 6, are shown in figure 7.

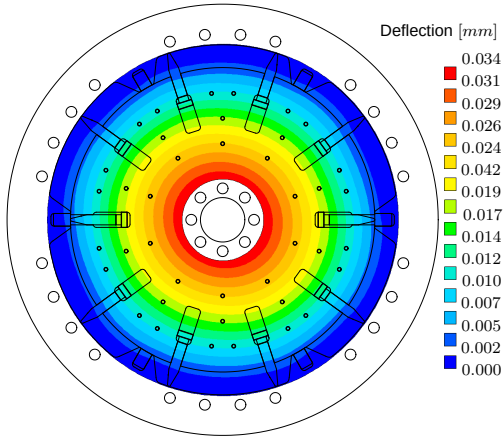

Fig. 7. Housing and rotor deflections.

3. Motor efficiencies

The efficiency of hydraulic motors is divided in hydro-mechanical η_{hm} and volumetric η_v efficiency. The hydro-

mechanical efficiency is the ratio between actual and theoretical output torque, given by

$$\eta_{hm} = \frac{M}{M_t} = \frac{M}{\Delta p \cdot H \cdot S \cdot R \cdot n_{Ch}}, \quad (3)$$

where M is the actual output torque from the motor, M_t is the theoretical output torque from the motor and Δp is the difference between high pressure and low pressure in the motor. R, H and S are motor dimensions as shown in figure 1.

The leakage flow across the end faces of the rotor is considered to be the dominating source to the volumetric efficiency. The volumetric efficiency for the hydraulic motor η_v is the ratio between the theoretical necessary flow to a certain angular velocity and the actual input flow, given as

$$\eta_v = \frac{Q_t}{Q} = \frac{R \cdot S \cdot H \cdot \omega \cdot n_{Ch}}{Q}, \quad (4)$$

where Q_t is the theoretical flow demand of the motor, Q is the actual flow demand to the motor, n_{Ch} is number of chambers and ω is the rotational speed of the motor.

The total efficiency of the motor η_{tot} is

$$\eta_{tot} = \eta_{hm} \cdot \eta_v. \quad (5)$$

4. Experimental Motor Testing

One of the main objectives with the developed prototype is to generate measured data that can be used to validate the simulation model.

The outer diameter of the prototype motor is $340mm$, the height is $106mm$ and the displacement is $D = 1.75\frac{l}{rev}$. The theoretical torque output from the motor is

$$\frac{T}{\Delta p} = \frac{D}{2\pi} = 28\frac{Nm}{bar}, \quad (6)$$

where T is torque and Δp is the pressure difference around the vanes.

The motor test setup is illustrated in figure 8. The motor is loaded by a powder brake. This powder brake is rated for smaller torques, whereas the connection is through a gearbox. The output torque of the motor is measured with strain gauge and the rotational position is measured with a digital encoder.

The fluid measurement equipment is four pressure transducers and two flow transducers (see figure 9). The total flow in and the total flow out of the chamber volumes are measured. The pressure is measured in the stop volumes, in the pressure compensation chambers and in the low- and the high pressure volumes of the chambers.

During the prototype tests the structural deflections are measured with a "SMAC Moving Coil Actuator" (MCA) mounted at the housing of the motor (see figure 10). This MCA is programmed in force mode to secure that the piston is always in contact with the rotor. The MCA is fitted with a $0.1\mu m$ optical encoder, which measures the position of the piston. Then the structural deflections

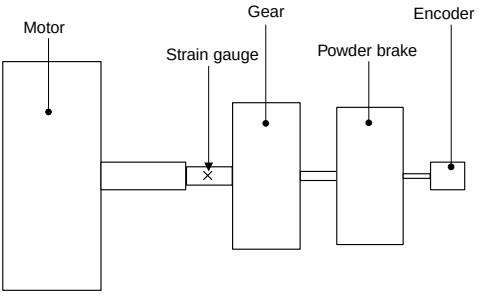

Fig. 8. The individual parts in the test setup.

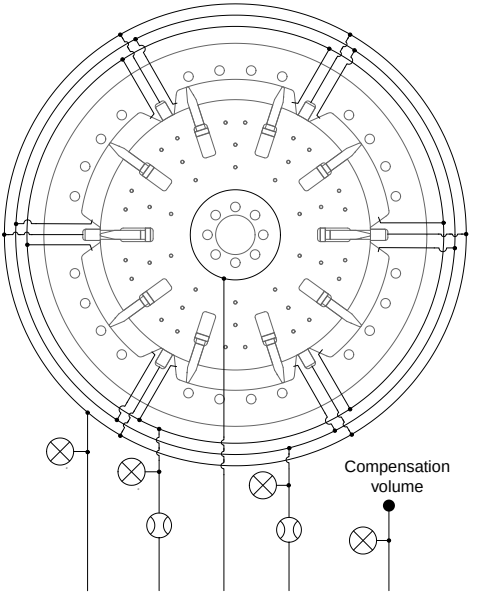

Fig. 9. The fluid measurement consists of two flow transducers and four pressure transducers.

and the axial movements of the rotor are the difference between the initial encoder position and the actual position.

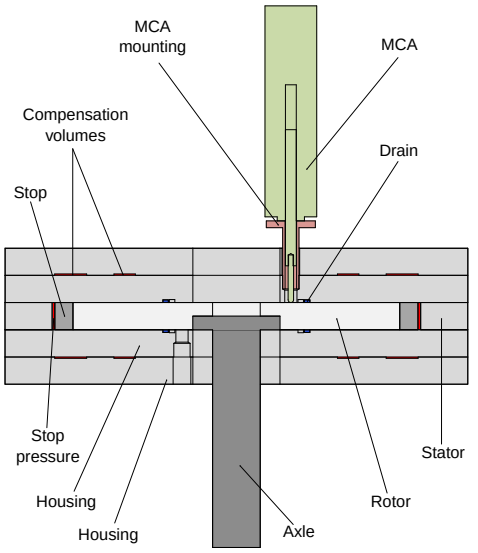

Fig. 10. The motor in a section cut. The MCA is mounted at the housing.

5. Test Results

The structural deflection of the housing and the volumetric efficiency is highly dependent on the chamber pressure and the pressure compensation chambers. Figure 11 shows a selected part (from $t = 580s$ to $t = 640s$) of a test run where the input flow is reduced in two steps (at time $t \approx 595s$ and $t \approx 613s$). The velocity is decreased with the input flow. The load is constant. All the measurements are fluctuating because of varying flow consumption to the radial vane actuation, but the mean values are overall stable and useful.

The first graph in figure 11 shows the pressures. It is interesting to notice that the compensation- and stop pressures are at a constant level. The pressures in the chamber volumes (p_1 and p_2) are reduced when the input flow is reduced. It is remarkable that the pressure difference ($\Delta p = p_2 - p_1$) is slightly decreased when the input flow is decreased, despite of the constant motor loading. The reason is decreased friction forces.

The second graph in figure 11 is shoving the output torque of the motor. This output torque is constantly fluctuating about $T = -650Nm$.

The third graph in figure 11 is the measured position of the MCA piston. These measurements are not absolute gap heights, but a combination of structural deflections and the axial movements of the rotor. The structural deflections are extracted from the measurements by subtracting the piston position just before the present pressure build-up (to time $t = 580s$) and considering the rotor to remain in its axial position and the roughness of the rotor surface has no influence. For the first input flow, and the corresponding pressure level, the deflection is $h = 50\mu m$. After the two input flow reductions and the corresponding pressure level decrease the deflection is reduced to $h = 10\mu m$.

The fourth graph is showing the efficiencies during the selected test section part. The efficiencies, and namely the volumetric efficiency, is closely related to the structural deflections and the gap height between housing and the end faces of the rotor. The volumetric efficiency is increased from $\eta_v = 0.5$ to $\eta_v = 0.85$ with the decrease in the gap heights. The hydromechanical efficiency η_{hm} is increased only a little. This increase is due to the decrease in the pressure level of the chambers, which is lowering the internal friction forces. The total efficiency η_{tot} is linearly related to the volumetric- and the hydromechanical efficiency and is therefore correspondingly increased.

Deflection Comparison

The input data to the FSI simulation are measured data from the selected test section. The calculated deflections where the MCA is located on the prototype motor and the measured deflections are shown in table 2. The calculated and the measured deflections are compared for two different motor conditions. It is for the first (before $t = 595s$) and the third (after $t = 613s$) period of the selected test section that is shown in figure 11.

	Condition 1	Condition 2
p_1	$12.5bar$	$6.5bar$
p_2	$55bar$	$39bar$
p_{Comp}	$35bar$	$35bar$
h_{Theo}	$57\mu m$	$31\mu m$
h_{Meas}	$50\mu m$	$10\mu m$

Table 2. Simulated and measured deflections for two motor conditions.

It is considered inexact to validate the FSI simulation by comparing absolute dimensions in the μm range. Instead the deflection difference is used. The theoretical deflection difference from motor condition 1 to condition 2 is $26\mu m$ and the equivalent measured difference is $40\mu m$. Qualitatively, the results are useful, however, the percentage deviation is somewhat a concern.

The main reason for the deviation between the theoretical and the measured deflections is considered to be the boundary conditions in the FEM model. This should be calibrated by examining a wider range of tests.

6. Discussion

The theoretical and experimental test results shows that the volumetric efficiency can be kept at an acceptable level by the use of compensation pressure volumes to counteract the performance critical deflections. The hydromechanical efficiency can be maximized by securing that the rotor is always fully balanced and the friction forces are minimized. In the prototype motor the rotor is not axially balanced. The source to the axial imbalance is the radial vane actuation system which must be redesigned.

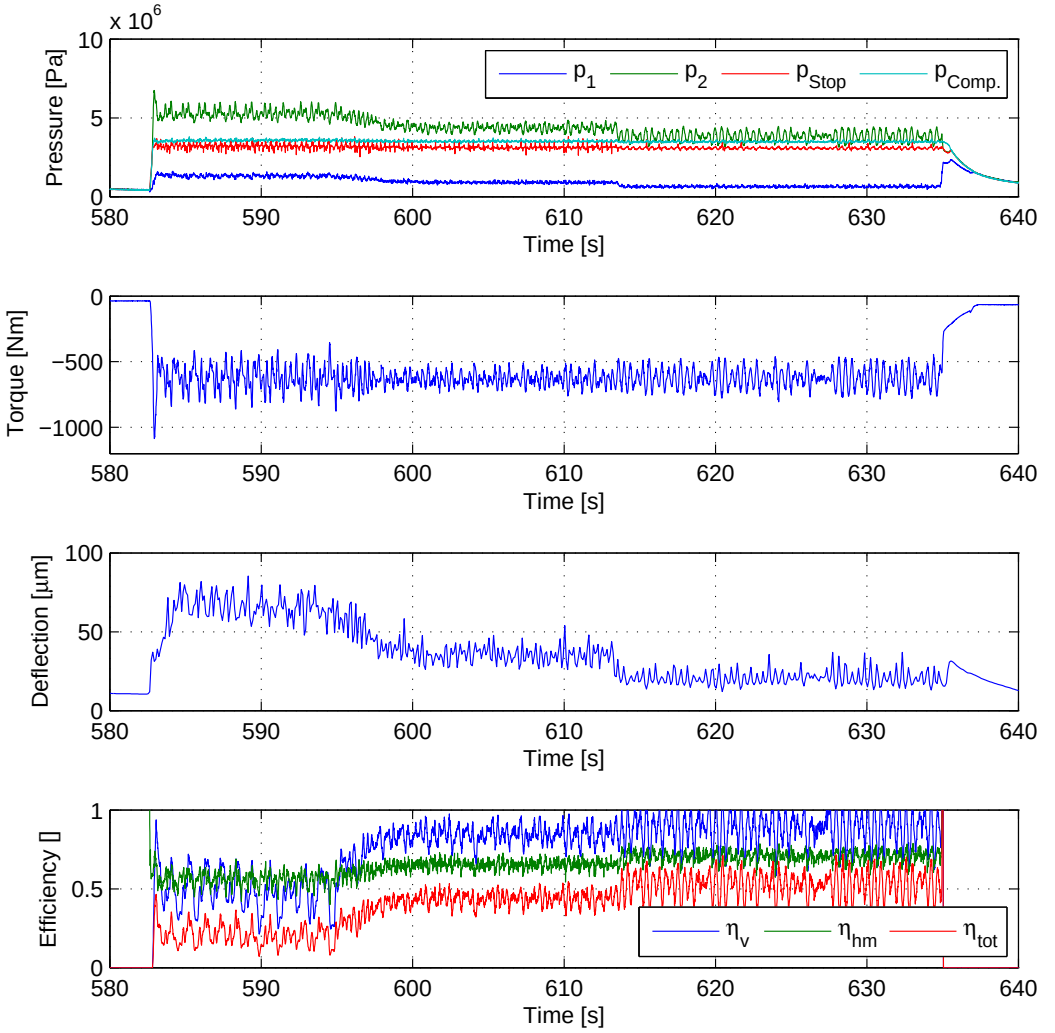

Fig. 11. Experimental test data. The input flow is decreased in two steps. The load is constant.

The aim of the FSI simulation model was to investigate the structural deflections of the prototype motor. The differences between the calculated and the measured deflection difference for the two motor conditions are $26\mu m$ and $40\mu m$ respectively. The deviation in percent is high, but the FSI simulation is reflecting the behaviour and the volumetric efficiency trends of the prototype motor. Therefore the FSI simulation is useful as a design tool. Next step in the research is to extend the FSI simulation model. Building larger prototypes is expensive, whereas the simulation model is to be used to predict the motor performance and dimensions when upscaling the motor.

The hydraulic yaw system has the potential to overcome the fundamental disadvantages associated with the pinion-gear rim connections used today. Furthermore the most extreme load cases for the yaw system can be fulfilled by designing the motor to withstand a maximum working pressure far beyond the nominal working pressure. By increasing the maximum pressure in the motor, the motor can deliver the necessary extreme torques. These extreme torques are rarely necessary, which also means that the efficiency is of less importance as compared to continuously operated motors.

Another advantage of the hydraulic yaw system is the inherited controllability of the fluid system. E.g. the stops can serve as brakes on the rotor by using the stop pres-

sure. Furthermore the stop pressures, and therefore the friction forces between stops and rotor, can serve as active damping in the yaw system.

References

[1] P. J. Tavner and J. Xiang and F. Spinato. *Reliability Analysis for Wind turbines*. wind Energy, (2007).

[2] Erich Hau. *Wind Turbines - Fundamentals, Technologies, Application, Economics*. Springer, 2nd edition, (2006).

[3] *www.energy.siemens.com/hq/en/power-generation /renewables/wind-power/wind-turbines/* Siemens Energy, Web page (11.01.2011).

[4] *www.vestas.com/en/wind-power-plants/procure ment/turbine-overview//v112-3.0-mw.aspx#/vestas-univers* Vestas, Web page (11.01.2011).

[5] *www.repower.de/index.php?id=532&L=1* REpower Systems, Web page (11.01.2011).

[6] *www.gepower.com/prod_serv/products/wind_ turbines/en/15mw/index.htm* GE Energy, Web page (11.01.2011).

[7] WO2010097086 (A1). *Hydraulic Motor or Pump*. Per Fenger , (2010).

[8] Rasmus Mørk Sørensen and Michael Rygaard Hansen and Ole Ø. Mouritsen and Per Fenger. *Investigation of Hydraulic Motor Principle for Low Speed High Torque Applications*. 22. Nordic Seminar on Computational Mechanics, (2009).

[9] *www.boschrexroth.com/RDSearch/rd/r_15228/re 15228_2008-08.pdf* Bosch Rexroth, Web page (11.01.2011).

[10] *www.hagglunds.com/Upload/20101207101946A_ En386-17H.pdf* Hagglunds, Web page (11.01.2011).

[11] Bernard J. Hamrock and Steven R. Schmid and Bo O. Jacobsen *Fundamentals of Fluid Film Lubrication*. Marcel Dekker Inc, Second Edition, (2004).